The Investigation of Crack Propagation in Cortical Bone using a Phase Field Fracture Approach

Olivia Karlsson

2022

LUND
UNIVERSITY

Master's Thesis

Faculty of Engineering, LTH
Department of Biomedical Engineering

Supervisors:
Anna Gustafsson and Hanna Isaksson

1 Abstract

Human cortical bone tissue is a complex and strong composite material, with the ability to resist damage via slowing, stopping or redirecting propagating cracks. However, the ability is impaired with age. At the microscale, changes are seen both in terms of increased porosity and as changes in local material parameters. The microstructure is based on circular concentric layers of bone tissue, called osteons, which surround the Haversian canals. The osteons are embedded in an interstitial matrix, and are separated by weak interfaces called cement lines. Both local material parameters and the effect of local toughening mechanisms are difficult to evaluate experimentally. Thus, computational models can be used as a complement.

The aim of this thesis was to investigate crack propagation in the microstructure in cortical bone using a phase field fracture approach. The phase field method is a continuous damage model in which the crack is allowed to advance if the energy release rate exceeds a critical limit. The crack is described by a crack density function which is dependent on a diffuse damage field. In this thesis, a phase field framework based on open source codes was implemented as a user-defined element subroutine in *Abaqus*. The framework was evaluated using typical benchmarks tests commonly used in the literature.

Realistic cortical bone models in 2D were created from microscopy images. The crack propagation was investigated for different material parameters, geometries and levels of porosity. The critical energy release rate of the cement lines and the osteons affected the crack propagation. With a lower value for the cement lines and a higher value for the osteons compared to the interstitial matrix protected the osteons from damage and redirected the crack into the cement lines. The ability to deflect advancing cracks decreased with increasing porosity, which is in line with both numerical and experimental studies in literature.

The phase field framework implemented in this work is a great tool for studying crack propagation in cortical bone. It could be used to further analyze the local mechanical properties and give additional insights in how the bone tissue is designed to resist fracture.

2 Acknowledgements

I want to start by thanking my main supervisor Anna Gustafsson for her constant support, patience and encouragement. Anna, even though this thesis has been done remotely, you have never felt far away. You were always just a call away. You have supported me all the way and I have learnt so much from you.

I would also like to thank my co-supervisor Hanna Isaksson, not only for your valuable feedback and input, but also for introducing me to Biomechanics at the beginning of my specialization. I would also like to acknowledge the Biomechanics Group for introducing me to the team during my introductory weeks on site in Lund. Lorenzo Grassi, thank you for helping me getting started with the remote access to my computer. I had a lot of fun during this project, and I want to thank you all for that.

Finally, my family and friends, thank you. All the long phone calls with my parents and online-AWs with my friends gave me so much during this time of home-office. A special thanks to Joakim, you are my rock! Without all of you, this would not have been possible.

Olivia Karlsson
Stockholm, January 2022

Contents

3 Introduction

Bone is a very complex and strong structure. Together with the soft tissues muscles, tendons and ligaments, they make up the musculoskeletal system of the human body. Within the field of Biomedical Engineering and specifically biomechanics, this system is studied. Among other things, we want to know how and why our bones break, and also why they fracture more easily with age and certain degenerative diseases. As our population lives longer and longer, the human body cannot keep up. With a better understanding of crack development in bone tissue, both the suffering of individuals and the high costs for the healthcare system could be reduced.

Bone tissue can be divided into two groups on the mesoscale: cortical and trabecular bone. The cortical bone, which is the focus of this thesis, is harder and makes up the outer layers in for example the shaft of the long bones [8]. The trabecular bone can be found in the vertebrae and in the ends of the long bones. The microstructure of the cortical bone is based on the structural unit, osteons, which are circular concentric layers of bone tissue and can be seen in Fig. 1. The layers surround the Haversian canals which contain blood vessels and nerves. The osteons are embedded in an interstitial matrix, and are separated by the cement lines, which are the outer shells of the osteons [13, 8].

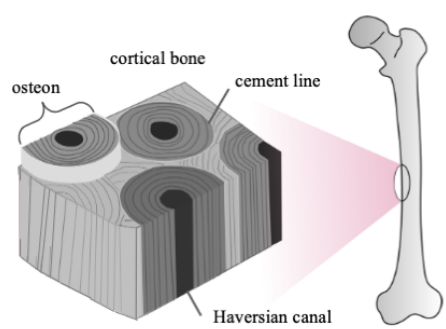

Figure 1: Structure of cortical bone with the structural unit, the osteons, with the surrounding cement lines. The osteons surrounds the Haversian canals. Figure from [13].

To study damage mechanisms in cortical bone experimentally is very challenging. The mechanical properties and the effect of the microstructure are also difficult to determine when using experimental methods. Thus, nu-

merical models are being developed as a compliment. Previously, crack propagation in cortical bone have been numerically modelled using cohesive elements and the extended finite element method (XFEM). The Phase Field (PF) method, used in this thesis, is the most recent fracture mechanics approach, and until today it has only been applied in few studies in computational biomechanics. The advantage of the phase field method is the ability to model crack propagation without a predefined crack path, and it has also shown the ability to model behaviours like crack initiation, branching, deflection and crack coalescence [2, 28]. This kind of complex behaviours have previously been difficult to model using other numerical methods [2].

The PF method have not yet been implemented in any commercial computational software. However, in the work by for example Molnár and Gravouil [28], Martínez-Pañeda et al. [25] and Kristensen and Martínez-Pañeda [20], the software *Abaqus* is used together with a user-defined element (UEL) subroutine. The codes for the UEL subroutine have been published as open source codes [20, 25, 28].

3.1 Objectives

The main objective of this thesis is to investigate the feasibility of using a phase field model for simulating crack propagation in the microstructure of cortical bone, for the purpose of a better understanding of crack development and propagation in cortical bone and the effect of ageing.

To achieve the objective, a PF framework is implemented using the open source codes provided by Martínez-Pañeda et al. [25] and Kristensen and Martínez-Pañeda [20]. The framework contains different alternatives for the PF model, for example different solution schemes and functions which describes the diffuse crack. To test and evaluate the implemented PF framework, three benchmark tests are performed. Then, PF models of microscopy images of cortical bone are created and the results are compared and validated to numerical (e.g. Gustafsson et al. [15]) and experimental results (e.g Chan et al. [7]) from the literature.

In this project, the hypothesis is that the phase field fracture approach can model crack behaviors such as deflection and initiation. Furthermore, the cement lines are crucial for the ability to resist damage at the microscale and

material parameters can influence crack behaviour. It is also hypothesized that age-related factors, such as increased porosity, weaken the structure of cortical bone, increasing the risk of damage.

4 Biomechanics and Cortical Bone

Within the field of Biomedical Engineering, the human body can be studied as a mechanical system. The human body consists of different parts contributing to its capability to move as a system, some examples are bones, muscles, ligaments and tendons. It is the application of classical mechanics to these biological systems, like the muscoskeletal system, that is the foundation of biomechanics [33]. Biomechanics is a field which combines the engineering theories and concepts with biology, physiology and anatomy. When focusing on bone tissue, the study is often referred to as bone mechanics.

4.1 Structure of Cortical Bone

Bone tissue is a heterogeneous complex composite material, which is designed to carry load. Bone is a mineralized tissue, which means that the structure is made up of minerals integrated into a softer collagen matrix [8]. Bone can be divided into two types, cortical bone and trabecular bone. We can find both types in the skeletal bones of the human body. The hard outer layer of all bones consists of cortical bone, while the trabecular bone is found in the internal porous structure [13]. In long bones, in for example the thigh bone (called femur in latin), the cortical bone makes up the shaft and the trabecular bone is mainly present at the ends. Cortical bone is more compact and dense than trabecular bone, that is why cortical bone also is referred to as compact bone [8].

The structure of cortical bone is well-defined with a unique hierarchy. The structure can be divided into different levels, see Fig. 2, where the mineralized collagen fibres can be found at the nanoscale. At microlevel, the fibres are packed together to form lamellae, which can be described as layered sheets [33]. These sheets forms the so called osteons, which are the main functional unit in this type of bone. The osteons are cylindrical bone pillars that runs parallel to each other along the shaft of the long bone [13]. The osteons are integrated in an interstitial matrix. They are approximately 0.2-0.3 mm in diameter and a few millimeters long [1]. At the centre of each osteon is the Haversian canal. The Haversian canal is a hollow cavity and the channel for the blood vessels through the compact bone tissue [8].

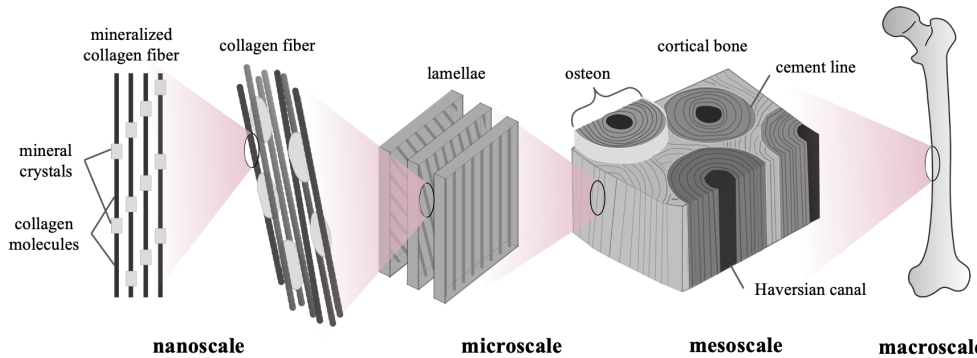

Figure 2: Structure of cortical bone displaying the hierarchy of the structure at length scales ranging from macroscale to the nanoscale. Figure from [13].

The osteons are separated from the matrix by a thin layer called the cement line. The cement lines are highly mineralized, which make them more brittle [13, 35]. The formation of osteons and cement lines are a result of the fact that the bone tissue consistently renew itself. Approximately 10-15% of the human skeleton is renewed every year [8]. The capability to replace old with new bone tissue comes from the different specialized bone cells. They are called osteocytes, osteoclasts and osteoblasts. The osteoblasts are responsible for creating new bone tissue, and osteoclasts are responsible for dissolving old bone tissue. The osteocytes are the mature bone cells that remains in the bone tissue [8]. When the osteoclasts are dissolving old bone tissue, a resorption cavity is created [13]. The outer line of this cavity is the hyper-mineralized cement lines. From this outer layer, the osteoblasts start to form new bone tissue, lamellae. Bone remodelling is a constant process [8]. With age, the interstitial matrix will contain more remains of old osteons, and therefore become more mineralized [13, 34].

4.2 Mechanical Properties of Cortical Bone

The mechanical properties of cortical bone are related to the composition and structure at the different length scales, as seen in Fig. 2. Due to the combination of the mineral phase integrated into a soft collagen matrix, the bone tissue is both strong and stiff, while also being light [33, 36]. One way to study the mechanical properties of bone (experimentally) is through

loading the bone tissue, and studying a stress-strain curve, or similarly a force-displacement curve [33].

Due to the longitudinal structure of the osteons, cortical bone has anisotropic properties [33]. It means that the cortical bone has different mechanical properties when loaded in different directions (Fig. 3). The stiffness in the longitudinal direction is greater than in the transverse. The area under curve, which is the amount of energy stored in the material before fracture, is also greater when loaded in the longitudinal direction. The plastic region of transverse load is smaller, and shows more brittle behaviour than the longitudinal. This means that the tissue can deform less before failure when loaded in the transverse direction. The maximum force, also called ultimate strength, is also less for the transversal load. Note that the curves in Fig. 3 are tensile loads. Cortical bone is more resistant in compression than tension, which is not that surprising since we load our legs with our body weight in that direction everyday. The bone tissue is always adapting to the load applied [33].

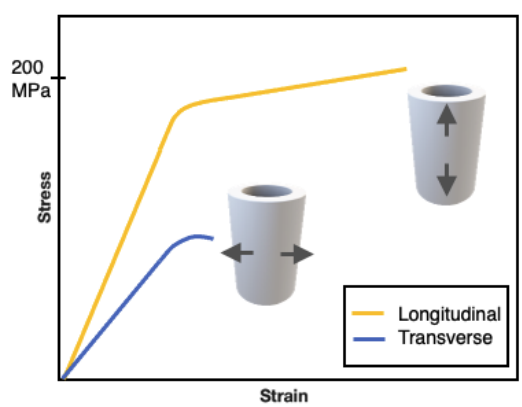

Figure 3: Stress-strain curve for cortical bone under tensile load in two different directions: Longitudinal in yellow and Transverse in blue. The directions are illustrated with a hollow cylinder representing the shaft of a long bone. Drawn based on figure in [33].

The structure of cortical bone includes several mechanisms that enable the tissue to resist damage. One could say that the bone protects itself from failure and fracture. It can resist fracture at multiple length scales. At the microscale, it resists fracture by redirecting, decelerating and also stopping

cracks from advancing in the tissue [22, 33]. At smaller length scales, the bone structure instead prevents crack initiation. The process of bone remodelling also contributes to the fracture resistance, by replacing broken bone tissue with new in regions of damage and microcracks.

Cortical bone has a high fracture toughness, and this is due to the composition and structure of the bone tissue together with its ability to heal itself. When comparing the collagen and minerals separately, the fracture toughness of the bone tissue exceeds the other two [13, 36]. It is also clear that the cement lines of the osteons play a role in the ability to resist fracture [8]. The cement lines protect the osteons by providing another weaker path and thereby directing the cracks to advance along the line or within the more mineralized interstitial matrix [13]. However, it is difficult to determine the mechanical properties for the matrix, osteons and cement lines individually. The conventional methods used to determine fracture toughness is done at a tissue level, and therefore it is difficult to distinguish between matrix, osteons and cement lines [13].

4.3 The Effect of Ageing

As we age, so do our bones. The effect of ageing on cortical bone is firstly observed as the loss of bone mass, i.e. lower bone density. The quantity of bone tissue decreases, but so does the quality. The microdamage and microcracks accumulate when the osteoblasts cannot keep up, as their ability to form new bone tissue is impaired with age [33]. The cement lines also become less effective in deflecting and redirecting cracks [8]. The reason is unknown, but when comparing crack paths in young and old bone tissue, cracks that have penetrated the osteons are observed more often in the older bone tissue [7] as can be seen in Fig. 4.

The decrease of bone mass, as an effect of ageing of the cortical bone tissue, is due to increased porosity. This can be in the form of increased number of pores as well as increased size of the pores [32]. This leads to decreased fracture toughness of the tissue.

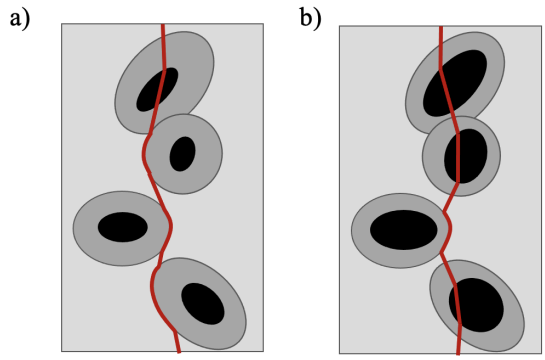

Figure 4: Sketch of crack path (in red) in young bone tissue in a) and old bone tissue in b). The crack is deflected and follow the cement lines to a greater extent in the young bone tissue in a) compared to the old bone tissue in b). The crack path is more straight and penetrates the osteons for the old bone tissue. Drawn based on figure in Chan et al. [7].

4.4 Computational Models of Cortical Bone

To gain further knowledge about the properties and behaviour of cortical bone, numerical methods can be used to complement the experiments. Several studies using numerical methods based on the finite element method have been used to model bone mechanics.

The study by Mischinski and Ural [27] investigated crack propagation in cortical bone at a microscale, and the effect of the cement lines. They used a method called cohesive elements, which models the crack as discontinuity. The cohesive elements are interface elements that are placed in between solid elements, and are therefore based on a predefined crack path. The study introduced two predefined cracks, one penetrating the osteon and one deflected into the cement line, see Fig. 5. The study gave an insight in how crack paths in cortical bone are affected by changes in the microstructure. For example, the crack trajectory was affected when altering the fracture properties of the osteons and also when altering the properties of the cement lines [27].

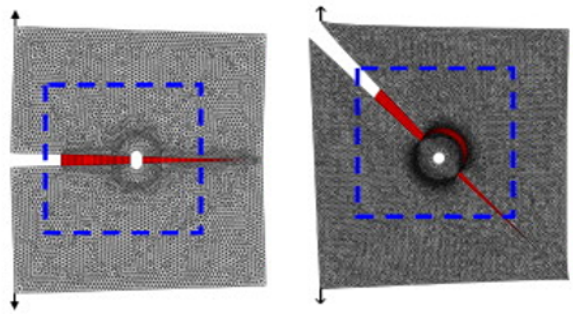

Figure 5: The predefined cracks introduced in the study by Mischinski and Ural [27] which used the cohesive elements method. The predefined cracks are one penetrating the osteon and one deflected into the cement line. The figure is from [27] and reprinted with permission from Elsevier.

As mentioned earlier, the mechanical properties of the cement line are not easily determined experimentally. One of these properties is the critical energy release rate $\mathcal{G}_c$, which is the limit of the energy required for a crack to advance in the material [12]. In the study by Giner et al. [10], the critical energy release rate $\mathcal{G}_c$ is estimated using both experimental and numerical methods. Giner et al. [10] calibrated the numerical FE model to the experimental results found in the study. The calibrated FE model was then used to estimate $\mathcal{G}_c$, by approximating the variation of the strain energy of the system when the crack propagated though the cement line together with the definition of the energy release rate (Eq. 2 in Section 5.1.1). The numerical FE method used is called element deletion method, as seen in Fig. 6, which is based on that elements are considered failed or "killed" once the failure strain is reached. The results of the study showed that the crack advanced mostly in the cement lines or the interstitial matrix, rather in the osteonal tissue.

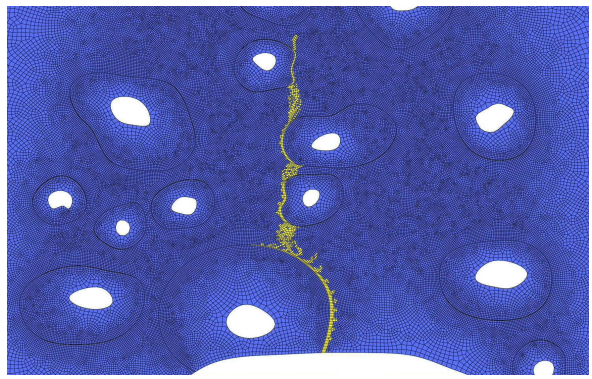

Figure 6: The element deletion method used in the study by Giner et al. [10]. The blue elements are intact and the yellow elements are the "killed" elements for which the failure strain has been reached. The crack is therefore represented by the yellow elements. The figure is reprinted with permission from Elsevier.

Another commonly used method is the extended finite element method (XFEM) which is also a method based on a discrete crack. It is also a cohesive fracture model, as the method of cohesive elements, however it does not require a predefined crack. It allows the crack to advance by replacing one element with two when the material fractures. By using additional degrees of freedom, the new elements are created using original nodes and the additional so called phantom nodes. This method is implemented in *Abaqus*. In the study by Gustafsson et al. [15], XFEM was used to model crack propagation in cortical bone at the microscale. Realistic geometries of the microstructure were used in the study, and they were based on microscopy images [15]. The procedure for creating the models is captured in Fig. 7.

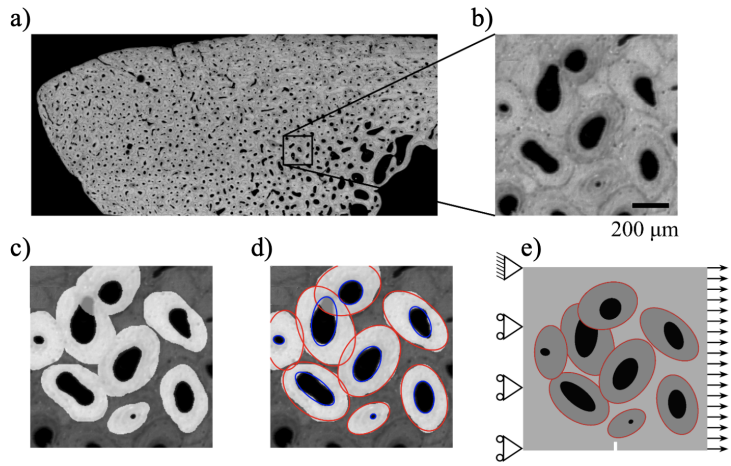

Figure 7: Pipeline of the development of the cortical bone model in the study by Gustafsson et al. [15]. a) A scanning acoustic microscopy (SAM) image of a tibial shaft (the shinbone). b) Sub-region of the size 1x1 mm^2. c) Osteons and Haversian canals manually segmented. d) Ellipses fitted to the manually segmented osteons and Haversian canals. e) Resulting model with boundary conditions for a tensile test. A frame around the image was added and extended the model to the size 1.2x1.2 mm^2, so that the osteons were not cut by the boundaries. The figure is from [15] and is reprinted with permission from Elsevier.

In the study by Gustafsson et al. [15], the crack propagation was investigated, and the effect of age in terms of porosity and fracture energy was analyzed. The results showed that the cement lines effectively deflected the propagating crack. With increasing porosity the crack path advanced and penetrated the osteons [15], which is captured in Fig. 8. The same results were found for a lower fracture energy. The crack path in different geometries were also analyzed, where the the number of osteons in the model varied, and the results can be seen in Fig. 9. One disadvantage of the XFEM implemented in *Abaqus* is that there can only be one active crack, and an element can only be split into two once. This means that new cracks cannot form. This is the reason Gustafsson et al. [15] models the Haversian canals with XFEM elements with a very small stiffness and critical energy release rate. If they were instead modelled as holes in the geometry, a new crack could not be initiated if the crack advanced to penetrate the osteon and reaching the canal.

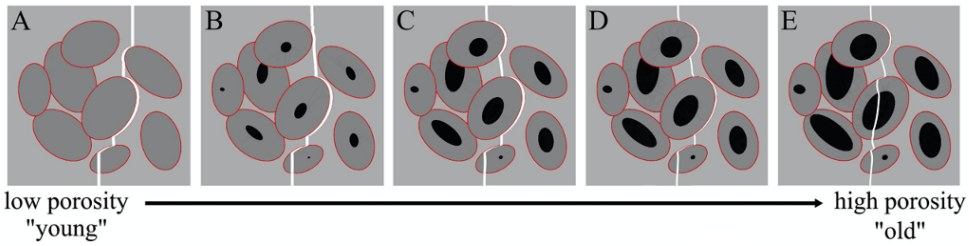

Figure 8: The resulting crack paths from using XFEM in the study by Gustafsson et al. [15]. XFEM-models with (A) 0 %, (B) 2 % (C) 7 %, (D) 9 % and (E) 15 % porosity were evaluated.The figure is reprinted with permission from Elsevier.

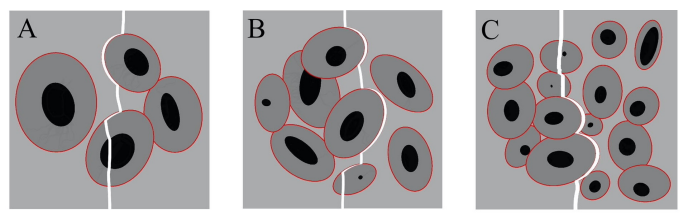

Figure 9: The resulting crack paths from using XFEM in the study by Gustafsson et al. [15]. XFEM-models with different geometry which included (A) 4 osteons (B) 8 osteons and (C) 15 osteons were evaluated. The porosity of the models was 7%. The figure is reprinted with permission from Elsevier.

The phase field (PF) method is actively used within the field of fracture mechanics, but is however new in the area of biomechanics. During the last year, Maghami et al. [23] published an article using the PF method to evaluate fracture behaviour in cortical bone. Similarly to the study by Gustafsson et al. [15], they used realistic geometries based on microscopy images, as can be seen in Fig. 10 [23]. They formulated the PF method using the UEL subroutine in *Abaqus* based on open source code from the study by Molnár and Gravouil [28] which used the work by Miehe et al. [26] as a base. The results presented by Maghami et al. [23] showed that the cement lines do affect the crack trajectory, and that the extent in which the propagating cracks are deflected decreases with age.

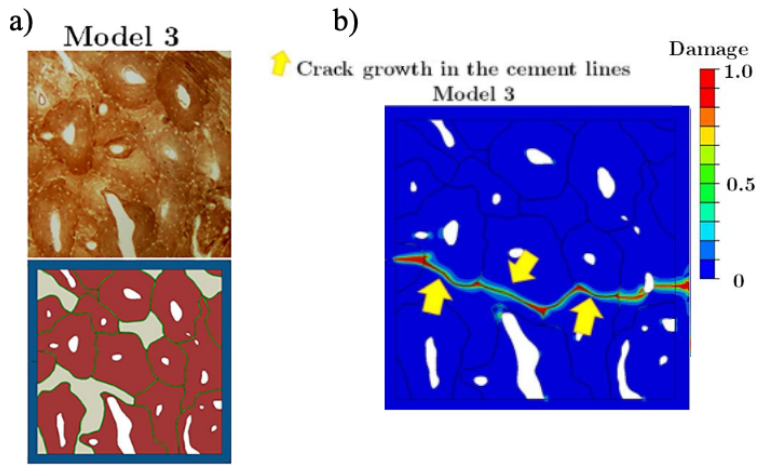

Figure 10: a) The human cortical bone models used in the study by Maghami et al. [23], which are based on microscopy images. b) The resulting phase field of the cortical bone model where the crack have deflected into the cement lines marked with yellow arrows. The figures a) and b) are from [23] and are reprinted with permission from Elsevier.

5 Fracture Mechanics and The Phase Field Method

5.1 Fracture Mechanics

Fracture is the phenomenon where an intact body is split or partially split into parts. The study and characterization of this phenomenon is the foundation of the field fracture mechanics [12]. Fracture can occur by one or more cracks propagating through a body, and can take place at all length scales [13]. It is of great importance to be able to study the evolution and behaviour of cracks from an engineering point of view. When relying on continuum mechanics, material behaviours are often quantified by stresses and strains [12]. These quantities cannot be directly used to predict fracture behaviour, and there are two reasons for that. The first reason is that these quantities becomes infinite close to the crack tip. Dependent on the size of the inelastic region around the crack tip, referred to as the plastic zone, fracture mechanics can be divided into two branches; linear-elastic fracture mechanics (LEFM) and nonlinear fracture mechanics [12, 13]. LEFM can be applied to materials where the plastic zone is very small or non-existent. This can be seen in brittle fractures, and therefore LEFM can also be referred to as brittle fracture mechanics [12]. The other reason is that cracks of different lengths behave differently when the same stress is applied. To quantify this, fracture criterions were introduced within the field of fracture mechanics. Two examples are the critical energy release rate presented by Griffith [11] and the stress intensity factor presented by Irwin [18].

5.1.1 Griffith's Theory

In 1921, Griffith [11] published the concept that became a milestone within fracture mechanics. The concept is called *Griffith's fracture criterion*, which is an energy criterion. Griffith's theory is based on that during stable crack propagation, there is no change in the total energy of the system [5]. Therefore energy is dissipating while new surfaces are created when the crack progresses. This can be expressed by

$$\frac{d(\Pi^{int} + \Pi^{sur} + \Pi^{ext})}{da} = 0, \tag{1}$$

where Π^{int} is the potential energy of the material, Π^{sur} is the surface energy of the crack faces and Π^{ext} is the potential energy of the external forces [12]. For an infinitesimal crack length da, the change in the total energy is equal to zero. This is applied for plane problems. The expression can be used to define the energy release rate, which is the energy released when the crack has advanced with the infinite small crack length da. The energy release rate $\mathcal{G}$ is expressed in Eq. 2.

$$\mathcal{G} = \frac{d\Pi^{sur}}{da} = -\frac{d(\Pi^{int} + \Pi^{ext})}{da} \tag{2}$$

The criterion for fracture is based on the critical energy release rate $\mathcal{G}_c$, which is a material parameter. This means that for a crack to advance, the energy released must be equal to or greater than the energy needed for fracture, i.e. $\mathcal{G} = \mathcal{G}_c$. The critical energy release rate is also known as the crack resistance [12].

5.1.2 Stress Intensity Factor

Following the work by Griffith [11], Irwin [18] presented the concept of linear-elastic fracture mechanics (LFEM) in 1957. The stresses around the crack tip could now be characterized using stress intensity factors (SIF) [5]. It is also referred to as the K-concept, and it divides the crack into three different cracking modes, see Fig. 11 [5, 12]. For Mode I, the crack opens under tensile load. In Mode II, the crack faces are sliding against each other due to in-plane shear load. The out-plane shear load makes the crack faces tear against each other in Mode III [5, 12, 13].

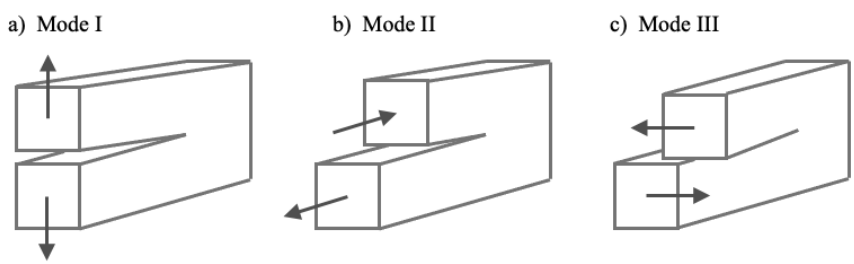

Figure 11: The three crack modes with Mode I in a), Mode II in b), and Mode III in c). Drawn from figure in Carlsson [5].

The SIF for each mode, K_I, K_{II} and K_{III}, can be used as a fracture criterion and are then referred to as the fracture toughness K_c [12]. The SIF for the three different crack modes are defined by

$$K_{I,II,III} = Q\sigma_f\sqrt{\pi a} \tag{3}$$

where Q is a dimensionless constant which depends on geometry and type of loading, σ_f is the critical stress, and a is the crack length. The fracture criterion using the fracture toughness is expressed as $K_{Ic} = K_I$, using Mode I as an example. K_c is a material parameter, similarly to the critical energy release rate $\mathcal{G}_c$ [12]. K_c is connected to $\mathcal{G}_c$ as described in Eq. 4, where E is the Young's modulus and ν is Poisson's ratio [12, 13].

$$\mathcal{G}_c = \frac{K_c^2}{E'}, \qquad \text{with } E' = \begin{cases} E & \text{for plane stress} \\ \frac{E}{1-\nu^2} & \text{for plane strain} \end{cases} \tag{4}$$

5.2 The Phase Field Method

With Griffith's theory [11] in mind, the next step towards the phase field (PF) method is the variational approach to fracture [5]. It is closely related to Griffith's theory. The approach was presented in an article by Francfort and Marigo in 1998 [9].

In the variational approach to fracture [9], a set of possible crack paths is considered [5]. The approach includes a condition which states that the crack path in the set which gives the minimum or a stationary point of the total energy of the body must be the real one [5, 9]. Basing the PF models on this approach, contributes to the ability of the PF method to model crack initiation and find the direction of the propagation of the crack. Another condition that must be fulfilled is regarding the area of the crack faces. It can only increase or stay constant, never decrease [5]. This is the same as saying that the crack cannot heal. On the basis of the variational approach, the PF method can be further described, starting with the total energy of a body.

5.2.1 Total Energy of a Body

Consider a body with a discrete crack Γ, as seen in Fig. 12a. The total energy of this body can be described by Eq. 5 [5]. The potential energy in

the body Π^{int}, in terms of strain energy, is dependent of the displacement field $\mathbf{u}$ and the crack Γ. The strain energy density is denoted as $\hat{\psi}_0$. The surface energy of the crack faces Π^{sur} is dependent on the crack Γ and the critical energy release rate $\mathcal{G}_c$ of the material of the body. The potential energy of the external forces Π^{ext} is dependent on $\mathbf{u}$ as well as the body forces $\hat{\boldsymbol{b}}$ and the applied traction $\boldsymbol{t}$, as seen in Fig. 12a. According to Francfort and Marigo [9], the minimization of Eq. 5 is governing the process of crack growth [2, 5].

$$
\begin{aligned}
\Pi(\Gamma, \boldsymbol{u}) &= \Pi^{int}(\Gamma, \boldsymbol{u}) + \Pi^{sur}(\Gamma) + \Pi^{ext} \\
\Pi^{int}(\Gamma, \boldsymbol{u}) &= \int_{\mathcal{B}} \hat{\psi}_0(\Gamma, \varepsilon(\boldsymbol{u}))\mathrm{d}V \\
\Pi^{sur}(\Gamma) &= \int_{\Gamma} \mathcal{G}_c \mathrm{d}A = \mathcal{G}_c \int_{\Gamma} \mathrm{d}A \\
\Pi^{ext} &= \int_{\partial\mathcal{B}} -\boldsymbol{t} \cdot \boldsymbol{u}\mathrm{d}A + \int_{\mathcal{B}} -\boldsymbol{u} \cdot \hat{\boldsymbol{b}}\mathrm{d}V
\end{aligned}
\tag{5}
$$

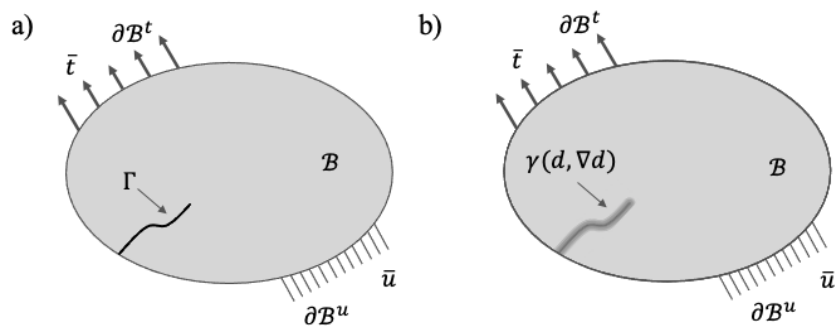

Figure 12: A body $\mathcal{B}$ with the boundary conditions $\boldsymbol{u} = \overline{\boldsymbol{u}}$ and $\delta\boldsymbol{u} = 0$ on $\partial\mathcal{B}^u$ and $\boldsymbol{t} = \bar{\boldsymbol{t}}$ on $\partial\mathcal{B}^t$. The body in a) has a sharp discrete crack Γ and the body in b) has a diffuse crack expressed by the crack density function $\gamma(d, \nabla d)$ which is dependent on the diffuse damage field d. Drawn based on figure in Carlsson [5].

5.2.2 Crack Density Function

It is almost impossible to find analytical solutions to the variational approach, and it must therefore be solved numerically. To make that possible, the discrete crack Γ, as seen in Fig. 12a, will be modelled with a crack density

function which is dependent on a diffuse damage field (Fig. 12b), which was presented by Bourdin et al. in 2000 [4]. The damage field, also called the phase field d, is a scalar-valued regularized field. The phase field variable is therefore defined as a smooth transition between $0 \leq d \leq 1$, and $d = 0$ represents material that is intact and $d = 1$ represents fully broken material [2, 4, 5, 28].

The crack density function, also called crack functional $\gamma(d, \nabla d)$, which models the sharp crack Γ, can be expressed in many ways. It is dependent on the phase field variable and its gradient. In this thesis, two crack functionals are used. The crack functionals are referred to as AT1 (Ambrosio-Tortorelli 1) and AT2 (Ambrosio-Tortorelli 2) and are defined in Eq. 6 [5]. AT1 has an elastic region before the crack is initiated. AT2 does not have a linear region, and the damage is initiated directly [5, 24].

$$\begin{aligned} \gamma_{AT2}(d, \nabla d) &= \frac{1}{2\ell_c}\left[d^2 + \ell_c^2 \nabla d \cdot \nabla d\right] \\ \gamma_{AT1}(d, \nabla d) &= \frac{3}{8\ell_c}\left[d + \ell_c^2 \nabla d \cdot \nabla d\right] \end{aligned} \tag{6}$$

The parameter ℓ_c is the length scale parameter or the characteristic length of the crack which determines the width of the diffuse crack. When $\ell_c \to 0$, the sharp crack Γ will be retrieved. The choice of the length scale parameter comes with a condition regarding the mesh size h. The mesh size h must be small enough in order to capture and resolve a diffuse PF crack. The conditon according to Miehe et al. [26] is defined as: $h < \ell_c/2$.

Using the crack density function, the surface energy of the crack can be approximated by

$$\Pi^{sur}(\Gamma) = \mathcal{G}_c \int_\Gamma \mathrm{d}A \approx \mathcal{G}_c \int_\mathcal{B} \gamma(d, \nabla d)\mathrm{d}V = \Pi^{crack}(d, \nabla d). \tag{7}$$

The advantage of modelling the discrete crack as diffuse crack is that the surface energy, previously expressed as a surface integral, can be approximated with a volume integral over the whole body. By using this approximation, the definition of the total energy of the body expressed in Eq. 5 can be rewritten as

$$\Pi(\boldsymbol{u}, d) = \Pi^{int}(\boldsymbol{u}, d) + \Pi^{crack}(d, \nabla d) + \Pi^{ext}. \tag{8}$$

5.2.3 Isotropic Model

For an isotropic linear elastic body, the strain energy density is defined as

$$\hat{\psi}_0(\boldsymbol{\varepsilon}) := \frac{1}{2}\boldsymbol{\varepsilon} : \mathbb{C} : \boldsymbol{\varepsilon} \tag{9}$$

where $\boldsymbol{\varepsilon}$ is the small strains defined as $\boldsymbol{\varepsilon} = \frac{1}{2}\left(\nabla \boldsymbol{u} + \nabla \boldsymbol{u}^T\right)$ and $\mathbb{C}$ is the linear elastic stiffness tensor. $\mathbb{C}$ in Voight notation, and for plane strain conditions, can be defined as

$$\mathbb{C} = \frac{E}{(1+\nu)(1-2\nu)} \begin{bmatrix} 1-\nu & \nu & \nu & 0 \\ \nu & 1-\nu & \nu & 0 \\ \nu & \nu & 1-\nu & 0 \\ 0 & 0 & 0 & \frac{1-2\nu}{2} \end{bmatrix} \tag{10}$$

where E is the Young's modulus and ν is the Poisson's ratio. $\mathbb{C}$ can also be used to express the Cauchy stress tensor for an (undamaged) isotropic linear elastic material, $\boldsymbol{\sigma}_0 = \mathbb{C} : \boldsymbol{\varepsilon}$ [20]. Here, $\boldsymbol{\varepsilon} = \{\varepsilon_{xx}, \varepsilon_{yy}, \varepsilon_{zz}, 2\varepsilon_{xy}\}^T$.

During the growth of a crack, the material will lose its stiffness as the damage increases. This is introduced using the PF variable d and a degradation function $g(d)$. A commonly used degradation function is

$$g(d) = [(1-d)^2 + k], \tag{11}$$

where k is a small numerical parameter added for stability reasons [25]. The Cauchy stress tensor can thereby be expressed as

$$\boldsymbol{\sigma} = \left[(1-d)^2 + k\right] \frac{\partial \hat{\psi}_0(\boldsymbol{\varepsilon})}{\partial \boldsymbol{\varepsilon}} = \left[(1-d)^2 + k\right] \boldsymbol{\sigma}_0 = \left[(1-d)^2 + k\right] \mathbb{C} : \boldsymbol{\varepsilon} \tag{12}$$

where $\boldsymbol{\sigma}_0$ is the undamaged Cauchy stress tensor for a linear elastic material.

Another condition that must be fulfilled in the PF model is the irreversibility of the crack growth [9]. The area of the crack faces can only increase or stay constant, never decrease. To ensure this condition, Miehe et al. [26] introduced the history field

$$\mathscr{H}(\boldsymbol{x}, t) = \max_{\tau \in [0,t]} \hat{\psi}_0(\boldsymbol{\varepsilon}(\boldsymbol{x}, \tau)). \tag{13}$$

By replacing $\hat{\psi}_0$ with the history field variable $\mathscr{H}$, it is ensured that the strain energy in each point $\boldsymbol{x}$ is the largest experienced strain energy in the simulation history [2, 5]. By always using the maximum strain energy experienced, the crack cannot heal.

5.2.4 Anisotropic Model with Strain Energy Split

The isotropic PF models have shown unrealistic and unphysical behaviour, like crack growth during compression [2]. Therefore a split between tension and compression can be introduced, where the crack is assumed to grow only under tensile load, and not under compressive load. Therefore the strain energy density can be split into two parts: one positive part $\hat{\psi}_0^+$ stemming from tensile strains and one negative part $\hat{\psi}_0^-$ stemming from compressive strains [5]. A model with strain energy split is called an anisotropic model [2].

The positive and the negative parts can be split in many ways. The two most common splits are the spectral split by Miehe et al. [26] and the volumetric-deviatoric split by Amor et al. [3]. This thesis is using the volumetric-deviatoric split because Carlsson and Isaksson [6] used it when modelling crack propagation in the microstructure of wood and it is easier to implement compared to the spectral split. The volumetric-deviatoric split divides the strain energy density $\hat{\psi}_0$ by the volumetric and deviatoric contributions. $\hat{\psi}_0^+$ and $\hat{\psi}_0^-$ of the split are defined in Eq. 14, where $K_n = \lambda + \frac{2\mu}{n}$ is the bulk modulus and λ and μ are the Lamé constants [3]. n is the number of dimensions of the problem, i.e. $n = 2$ for plane problems. The operators $\langle\cdot\rangle_\pm$ are defined as $\langle\cdot\rangle_\pm := \frac{1}{2}(\cdot \pm |\cdot|)$ and the deviatoric strain is $\boldsymbol{\varepsilon}^{dev} = \boldsymbol{\varepsilon} - \mathrm{tr}(\boldsymbol{\varepsilon})\boldsymbol{I}/3$.

$$\begin{aligned} \hat{\psi_0}^+(\boldsymbol{\varepsilon}) &:= \frac{1}{2}K_n\langle \mathrm{tr}(\boldsymbol{\varepsilon})\rangle_+^2 + \mu\left(\boldsymbol{\varepsilon}^{dev} : \boldsymbol{\varepsilon}^{dev}\right) \\ \hat{\psi_0}^-(\boldsymbol{\varepsilon}) &:= \frac{1}{2}K_n\langle \mathrm{tr}(\boldsymbol{\varepsilon})\rangle_-^2 \end{aligned} \tag{14}$$

For the crack to only grow during tensile load, the degradation function $g(d)$ will only be applied to the positive part $\hat{\psi}_0^+$, while the negative part $\hat{\psi}_0^-$ remains unaffected [5]. Using the degradation function (Eq. 11), the anisotropic strain energy density can be expressed as

$$\hat{\psi}_0(\boldsymbol{\varepsilon}, d) = [(1-d)^2 + k]\hat{\psi}_0^+(\boldsymbol{\varepsilon}) + \hat{\psi}_0^-(\boldsymbol{\varepsilon}) \tag{15}$$

and the Cauchy stress tensor for an anisotropic material, using the split of the strain energy and the degradation function, can be expressed as

$$\boldsymbol{\sigma}(\boldsymbol{u}, d) := \left[(1-d)^2 + k\right]\frac{\partial\hat{\psi}_0^+(\boldsymbol{\varepsilon})}{\partial\boldsymbol{\varepsilon}} + \frac{\partial\hat{\psi}_0^-(\boldsymbol{\varepsilon})}{\partial\boldsymbol{\varepsilon}} = \left[(1-d)^2 + k\right]\boldsymbol{\sigma}^+ + \boldsymbol{\sigma}^-. \tag{16}$$

Similarly to the isotropic model, the history variable $\mathscr{H}$ must also be introduced for the anisotropic model, to ensure that the crack growth is irreversible. Since the strain energy density $\hat{\psi}_0$ is split in this model, the definition for the history variable must be altered. Miehe et al. [26] therefore introduced $\mathscr{H}^+$ as

$$\mathscr{H}^+(\boldsymbol{x}, t) = \max_{\tau \in [0,t]} \hat{\psi}_0^+(\boldsymbol{\varepsilon}(\boldsymbol{x}, \tau)). \tag{17}$$

Using $\mathscr{H}^+$ ensures that the positive strain energy in each point $\boldsymbol{x}$ is the largest experienced positive strain energy in the simulation history and therefore the crack cannot heal [2, 5].

5.2.5 The Hybrid Formulation

Choosing an anisotropic model instead of an isotropic model comes with a greater computational cost due to the non-linearity of Eq. 16 when solving the problem numerically. Ambati et al. [2] suggested an alternative method, the hybrid formulation, which lowers the computational cost. The hybrid formulation is the combination of the isotropic and anisotropic model. The isotropic formulation is used to describe the displacement field and the anisotropic formulation is to describe the phase field.

The hybrid formulation retains the linearity of the linear momentum balance equation from the isotropic model, by using the undamaged Cauchy stress tensor (Eq. 12) for the displacement field. The governing equation for the phase field uses the history variable $\mathscr{H}^+$, as defined for the anisotropic model in Eq. 17. The split of the strain energy density is therefore introduced in the hybrid formulation by using $\mathscr{H}^+$. At the end of the next section 5.2.6, the difference between the isotropic, anisotropic and hybrid formulation becomes clear when expressed using the strong form.

5.2.6 The Weak and Strong Form

The Dirichlet variational principle, or the principle of least action, will be used to derive the strong form of both the displacement field $\boldsymbol{u}$ and the phase field d. This is done by calculating the first variation of the total potential energy. The total energy of the body is defined in Eq. 18, combining Eq. 7, 8 and 15. Note that through this section, the stability parameter k will be

omitted in the equations and the history field variable $\mathscr{H}^+$ will replace $\hat{\psi}_0^+$, in concordance with the hybrid formulation.

$$\begin{aligned}\Pi(\boldsymbol{u}, d) &= \Pi^{int}(\boldsymbol{u}, d) + \Pi^{crack}(d, \nabla d) + \Pi^{ext}(\boldsymbol{u}) \\ &= \int_{\mathcal{B}} \left\{ [1-d]^2 \hat{\psi}_0^+(\boldsymbol{\varepsilon}) + \hat{\psi}_0^-(\boldsymbol{\varepsilon}) \right\} \mathrm{d}V \\ &+ \mathcal{G}_c \int_{\mathcal{B}} \gamma(d, \nabla d) \mathrm{d}V + \int_{\partial\mathcal{B}} -\boldsymbol{t} \cdot \boldsymbol{u} \ \mathrm{d}A + \int_{\mathcal{B}} -\boldsymbol{u} \cdot \hat{\boldsymbol{b}} \ \mathrm{d}V\end{aligned} \tag{18}$$

The first variation of the total energy with respect to both the displacement field $\boldsymbol{u}$ and the phase field d is

$$\begin{aligned}\delta\Pi(\boldsymbol{u}, d \mid \delta\boldsymbol{u}, \delta d) = \lim_{\epsilon \to 0} \frac{\mathrm{d}}{\mathrm{d}\epsilon} \Pi\left(\boldsymbol{u}^*, d^*\right) = 0, \quad \epsilon \in \mathbb{R} \quad \text{with} \\ \boldsymbol{u}^* = \boldsymbol{u} + \epsilon\delta\boldsymbol{u} \\ d^* = d + \epsilon\delta d\end{aligned} \tag{19}$$

The corresponding boundary conditions, as seen in Fig.12, are $\boldsymbol{u} = \overline{\boldsymbol{u}}$ and $\delta\boldsymbol{u} = 0$ on $\partial\mathcal{B}^u$ and $\boldsymbol{t} = \overline{\boldsymbol{t}}$ on $\partial\mathcal{B}^t$.

If the variation in Eq. 19 is solved for the two fields separately with respect to $\delta\boldsymbol{u}$ and δd, the weak form for each field are derived. The weak form of the displacement field $\boldsymbol{u}$ is defined in Eq. 20 and the weak form of the phase field d is defined in Eq. 21 for the two crack density functions AT1 and AT2 [5, 25].

$$\delta\Pi(\boldsymbol{u}, d \mid \delta\boldsymbol{u}) = \int_{\mathcal{B}} \boldsymbol{\sigma} : \nabla\delta\boldsymbol{u} \mathrm{d}V + \int_{\partial\mathcal{B}} -\delta\boldsymbol{u} \cdot \boldsymbol{t} \mathrm{d}A + \int_{\mathcal{B}} -\delta\boldsymbol{u} \cdot \hat{\boldsymbol{b}} \mathrm{d}V = 0 \tag{20}$$

$$\begin{aligned}&\text{AT2:} \quad \delta\Pi(\boldsymbol{u}, d \mid \delta d) \\ &= \int_{\mathcal{B}} \left\{ -\delta d 2[1-d]\mathscr{H}^+ + \frac{\mathcal{G}_c}{2\ell_c} \left[\delta d 2d + \ell_c^2 2\nabla\delta d \cdot \nabla d \right] \right\} \mathrm{d}V = 0 \\ &\text{AT1:} \quad \delta\Pi(\boldsymbol{u}, d \mid \delta d) \\ &= \int_{\mathcal{B}} \left\{ -\delta d 2[1-d]\mathscr{H}^+ + \mathcal{G}_c \frac{3}{8\ell_c} \left[\delta d + \ell_c^2 2\nabla\delta d \cdot \nabla d \right] \right\} \mathrm{d}V = 0\end{aligned} \tag{21}$$

The strong form of the displacement field can be derived from the weak form in Eq. 20 by using Gauss' divergence theorem together with Cauchy's theorem [25]. It is expressed in Eq. 22. The strong form of the phase field

can also be derived using Gauss' divergence theorem, however in this case homogeneous Neumann boundary conditions must be assumed: $\mathcal{G}_c \ell_c \nabla d \cdot \boldsymbol{n} = 0$ on $\partial\mathcal{B}$. The strong form of the phase field for the two crack density functions are given in Eq. 23. For a more detailed derivation, see Appendix A.1. This set of partial differential equations, together with the boundary conditions summarized in Eq. 24, is called the Euler-Lagrange equations of the problem [5, 25].

$$\operatorname{div} \boldsymbol{\sigma} + \hat{\boldsymbol{b}} = 0 \tag{22}$$

$$\begin{aligned} \text{AT2:} \quad & 2[1-d]\mathscr{H}^+ - \frac{\mathcal{G}_c}{\ell_c}\left[d - \ell_c^2 \operatorname{div} \nabla d\right] = 0 \\ \text{AT1:} \quad & 2[1-d]\mathscr{H}^+ - \frac{3\mathcal{G}_c}{8\ell_c}\left[1 - 2\ell_c^2 \operatorname{div} \nabla d\right] = 0 \end{aligned} \tag{23}$$

$$\begin{aligned} \boldsymbol{u} &= \overline{\boldsymbol{u}} \quad \text{on} \quad \partial\mathcal{B}^u \\ \boldsymbol{t} &= \overline{\boldsymbol{t}} \quad \text{on} \quad \partial\mathcal{B}^t \\ \mathcal{G}_c \ell_c \nabla d \cdot \boldsymbol{n} &= 0 \quad \text{on} \quad \partial\mathcal{B} \end{aligned} \tag{24}$$

Using the strong forms in Eq. 22 and 23, the isotropic formulation, the anisotropic formulation and the hybrid formulation can be more easily defined. On the next page there is an equation box presented which summarizes the difference between those formulations.

Isotropic formulation

$$\operatorname{div}\boldsymbol{\sigma} + \hat{\boldsymbol{b}} = 0$$

$$\text{where } \boldsymbol{\sigma}(\boldsymbol{u}, d) = (1-d)^2 \frac{\partial \hat{\psi}_0(\boldsymbol{\varepsilon})}{\partial \boldsymbol{\varepsilon}} = (1-d)^2 \boldsymbol{\sigma}_0$$

$$\text{AT2:} \quad 2[1-d]\mathscr{H} - \frac{\mathcal{G}_c}{\ell_c}\left[d - \ell_c^2 \operatorname{div}\nabla d\right] = 0$$

$$\text{AT1:} \quad 2[1-d]\mathscr{H} - \frac{3\mathcal{G}_c}{8\ell_c}\left[1 - 2\ell_c^2 \operatorname{div}\nabla d\right] = 0$$

$$\text{where } \mathscr{H}(\boldsymbol{x}, t) = \max_{\tau \in [0,t]} \hat{\psi}_0(\boldsymbol{\varepsilon}(\boldsymbol{x}, \tau))$$

Anisotropic formulation

$$\operatorname{div}\boldsymbol{\sigma} + \hat{\boldsymbol{b}} = 0$$

$$\text{where } \boldsymbol{\sigma}(\boldsymbol{u}, d) = (1-d)^2 \frac{\partial \hat{\psi}_0^+(\boldsymbol{\varepsilon})}{\partial \boldsymbol{\varepsilon}} + \frac{\partial \hat{\psi}_0^-(\boldsymbol{\varepsilon})}{\partial \boldsymbol{\varepsilon}} = (1-d)^2 \boldsymbol{\sigma}^+ + \boldsymbol{\sigma}^-$$

$$\text{AT2:} \quad 2[1-d]\mathscr{H}^+ - \frac{\mathcal{G}_c}{\ell_c}\left[d - \ell_c^2 \operatorname{div}\nabla d\right] = 0$$

$$\text{AT1:} \quad 2[1-d]\mathscr{H}^+ - \frac{3\mathcal{G}_c}{8\ell_c}\left[1 - 2\ell_c^2 \operatorname{div}\nabla d\right] = 0$$

$$\text{where } \mathscr{H}^+(\boldsymbol{x}, t) = \max_{\tau \in [0,t]} \hat{\psi}_0^+(\boldsymbol{\varepsilon}(\boldsymbol{x}, \tau))$$

Hybrid formulation

$$\operatorname{div}\boldsymbol{\sigma} + \hat{\boldsymbol{b}} = 0$$

$$\text{where } \boldsymbol{\sigma}(\boldsymbol{u}, d) = (1-d)^2 \frac{\partial \hat{\psi}_0(\boldsymbol{\varepsilon})}{\partial \boldsymbol{\varepsilon}} = (1-d)^2 \boldsymbol{\sigma}_0$$

$$\text{AT2:} \quad 2[1-d]\mathscr{H}^+ - \frac{\mathcal{G}_c}{\ell_c}\left[d - \ell_c^2 \operatorname{div}\nabla d\right] = 0$$

$$\text{AT1:} \quad 2[1-d]\mathscr{H}^+ - \frac{3\mathcal{G}_c}{8\ell_c}\left[1 - 2\ell_c^2 \operatorname{div}\nabla d\right] = 0$$

$$\text{where } \mathscr{H}^+(\boldsymbol{x}, t) = \max_{\tau \in [0,t]} \hat{\psi}_0^+(\boldsymbol{\varepsilon}(\boldsymbol{x}, \tau))$$

5.2.7 FE-formulations

The Euler-Lagrange equations, i.e. the strong forms, in Eq. 22 and 23 together with the boundary conditions in Eq.24, can be solved using the finite element (FE) method. Using Voight notation, the displacement field $\mathbf{u}$ and the phase field d can be discretized by

$$\mathbf{u} = \sum_{i=1}^{nnode} \mathbf{N}_i^{\mathbf{u}} \mathbf{u}_i \quad \text{and} \quad d = \sum_{i=1}^{nnode} N_i d_i \tag{25}$$

where $\mathbf{u}_i = \{u_x, u_y\}^T$ and d_i are the displacement and phase field values at node i. N_i is the shape functions associated with node i and $nnode$ is the number of nodes for each element [5, 25]. The discretizations of the derivatives of the displacement and phase field are expressed as

$$\nabla \mathbf{u} = \boldsymbol{\varepsilon} = \sum_{i=1}^{nnode} \mathbf{B}_i^{\mathbf{u}} \mathbf{u}_i \quad \text{and} \quad \nabla d = \sum_{i=1}^{nnode} \mathbf{B}_i^{d} d_i \tag{26}$$

where the strain components are defined as $\boldsymbol{\varepsilon} = \{\varepsilon_{xx}, \varepsilon_{yy}, 2\varepsilon_{xy}\}^T$. The shape function matrix and the corresponding derivatives are defined as

$$\mathbf{N}_i^{\mathbf{u}} = \begin{bmatrix} N_i & 0 \\ 0 & N_i \end{bmatrix} \qquad \mathbf{B}_i^{\mathbf{u}} = \begin{bmatrix} N_{i,x} & 0 \\ 0 & N_{i,y} \\ N_{i,y} & N_{i,x} \end{bmatrix} \qquad \mathbf{B}_i^{d} = \begin{bmatrix} N_{i,x} \\ N_{i,y} \end{bmatrix}. \tag{27}$$

The virtual quantities $\delta\mathbf{u}$ and δd included in the weak form must also be discretized. The quantities, together with their derivatives are discretized by

$$\delta \mathbf{u} = \sum_{i=1}^{nnode} \mathbf{N}_i^{\mathbf{u}} \delta \mathbf{u}_i \quad \text{and} \quad \delta d = \sum_{i=1}^{nnode} N_i \delta d_i \tag{28}$$

$$\nabla \delta \boldsymbol{u} = \delta \boldsymbol{\epsilon} = \sum_{i=1}^{nnode} \mathbf{B}_i^{\boldsymbol{u}} \delta \mathbf{u}_i \quad \text{and} \quad \nabla \delta d = \sum_{i=1}^{nnode} \mathbf{B}_i^{d} \delta d_i. \tag{29}$$

Using this FE discretization, the weak forms can be used to express the residuals for the problem. The weak form in Eq. 20 is discretized to the residual of displacement field, presented in Eq. 30. The weak forms in Eq.

21 are discretized to the residuals of phase field, presented for each crack density function in Eq. 31.

$$\bar{r}_i^{\mathbf{u}} = \int_{\mathcal{B}} \left[(1-d)^2\right] \left(\mathbf{B}_i^{\mathbf{u}}\right)^T \boldsymbol{\sigma}_0 \, \mathrm{d}V - \int_{\mathcal{B}} \left(\mathbf{N}_i^{\mathbf{u}}\right)^T \hat{\boldsymbol{b}} \, \mathrm{d}V - \int_{\partial\mathcal{B}} \left(\mathbf{N}_i^{\mathbf{u}}\right)^T \mathbf{t} \, \mathrm{d}A \quad (30)$$

$$\begin{aligned} \text{AT2: } r_i^d &= \int_{\mathcal{B}} \left\{ -2(1-d)\mathscr{H}^+ N_i + \frac{\mathcal{G}_c}{2\ell_c} \left[2dN_i + 2\ell_c^2 \left(\mathbf{B}_i^d\right)^T \mathbf{B}_i^d \, d_i \right] \right\} \mathrm{d}V \\ \text{AT1: } r_i^d &= \int_{\mathcal{B}} \left\{ -2(1-d)\mathscr{H}^+ N_i + \frac{3\mathcal{G}_c}{8\ell_c} \left[N_i + 2\ell_c^2 \left(\mathbf{B}_i^d\right)^T \mathbf{B}_i^d \, d_i \right] \right\} \mathrm{d}V \end{aligned} \quad (31)$$

5.2.8 Solution Methods

This FE problem, $\boldsymbol{r}^{\mathbf{u}} = 0$ and $\boldsymbol{r}^d = 0$, is solved with an iterative Newton-Raphson scheme. The need of an iterative scheme is due to the fact that the residuals in Eq. 30 and 31 are non-linear [20]. Additionally, there are two different solution schemes that can be used to solve the problem, a monolithic solution scheme or a staggered solution scheme. [20]

The staggered scheme decouples the variables in the coupled displacement-fracture problem and solves them separately [28]. By fixing one of the variable, and solving for the other one, this results in two convex problems instead of the previously non-convex problem [20]. The staggered solution schemes have shown to be very robust, however at a computational cost since the method requires very small load steps [20]. The system of equation for the staggered solution scheme is presented in Eq. 32, where $\mathbf{K}^{\mathbf{uu}}$ and $\mathbf{K}^{dd}$ are the tangent stiffness matrices for the displacement field and the phase field, respectively. The tangent stiffness matrices, for node i, are expressed in Eq. 33 for the displacement variable and in Eq. 34 for the phase field variable for both AT1 and AT2.

$$\begin{Bmatrix} \mathbf{u} \\ d \end{Bmatrix}_{t+\Delta t} = \begin{Bmatrix} \mathbf{u} \\ d \end{Bmatrix}_t - \begin{bmatrix} \mathbf{K}^{\mathbf{uu}} & 0 \\ 0 & \mathbf{K}^{dd} \end{bmatrix}_t^{-1} \begin{Bmatrix} \mathbf{r}^{\mathbf{u}} \\ \mathbf{r}^d \end{Bmatrix}_t \quad (32)$$

$$\boldsymbol{K}_{ij}^{\mathbf{uu}} = \frac{\partial \bar{r}_i^{\mathbf{u}}}{\partial \boldsymbol{u}_j} = \int_{\mathcal{B}} \left[(1-d)^2\right] \left(\mathbf{B}_i^{\mathbf{u}}\right)^T \mathbb{C} \, \mathbf{B}_j^{\mathbf{u}} \, \mathrm{d}V \quad (33)$$

$$
\begin{aligned}
\text{AT2: } \boldsymbol{K}_{ij}^{dd} &= \frac{\partial r_i^d}{\partial d_j} = \int_{\mathcal{B}} \left\{ \left[\frac{\mathcal{G}_c}{\ell_c} + 2\mathscr{H}^+ \right] N_i N_j + \mathcal{G}_c \ell_c \left(\mathbf{B}_i^d \right)^T \mathbf{B}_j^d \right\} \mathrm{d}V \\
\text{AT1: } \boldsymbol{K}_{ij}^{dd} &= \frac{\partial r_i^d}{\partial d_j} = \int_{\mathcal{B}} \left\{ 2\mathscr{H}^+ N_i N_j + \frac{3}{4} \mathcal{G}_c \ell_c \left(\mathbf{B}_i^d \right)^T \mathbf{B}_j^d \right\} \mathrm{d}V
\end{aligned}
\tag{34}
$$

The alternative, the monolithic solution scheme, presented in Eq. 35, solves for the variables d and $\boldsymbol{u}$ simultaneously, i.e. the non-convex problem [20]. The non-convexity can cause problem with convergence. To counteract this problem, a quasi-Newton method can be used together with the monolithic solution scheme. The Broyden-Fletcher-Goldfarb-Shanno (BFGS) algorithm is an example of a quasi-Newton method [20]. The Newton-Raphson method updates the stiffness matrix after each iteration, the BFGS algorithm does not. Instead, an approximated stiffness matrix is used when convergence has not been reached with a set number of iterations [20]. By using this algorithm, the update of approximated stiffness couples the two fields, which means that the system of equations can initially be expressed as the staggered solution scheme in Eq. 32 instead of the monolithic scheme without the BFGS algorithm, as seen in Eq. 35 [20]. The difference is the off-diagonal matrices $\mathbf{K}^{\mathbf{u}d}$ and $\mathbf{K}^{d\mathbf{u}}$. The BFGS algorithm is implemented in Abaqus' quasi-Newton solver. A monolithic solution scheme with a quasi-Newton method is faster than the staggered scheme. The load steps used can be larger, which is a great advantage of the monolithic solution.

$$
\begin{gathered}
\begin{Bmatrix} \mathbf{u} \\ d \end{Bmatrix}_{t+\Delta t} = \begin{Bmatrix} \mathbf{u} \\ d \end{Bmatrix}_t - \begin{bmatrix} \mathbf{K}^{\mathbf{uu}} & \mathbf{K}^{\mathbf{u}d} \\ \mathbf{K}^{d\mathbf{u}} & \mathbf{K}^{dd} \end{bmatrix}_t^{-1} \begin{Bmatrix} \mathbf{r}^{\mathbf{u}} \\ \mathbf{r}^{d} \end{Bmatrix}_t \\
\text{where } \boldsymbol{K}_{ij}^{\mathbf{u}d} = \frac{\partial \bar{r}_i^{\mathbf{u}}}{\partial d_j} \text{ and } \boldsymbol{K}_{ij}^{d\mathbf{u}} = \frac{\partial r_i^d}{\partial \boldsymbol{u}_j}
\end{gathered}
\tag{35}
$$

6 Method

The project is carried out in three steps. First, a PF framework is implemented to combine and merge different methods and functionalities into a single code. The framework is based on open source codes published in the literature. To test and evaluate the framework, three benchmark tests commonly used in the literature are performed, as a second step. The last step includes simulations of crack propagation in microstructural models of cortical bone. The models are based on the XFEM-models from the study by Gustafsson et al. [15]. Crack propagation in the cortical bone models is investigated using different material parameters, geometries and levels of porosity.

6.1 The Phase Field Framework

6.1.1 User Subroutines in Abaqus

An implementation of the PF method is missing in commercial computational tools, as mentioned earlier. Although, using *Abaqus*, the PF method can be implemented by using the option of user subroutines. The user subroutine user-defined element (UEL), allows the user to implement calculations for the stiffness matrices and the nodal force vectors. Implementing the PF method using user subroutines in *Abaqus* has been done by for example Molnár and Gravouil [28], Martínez-Pañeda et al. [25], Kristensen and Martínez-Pañeda [20] and Navidtehrani et al. [31]. All of the studies mentioned have published open source code of their implementations. This thesis is also using the option of user subroutines in *Abaqus* in order to implement the PF method. It is based on the open source code by Martínez-Pañeda et al. [25] and Kristensen and Martínez-Pañeda [20]. The implementation also takes inspiration from of the work by Navidtehrani et al. [31]. The UEL elements created in the subroutine are two-dimensional isoparametric linear quadrilateral elements, and therefore has four integration points. The elements have three degrees of freedom for each node, the displacement in the x- and y-direction and the phase field variable.

Only information regarding the stiffness matrix and the nodal force vector is transferred as output from the UEL subroutine in *Abaqus*. No information

regarding stresses and strains are transferred. The definition of the shape functions used for the UEL elements is not transferred either. This is a disadvantage of using user subroutines, however can be overcome by introducing a visual mesh. The visual mesh, which is an idea adopted from Martínez-Pañeda et al. [25], uses the same element nodes and integration points as the original mesh. The visual mesh uses standard *Abaqus* elements (in this thesis CPE4) instead of UEL elements in order to visualize the output. The output parameters (e.g. stress and strain components and the phase field parameter d) are transferred using the user material subroutine (UMAT). The visual mesh have no impact on the solution, because the constitutive matrix and the stress components for the visual elements are set to zero [25]. Fortran is used to implement the user subroutines UEL and UMAT. For more details regarding the subroutines UEL and UMAT, the reader is referred to the documentation following the open source code by Martínez-Pañeda et al. [25] and *Abaqus*-documentations.

6.1.2 Added Functionalities and Solution Flags

The codes provided by Martínez-Pañeda et al. [25] used a staggered solution scheme and Kristensen and Martínez-Pañeda [20] used a monolithic solution scheme based on quasi-Newton method. The codes only implemented AT2 as the crack density function, and no split of the strain energy density was included. The first focus of this thesis is creating a framework using the code by Martínez-Pañeda et al. [25] as a base, but with added functionalities.

A summary of the functionalities added to the PF framework can be seen in Fig. 13. The green boxes represents the original code, and the functionality implemented by Martínez-Pañeda et al. [25]. The yellow, red and blue box represents the added functionalities within the work performed in this thesis. To make a choice of which functionality to use (solution scheme, crack density function and split of the strain energy), solution flags are introduced. They are defined via the material parameters belonging to the UEL elements in the *Abaqus* input-file.

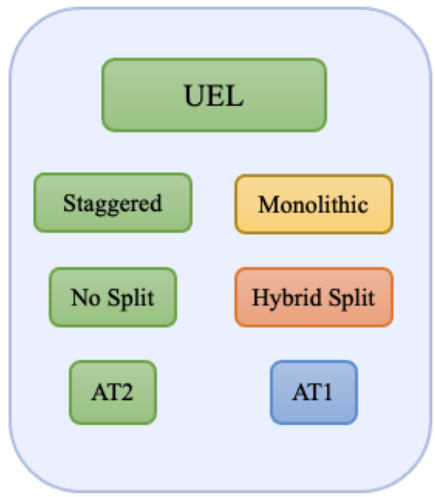

Figure 13: A summary of the implemented PF framework. The green boxes represents the original code by Martínez-Pañeda et al. [25]. The yellow box is monolithic scheme implemented based on the code provided by Kristensen and Martínez-Pañeda [20]. The Hybrid Split, which is the red box, is the volumetric-deviatoric split using the hybrid formulation. It is implemented in this PF framework with inspiration from Navidtehrani et al. [31]. Lastly, the blue box represents the crack density function AT1 which is also implemented in this PF framework.

By combining the code by Martínez-Pañeda et al. [25] and the code by Kristensen and Martínez-Pañeda [20], the PF framework can use both a staggered scheme and monolithic scheme. The choice is made by the solution method flag (of 0 or 1). The monolithic scheme is represented by the yellow box in Fig. 13.

The second crack density function AT1 is also added as an option, by using another solution flag, called crack functional flag. It is represented by the blue box in the summary in Fig. 13. The split of the strain energy density is introduced by implementing a function that calculates the crack driving force, which is the history field variable $\mathscr{H}$. The implementation is inspired by the work of Navidtehrani et al. [31]. However, Navidtehrani et al. [31] included both the spectral split by Miehe et al. [26] and the volumetric-deviatoric split by Amor et al. [3], and this thesis only implements the volumetric-deviatoric split which is defined in Eq. 14 in Section 5.2.4. The deviatoric strains in the implemented framework are calculated directly from the strain tensor. In the code by Navidtehrani et al. [31], the deviatoric strains are calculated from the

principal values of the strain tensor using a built-in function in *Abaqus* called SPRINC. Though, this is an unnecessary step since the SPRINC-function at some occasions can produce large principal values, and is therefore not reliable.

The choice of splitting the strain energy density is also made with a solution flag, the split flag. The choice is between a hybrid split or no split. The hybrid split uses the hybrid formulation, where the split of the strain energy is the volumetric-deviatoric split. In Fig. 13, the volumetric-deviatoric split with the hybrid formulation is represented by the red box. A summary of all the solution flags introduced in the PF framework are included in Table 1.

For the hybrid formulation, Ambati et al. [2] included an additional condition. It is supposed to prevent inter-penetration of the crack faces if a compressive load is applied. When a crack is created, the new crack faces are separated by completely degraded elements, i.e. $d = 1$. When the specimen is compressed, the crack faces penetrate each other, as the elements separating them has no stiffness. By setting $d = 0$ for the equations governing the displacement field when $\psi^- > \psi^+$, this can be prevented. However, this criteria can only be implemented successfully in the staggered solution scheme, as the two field are solved separately.

Table 1: A summary of all the solution flags introduced in the PF framework. They are introduced via the material parameters belonging to the UEL elements in the *Abaqus* input-file. It includes the functionality of which solution method to use, which crack density function and whether the strain energy density will be split.

Solution Flags for the Added Functionalities		
Solution Method	Crack Functional	Split of Strain Energy
0 = Monolithic	1 = AT1	0 = No split
1 = Staggered	2 = AT2	1 = Hybrid split (using the volumetric-deviatoric split)

6.1.3 Flow Chart of UEL Subroutine

For a better understanding of how the implemented PF framework works, the code is summarized in the flow chart in Fig. 14. The yellow, red and blue box represents the added functionalities.

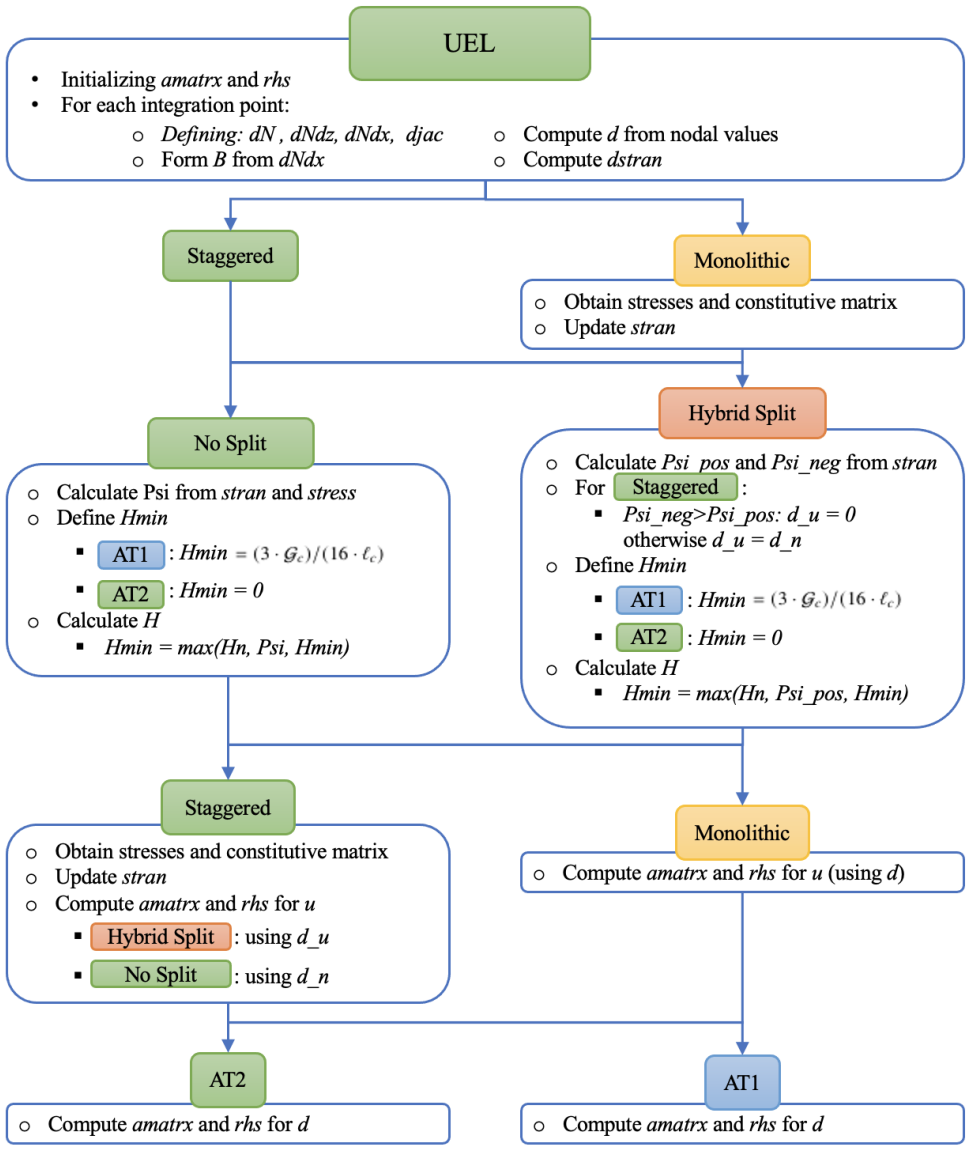

Figure 14: A summary of the code of the PF framework. The colors of the boxes follow the color scheme as in Fig. 13. A description of the variables mentioned in the flow chart is included in Fig. 15.

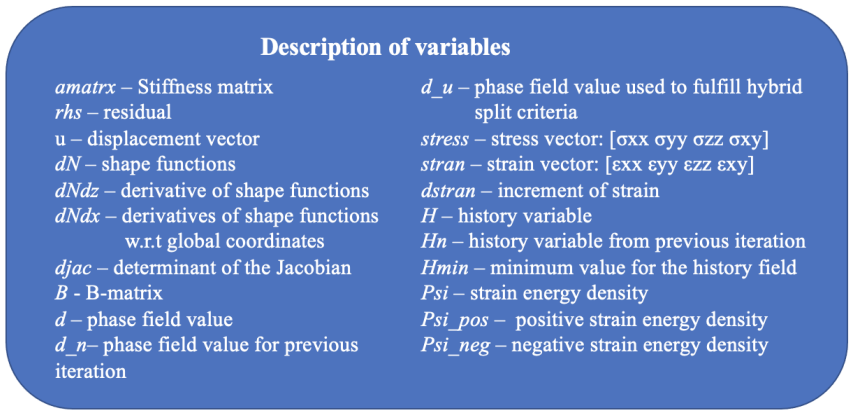

Figure 15: A description of the variables used in the flow chart in Fig. 14.

6.2 Benchmarks

To test and evaluate the implemented PF code, three benchmark tests are run. Two typical benchmarks are the Single-edged notched test (SENT) specimen under tensile load and shear load [20]. The third benchmark is a perforated asymmetric bending test from the study by Molnár and Gravouil [28] and Mandal et al. [24]. The crack density functions AT1 and AT2 are evaluated in the SENT benchmarks, and for the perforated asymmetric bending test, only AT1 is applied. Both the monolithic and staggered solution schemes are used, to evaluate the difference between the two. All benchmark tests are be modelled with a split of the strain energy density. It is a hybrid split, as described in this thesis.

6.2.1 SENT

The first benchmark is the Single-edged notched test (SENT) specimen under tensile load. It is a model that has been widely used [20]. The geometry is a quadratic plate with the a side length of 1 mm (Fig. 16a). The geometrically defined crack is 0.5 mm long and has a width of 0.02 mm at the widest point. The displacement applied to the specimen is $u = 0.01$ mm, which is based on the displacement applied in the study by Kristensen and Martínez-Pañeda [20].

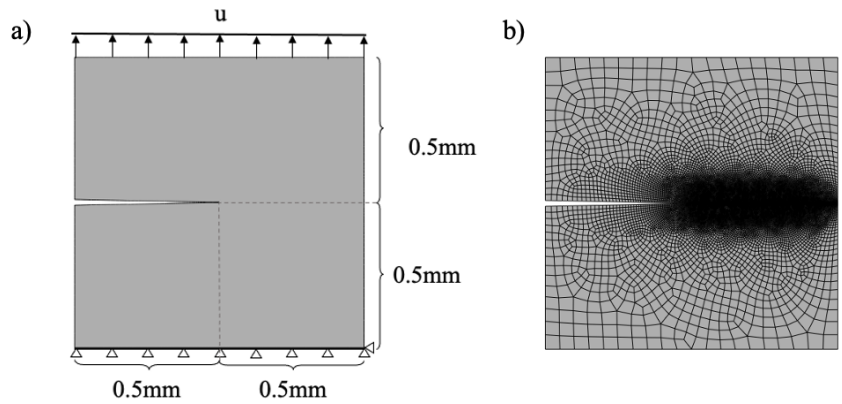

Figure 16: SENT Tensile: a) Geometry with boundary conditions b) Mesh with h = 0.001mm

The model is discretized with linear quadrilateral elements with the smallest mesh size $h = 0.001$ mm along the expected crack path, which is the same value used in the study by Molnár and Gravouil [28]. The mesh used can be seen in Fig. 16b. The material parameters used for the model are listed in Table 2 and the values are adopted from the study by Kristensen and Martínez-Pañeda [20]. Note that the length scale parameter ℓ_c, together with $h = 0.001$ mm fulfills the criteria $h < \ell_c/2$.

Table 2: Material parameters for the SENT Tensile and the SENT Shear. The values are adopted from the study by Kristensen and Martínez-Pañeda [20].

E (MPa)	ν	ℓ_c (mm)	$\mathcal{G}_c$ (N/mm)
210000	0.3	0.024	2.7

The same parameters are also used for the SENT Shear model, which has a shear load applied, which is the second benchmark. The geometry is the same as for the SENT Tensile model, but the boundary conditions differ, as seen in Fig. 17a. The displacement applied to this specimen is $u = 0.02$ mm. This value is chosen based on the displacement applied in the study by Kristensen and Martínez-Pañeda [20]. The mesh, in Fig. 17b is also different. The same type of elements are used to discretize the model, however the smallest mesh size is $h = 0.002$ mm in a square in the lower right corner, which include the expected crack path for this test. This value was used by Mandal et al.

[24], and it also fulfills the criteria $h < \ell_c/2$ for the length scale parameter $\ell_c = 0.024$ mm.

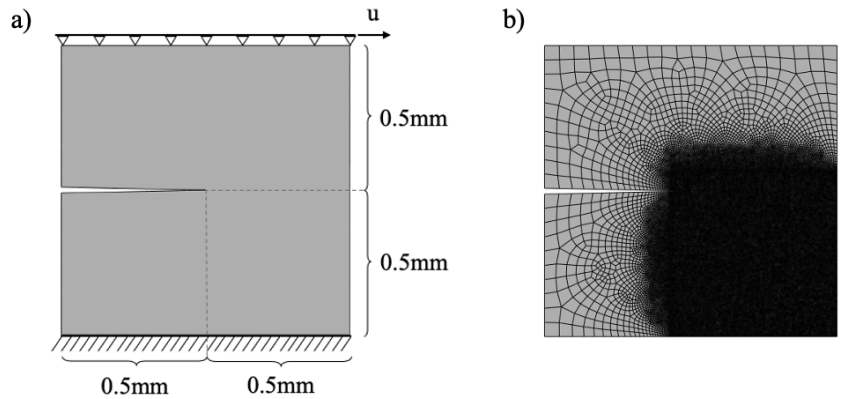

Figure 17: SENT Shear: a) Geometry with boundary conditions b) Mesh with $h = 0.002mm$

Both the staggered solution scheme and the monolithic solution scheme are applied in these tests, both for the SENT Tensile model and the SENT Shear model. In the study by Molnár and Gravouil [28], which used only the staggered scheme, the step size used was $\Delta u = 10^{-4}$ mm and $\Delta u = 10^{-5}$ mm for both the tensile and shear load. The smaller step size was used to be able to clearly and precisely follow the propagation of the crack. For thesis, the step size $\Delta u = 10^{-6}$ mm is used for the SENT Tensile model and $\Delta u = 2 \cdot 10^{-6}$ mm for the SENT Shear model, when solving with the staggered scheme. For the monolithic solution scheme, a larger step size is used. With the monolithic solution, the automatic adaptive step size scheme in *Abaqus* is used. It decreases the step size automatically when a certain number of iterations are needed for the solution to converge. This means that the step size is decreased to capture unstable crack growth more easily [20]. A step size of $\Delta u = 10^{-4}$ mm is used as the base for the SENT Tensile model and $\Delta u = 2 \cdot 10^{-5}$ mm for the SENT Shear model. The smallest step size allowed in the adaptive step scheme is $\Delta u = 10^{-11}$ mm.

The crack density functions, AT1 and AT2, are used for the SENT benchmark tests. The study by Kristensen and Martínez-Pañeda [20] and Molnár and Gravouil [28] only used AT2 for SENT models. AT1 was used by Mandal et al. [24], but only for the SENT Shear model. Generally in literature, AT2 has been used more than AT1. Therefore, this thesis is evaluating both crack

density functions for both SENT models.

6.2.2 Perforated Asymmetric Bending Test

To be able to investigate how holes affect crack propagation, e.g. by seeing how they can cause the crack to deflect, another benchmark test is used. It is a perforated asymmetric bending test, presented in the study by Molnár and Gravouil [28] and Mandal et al. [24]. It based on experiments carried out in the study by Ingraffea and Grigoriu [17]. The geometry is of a rectangular shape perforated with three holes. The geometry with boundary conditions is displayed in Fig. 18. Ingraffea and Grigoriu [17] tested different geometries by alternating the length of the introduced crack as well as its location from the center of the model. The crack paths found in the study by Ingraffea and Grigoriu [17] varied to a large extent, when the introduced crack was only slightly altered. The original geometry is expressed in inches, the length scale presented in Fig. 18 are translated into millimeters. The model is meshed with two types of element. A section of the model, which contains the three perforations, is assigned UEL-elements. The rest of the model has ordinary elements with linear elastic material, and the UEL subroutine is not applied for these elements.

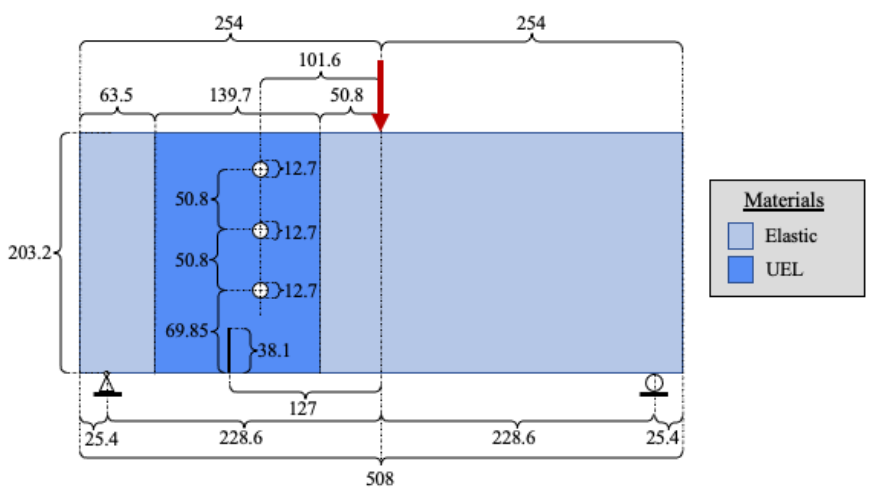

Figure 18: The geometry (unit of length: mm) and boundary conditions for the perforated asymmetric bending test. The geometrically introduced crack is 0.1 mm wide. The model contains both UEL-elements and elastic elements. Drawn based on the measurements in the study by Mandal et al. [24] and translated into millimeters.

The material parameters used for this benchmark are included in Table 3 and are the same values used by Mandal et al. [24]. In the study by Mandal et al. [24], two sets of parameters was used for the length scale parameter ℓ_c and the mesh size h. For the benchmark performed in this work $\ell_c = 1.905$ mm is used together with the mesh size $h = 0.254$ mm. A smaller $\ell_c = 1.27$ mm is also used together with $h = 0.254$ mm. Both values of ℓ_c fulfills the criteria $h < \ell_c/2$. In Fig. 19, the mesh of the model is presented. The mesh size $h = 0.254$ mm is used around the first two holes, where the crack is expected to propagate according to the results presented in the study by Mandal et al. [24]. Bigger elements are used for the elastic elements.

Neither studies by Molnár and Gravouil [28] and Mandal et al. [24] states the displacement applied on the model, which is represented by the red arrow in Fig. 18. In the SENT Tensile model, a displacement of $u = 0.01$mm is applied, which is 1% of the height of the model. Using that reasoning, the displacement applied for this benchmark is $u = 2$ mm. The crack is represented by the crack density function AT1, as it is will used for the cortical bone models.

Table 3: Material parameters for the UEL elements and the elastic elements in the perforated asymmetric bending test. The length scale parameter ℓ_c and the critical energy release rate $\mathcal{G}_c$ is only applied for the UEL elements. Values are from the study by Mandal et al. [24].

	Material Parameters			
Type of Element	E (MPa)	ν	ℓ_c (mm)	$\mathcal{G}_c$ (N/mm)
UEL	3275	0.35	1.905	0.315
Elastic	3275	0.35	-	-

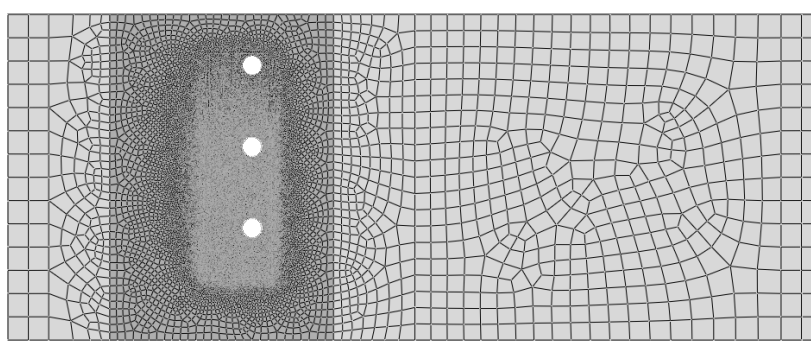

Figure 19: Mesh of the model used for the perforated asymmetric bending test. The mesh size $h = 0.254$ mm is used around the first two holes. The elastic elements are displayed with a light grey color and the UEL elements are displayed in a darker grey color.

6.3 Models of Cortical Bone

6.3.1 Geometry and Boundary Conditions

To create realistic models of human cortical bone, the models are based on microscopy images of a tibial shaft (the shaft of the shinbone). The geometries used are based upon the models used in the XFEM-study by Gustafsson et al. [15] and the pipeline for creating the models are displayed in Fig. 7 in Section 4.4. To use the models with PF instead of XFEM, a few modifications are made. First of all, the elements representing the Haversian canals are removed to create holes in the models. The PF method is not limited to only one active growing crack, and therefore can the canals be modelled as holes in this thesis. Secondly, the XFEM-elements are changed to isoparametric linear quadrilateral UEL elements. A visual mesh is created with *Abaqus*' CPE4-elements, using MATLAB, to be able to visualize the results from the UEL subroutine. The structure of the cortical bone: interstitial matrix, osteons and cement lines, are divided into three element sets. The reason is that different material parameters are given to the different sets. The material parameters used for the models are to be described in the next section.

Two models are used in this thesis: Model A and Model B (Fig. 20). Model A is the 4-osteon model used in the XFEM-study by Gustafsson et al. [15]. Model B is rotated 180° to generate another geometry. The models are of the size 1.2x1.2 mm^2, and have a thickness of 1 mm. The cement lines have a thickness of 5 µm around the osteons. The boundary conditions used for the two models are also presented in Fig. 20, where the displacement applied is u = 0.02 mm. A geometrical crack is also introduced in the models. The crack is of a triangular shape with a height of 0.12 mm high (10 % of the height of the model) and a base of 0.01 mm.

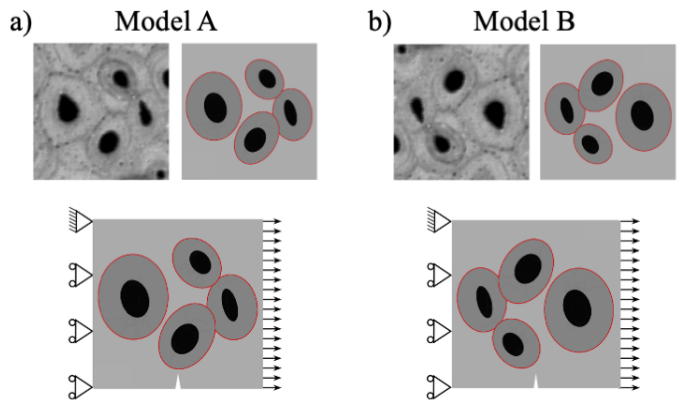

Figure 20: The two models used based on microscopy images. a) Model A and b) Model B. Model B is rotated 180° compared to Model A. Boundary conditions for each model are presented as well. The interstitial matrix is represented by the light grey area. The cement lines are marked with red, and the Haversian canals are the black holes. The grey area surrounding the Haversian canals are the osteons.

The cortical bone models are in first hand run with the monolithic solution scheme. As mentioned earlier, the monolithic scheme do not always converge, due to the non-convexity of the coupled problem. If problems with convergence occur, the staggered solution scheme is used instead. The staggered scheme is robust though computationally demanding due to small step size required. The step size used for the two schemes is based on the results from a sensitivity analysis of the step size. The same applies for the mesh, a sensitivity analysis of the mesh size is also performed. Also, the hybrid split described in this thesis is used within the PF framework for the cortical bone models. It hinders crack growth during compression and saves computational time compared to the anisotropic formulation [2].

Even if the crack density function AT2 is more used in the literature, AT1 is used for the cortical bone models in this thesis. When using AT2, the damage in the model starts as soon as the load is applied. When using AT1, there is an initial elastic region before damage is initiated. In the work by Carlsson [6], AT1 was used to model fracture in microstructure of wood. In this thesis, the microstructure of the cortical bone is modelled and the brittle response expected in the bone tissue is better described by AT1, and is therefore used.

6.3.2 Material Parameters

The individual mechanical properties of the matrix, osteons and cement lines have been difficult to experimentally determine. Thus, in literature, the values used as material parameters in computational studies have not been consistent [10].

In the study by Gustafsson et al. [16], a literature review was performed to summarize the numerical and experimental findings regarding the material parameters of the interstitial matrix, the osteons and the cement lines. This thesis is using parameters that are based on this summary as well as the material parameters used in the XFEM study by Gustafsson et al. [15] and the PF study by Maghami et al. [23]. A summary of the material parameters used in this thesis for the cortical bone models are presented in Table 4.

Table 4: The material parameters used for the cortical bone models.

	Material Parameters			
	E (MPa)	ν	$\mathcal{G}_c$ (N/mm)	ℓ_c (μm)
Matrix	15 000	0.3	0.4	3.75
Osteon	12 000	0.3	0.48	3.75
Cement line	18 000	0.3	0.13	3.75

Firstly, the values for the Young's modulus and the Poisson's ratio of the interstitial matrix, osteon and cement lines are the same as the values used in the XFEM study [15]. The stiffness for the matrix is 20% higher than for the osteons, and the stiffness for the cement lines is 20% higher than for the matrix.

The values for the critical energy release rate $\mathcal{G}_c$ are more difficult to choose. In the summary by Gustafsson et al. [16], the experimental values for $\mathcal{G}_c$ for the matrix is in the range 0.05-0.8 N/mm. The XFEM-study [15] used $\mathcal{G}_c = 0.4$ N/mm for the matrix, and is the value used in this thesis as well. The same value is chosen to be able to compare the results to the XFEM-models by Gustafsson et al. [15]. The experimental results from Mullins et al. [30] are included in the summary [16]. Mullins et al. [30] concludes that $\mathcal{G}_c$ for the osteons are greater than for the matrix. In the computational study by Maghami et al. [23], $\mathcal{G}_c$ for the osteons is 20% higher than $\mathcal{G}_c$ for the matrix. The same ratio is used for the values in this thesis.

The critical energy release rate $\mathcal{G}_c$ for the cement lines is not well documented in the literature since it is difficult to determine. Giner et al. [10] estimated the value with a numerical model calibrated to experimental findings, as described in Section 4.4. The estimated value was the average value in the study, which is $\mathcal{G}_c = 0.1629$ N/mm. The study by Maghami et al. [23] adopted this value in their work and the value was approximately 70% lower than the value used for the matrix. For this thesis, the same ratio is used to calculate the $\mathcal{G}_c$ for the cement lines from $\mathcal{G}_c = 0.4$ N/mm for the matrix, i.e. $\mathcal{G}_c = 0.13$ N/mm. Though, for the sensitivity analysis of the mesh and step size, $\mathcal{G}_c$ for the cement lines is 0.17 N/mm. It is a value that lies within the range estimated and presented in the study Giner et al. [10].

The length scale parameter ℓ_c must be carefully chosen. First of all, it must fulfill the criteria which relates to the mesh size: $h < \ell_c/2$ [26]. The reason is that the mesh must be able to resolve the crack width, and that is difficult if the mesh size h is too big compared to ℓ_c. Secondly, the length scale parameter must be smaller than the width of the cement lines in order for the crack to properly propagate inside the lines. The mesh must also be chosen with the width of the cement lines in mind, which is investigated in the sensitivity analysis of the mesh.

In the study by Maghami et al. [23], the width of the cement lines were also 5 µm and the length scale parameter $\ell_c = 3.4$ µm was used. In an ongoing study by Gustafsson, models using the length scale parameter $\ell_c = 3.75$ µm converged and fulfilled the criteria $h < \ell_c/2$. Therefore, this thesis is using $\ell_c = 3.75$ µm.

6.3.3 Sensitivity Analysis of Mesh and Step Size

The PF method is sensitive towards both the mesh and the step size used, and therefore a sensitivity analysis of both the mesh and the step size must be performed. For this part, Model B in Fig. 20b is used. The material parameters in Table 4 is used expect that $\mathcal{G}_c = 0.17$ N/mm for the cement lines.

The Sensitivity Analysis of Mesh

The sensitivity of the mesh is evaluated by testing different sizes of the

elements which is described by h, the smallest mesh size used in the region where the cracks are expected to propagate. The mesh size must fulfill the criteria $h < \ell_c/2$, and must also be sufficiently refined to resolve the cement lines. The cement lines for the cortical bone models used in this thesis are 5 µm wide and the length scale parameter uses is $\ell_c = 3.75$ µm. Three different meshes with different values of h are used, and are presented in Table 5. For visualization, Model B with three meshes is displayed in Fig. 21. Note that the smallest elements are concentrated to the structure of the osteons and bigger elements are used in the periphery of the models. Hence, the mesh size h is used where the cracks are expected to propagate. The meshes are chosen based on how many elements the cement lines are discretized with, see Table 5. The width of the cement line is made up of 2, 3 or 4 elements, as can be seen in Fig. 21. The coarsest mesh do not fulfill the criteria $h < \ell_c/2$, but the two finer meshes do. The analysis is performed using both the monolithic and the staggered solution scheme. The step size used is based on the sensitivity analysis of the step size.

Table 5: A summary of the three mesh sizes h used for the sensitivity analysis of the mesh. The number of elements which the cement lines are discretized with are included, and if the value of h fulfills the criteria connected to the length scale parameter $\ell_c = 3.75$ µm.

Mesh size h (µm)	No. of elements in the cement lines	ℓ_c/h	Fulfills the criteria $h < \ell_c/2$
2.5	2	1.5	No
1.67	3	2.2	Yes
1.25	4	3.0	Yes

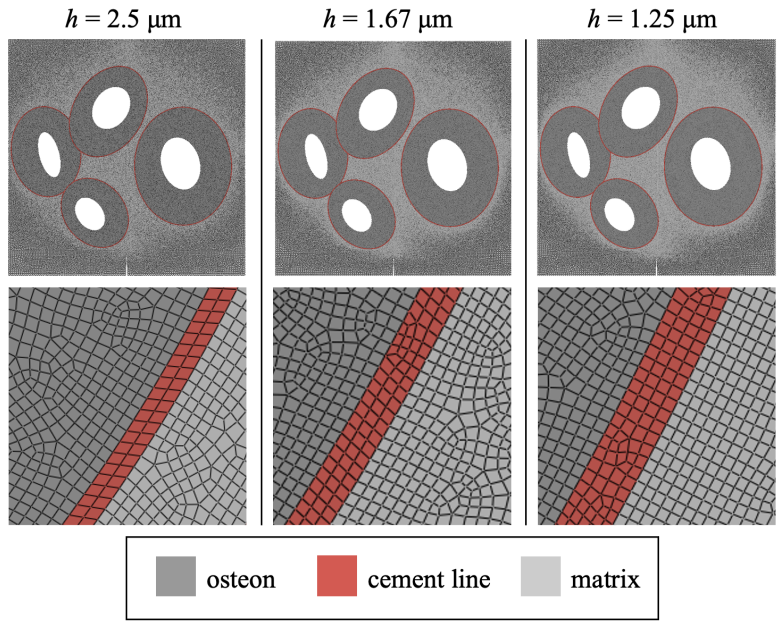

Figure 21: Model B meshed with the three mesh sizes: $h = 2.5$ µm, $h = 1.67$ µm and $h = 1.25$ µm. The number of elements used to discretize the cement lines can also be seen. The interstitial matrix are represented by the light grey elements, the osteons are represented by the darker grey elements and the cement lines are represented by the red elements.

The Sensitivity Analysis of Step Size

The sensitivity analysis of the step size is analyzed using $h = 2.5$ µm. The step size is of importance for both the monolithic and the staggered solution scheme, where the latter needs very small steps. The different step sizes used in the analysis are presented in Table 6. In the study by Maghami et al. [23], which uses a staggered solution scheme, uses a step size in the order of 10^{-5} and 10^{-6}. The values for Δu used for this analysis are of the same order for the staggered scheme. For the monolithic scheme, greater step sizes are used. The monolithic solution scheme used is also paired with the adaptive step size scheme in *Abaqus* as described earlier. The smallest step size allowed is $\Delta u = 10^{-11}$ mm.

To determine which step size to use for the rest of the analysis, a convergence check can be performed. By performing a convergence check, an optimal step size can be determined. The idea of convergence is that by decreasing the step size, the solution tends to one specific value. However, in this

case, it is not a specific value, it is rather a specific mechanical response in the material. The convergence check for the step size, in this thesis, is firstly based on the resulting crack paths in the beginning of the propagation. Model B used in this analysis includes an osteon close to the crack tip of the geometrically introduced crack, therefore the convergence check is based on how the cracks advance through the first osteon. The force-displacement curves of the models are analyzed to determine convergence. In the study by Kristensen and Martínez-Pañeda [20], the staggered solutions became closer to the monolithic solutions when the step size was decreased for the SENT benchmarks. The monolithic solutions, in the study by Kristensen and Martínez-Pañeda [20], resulted in force-displacement curves with sharp fracture points and brittle behaviour. This behaviour is sought for when determining convergence of the step size.

Table 6: A summary of the step sizes Δu used for the sensitivity analysis of the step size. Both the monolithic and staggered solution scheme are included.

Step size Δu (mm)				
Monolithic		Staggered		
$2 \cdot 10^{-4}$	$1 \cdot 10^{-5}$	$2 \cdot 10^{-5}$	$2 \cdot 10^{-6}$	$2 \cdot 10^{-7}$

6.3.4 Analysis of Material Parameters

Since the material parameters used to model cortical bone varies in computational studies, it is important to investigate if the chosen parameters in this study have an effect on crack growth. Therefore, this thesis includes an analysis of the material parameters. Model A and B are tested for three different sets of material properties:

Set 1: The standard material parameter summarized in Table 4.

Set 2: The critical release rate $\mathcal{G}_c$ for the osteons is altered: $\mathcal{G}_c^{\text{osteon}} = \mathcal{G}_c^{\text{matrix}} = 0.4$ N/mm.

Set 3: Homogeneous material. The material parameters used for the cement lines, osteons and matrix are the same. The material parameters of the matrix is used.

The first set is the standard material parameters in this thesis which are outlined in Table 4. For the second set, the critical energy release rate $\mathcal{G}_c$ for the osteons is altered. It is set to be $\mathcal{G}_c = 0.4$ N/mm, which is the value used for the matrix. The experimental study by Mullins et al. [30] found that $\mathcal{G}_c$ was the highest for the osteons. Set 2 can therefore provide information if the difference in $\mathcal{G}_c$ for the osteon and matrix affects the crack propagation. For the third and last set, the models are assumed to be homogeneous. This is done by using the material properties of the matrix for the osteons and cement lines as well. By assuming a homogeneous model, only the Haversian canals should influence that crack path. By testing the three sets on both Model A and Model B, the effect of the geometry can also be analyzed.

6.3.5 The Effect of Geometry

To investigate how the porosity of the bone tissue affects the crack propagation in cortical bone, three different microstructures are tested. As the bone mass decreases with age, by for example increasing porosity, the investigation can give an insight in how age and the change in microstructure affect the crack propagation and behaviour [32].

Model A in Fig. 20a is used in this analysis, and it has a porosity of 7%. By changing the size of the Haversian canals, the porosity of Model A can be altered. Two additional models are therefore created with a porosity of 15% and 0%. The percentage is based on the area of the Haversian canals compared to area of the whole model. 0% means that the Haversian canals are filled with osteonial material, and it is purely a theoretical model.

One advantage of the PF method is its ability to model crack initiation. To test it, this thesis is using models with a geometrically introduced crack and models without. The models, presented in Fig. 22a-c, have a geometrical crack introduced. For the models in Fig. 22d-f, the geometrically introduced crack is excluded. The same percentage of porosity is used for both types of models.

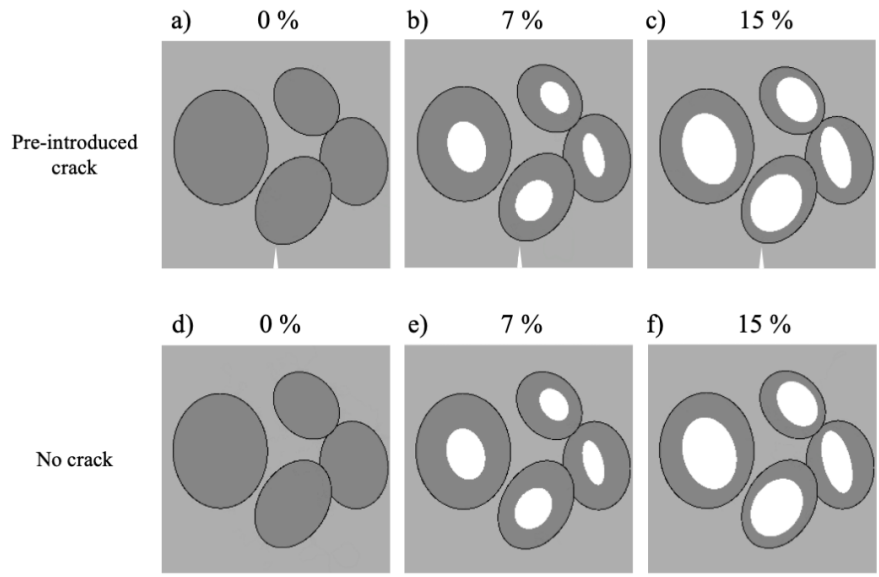

Figure 22: Model A with different porosity: 0% [a) & d)], 7% [b) & e)] and 15% [c) & f)]. a)-c) A geometrical crack is introduced. e)-f) No geometrical crack is introduced.

7 Results

7.1 Benchmarks

7.1.1 SENT Tensile

The crack paths for the staggered and monolithic solution method are almost identical, for both AT1 and AT2 (Fig. 23). The difference is that the staggered solution method results in a wider crack, with a smeared effect (Fig. 23b and 23d). This small difference between the solution schemes can also be seen in force-displacement curves in Fig. 23e, as the staggered solution results in a greater maximum force and also deforms more. The fracture point for the monolithic solution is also more distinct than the staggered solution.

AT2 is more smeared than AT1, although the crack paths are almost identical (Fig. 23). The force-displacement curves for AT1 display a more linear behaviour compared to AT1 (Fig. 23e), with a higher maximum force, whereas the maximum deformation is higher in AT2.

The crack paths in Fig. 23 are corresponding well to results from the literature presented in Fig. 24. The crack path in Fig. 24a, which used the same monolithic method as this thesis, is identical to the crack path in Fig. 23c. The model in Fig. 24b used a staggered solution scheme, and the resulting crack path is similar to the crack paths in Fig. 23b and 23d. However, the crack in Fig. 24b is more narrow, and the reason is that the length scale parameter used was three times smaller. The force-displacement curves for the SENT Tensile model (Fig. 23e) display the same non-linear behaviour for AT2 as the curves in Fig. 24c, with the same maximum displacement for the monolithic solution. The curves for the staggered solutions tend towards the curve of the monolithic solution with increasing number of increments, i.e. decreasing step size (Fig. 24c).

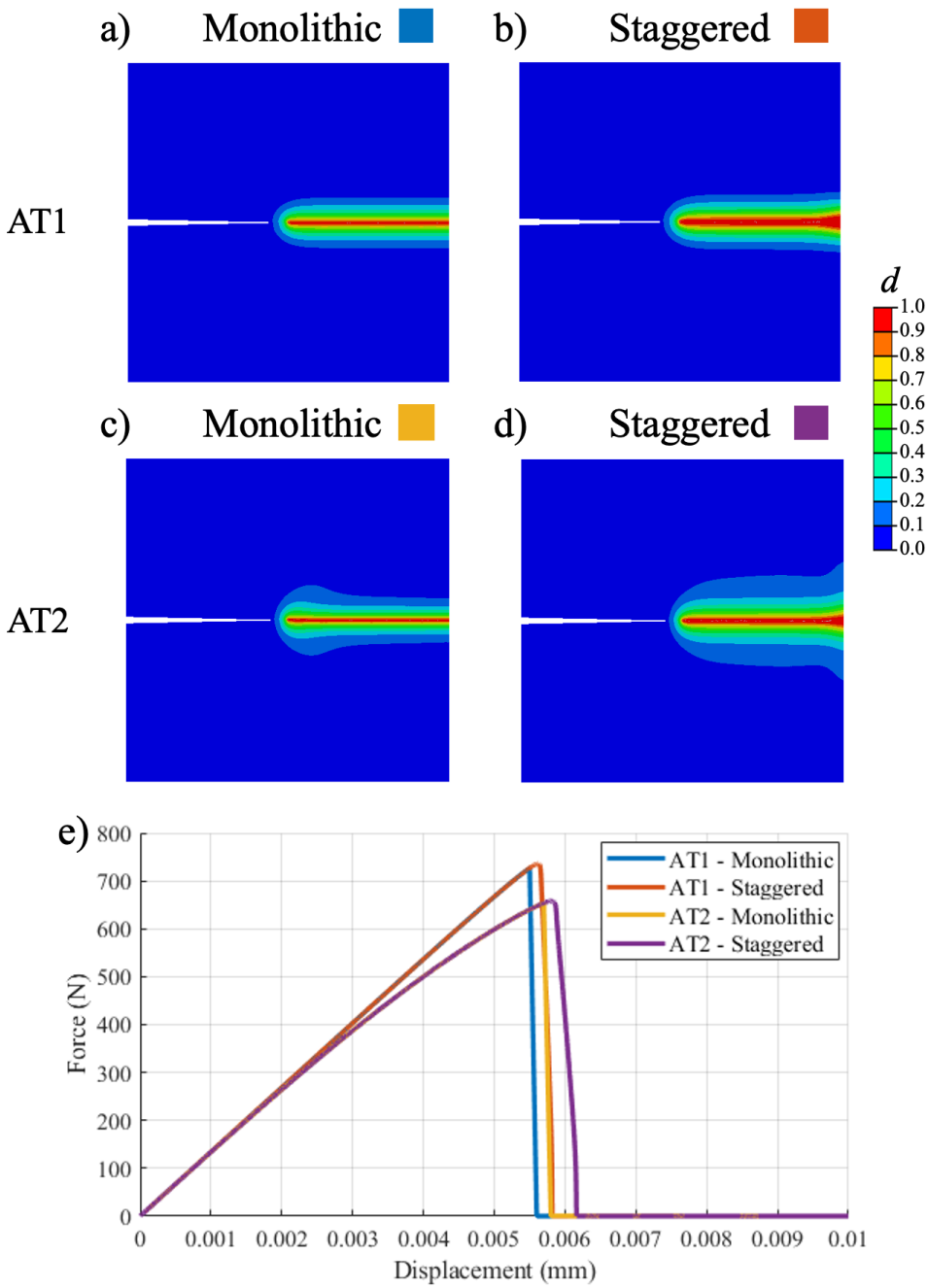

Figure 23: The resulting phase field d for the SENT Tensile model. a)-b) Crack density function AT1. c)-d) Crack density function AT2. e) The corresponding force-displacement curves. a) and c) Monolithic solution with $\Delta u = 10^{-4}$ mm. b) and d) Staggered solution with $\Delta u = 10^{-6}$ mm. $d = 0$ represents intact material and $d = 1$ represents broken material.

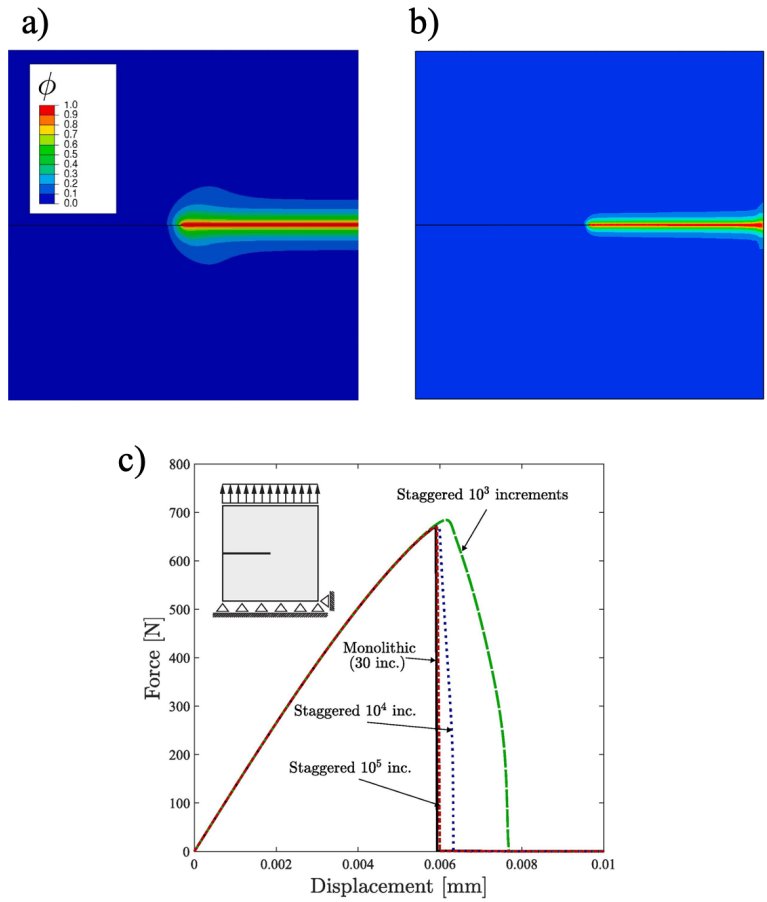

Figure 24: Results for the SENT Tensile Model using AT2 from the literature. a) The resulting phase field d, here denoted as ϕ, from the study by Kristensen and Martínez-Pañeda [20]. b) The resulting phase field d from the study by Molnár and Gravouil [28]. c) The corresponding force-displacement curve for a). The same material parameters as presented in Table 2 were used, except that $\ell_c = 0.0075$ mm in b). Figures a)-c) are reprinted with permission from Elsevier.

7.1.2 SENT Shear

The difference between the two solution methods for SENT Shear model is the smeared effect of the staggered solution scheme (Fig. 25b and 25d). Beyond that, the crack paths in Fig. 25a-b are similar, and propagate with approximately the same angle from the crack tip of the geometrically induced crack. The same can be said for the crack paths in Fig. 25c-d. The force-

displacement curves for the two solution schemes are also similar to each other, where the maximum forces are equal and they follow the same pattern (Fig. 25e). The difference is that the staggered solution allows the model to deform more, which is the behaviour observed for the SENT Tensile model as well.

The crack paths, when comparing AT1 and AT2, are different (Fig. 25). The crack paths are more curved for AT2 than for AT1, and the cracks are also wider. The difference is also clear in the force-displacement curves in Fig. 25e. The curves for AT1 are more linear in the beginning, and the curves for AT2 are more non-linear. For AT2, the maximum force is lower and the model is allowed to deform more. The fracture points are more distinct when using AT1 as the crack density function.

For a comparison to the literature, the straighter crack paths of AT1 (Fig. 25a-b) can also be seen in the results from Kristensen and Martínez-Pañeda [20] and from Mandal et al. [24] (Fig. 26). The force-displacement curves for the SENT Shear model (Fig. 25e) display the same non-linear behaviour for AT2 as the curves in Fig. 26d, with the same maximum displacement. The smeared effect of AT2 (Fig. 25c-d) can be seen in the results from Mandal et al. [24] (Fig. 26a-b) which also used both crack density functions.

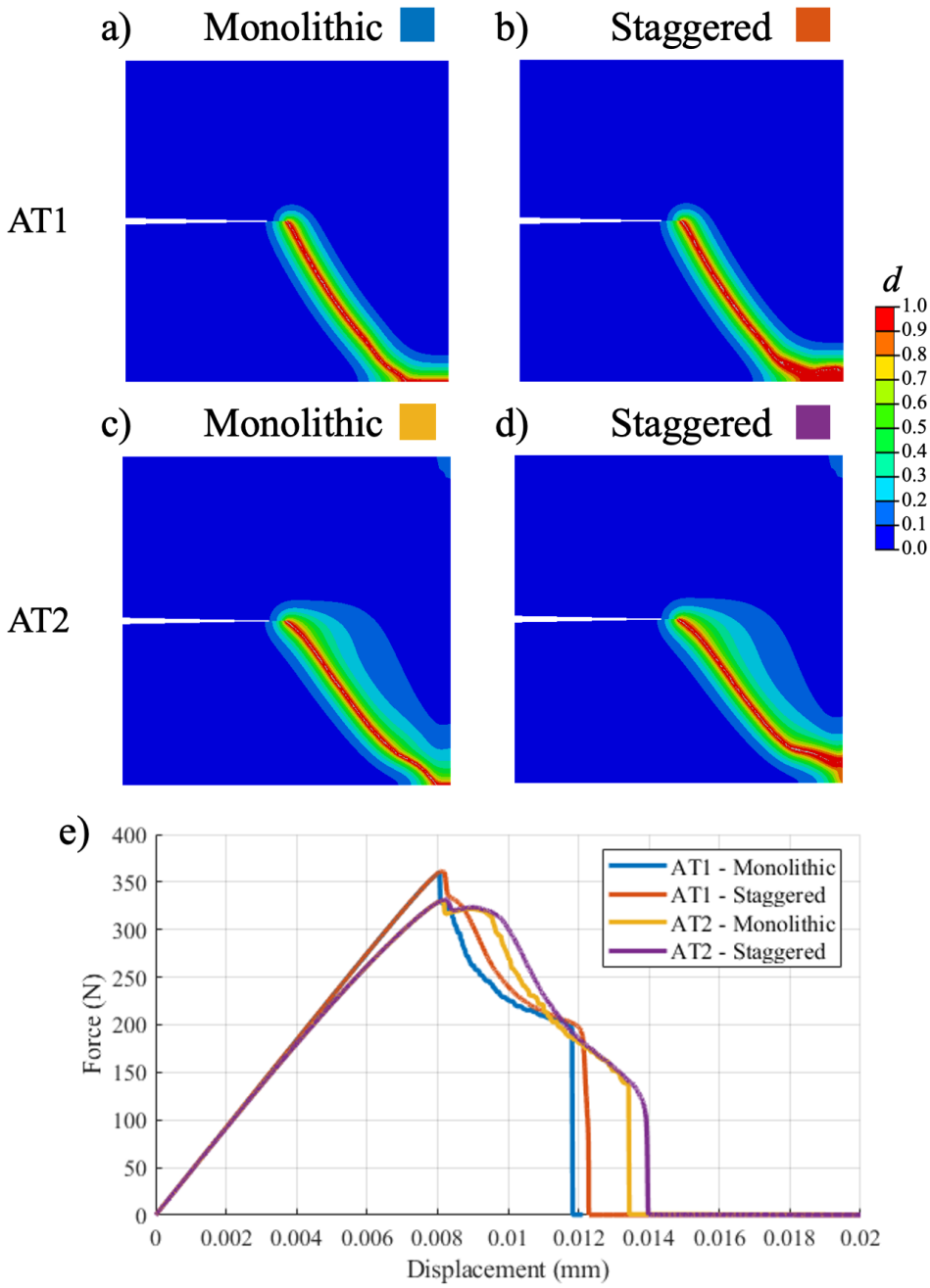

Figure 25: The resulting phase field d for the SENT Shear model. a)-b) Crack density function AT1. c)-d) Crack density function AT2. e) The corresponding force-displacement curves. a) and c) Monolithic solution with $\Delta u = 2 \cdot 10^{-5}$ mm. b) and d) Staggered solution with $\Delta u = 2 \cdot 10^{-6}$ mm. $d = 0$ represents intact material and $d = 1$ represents broken material.

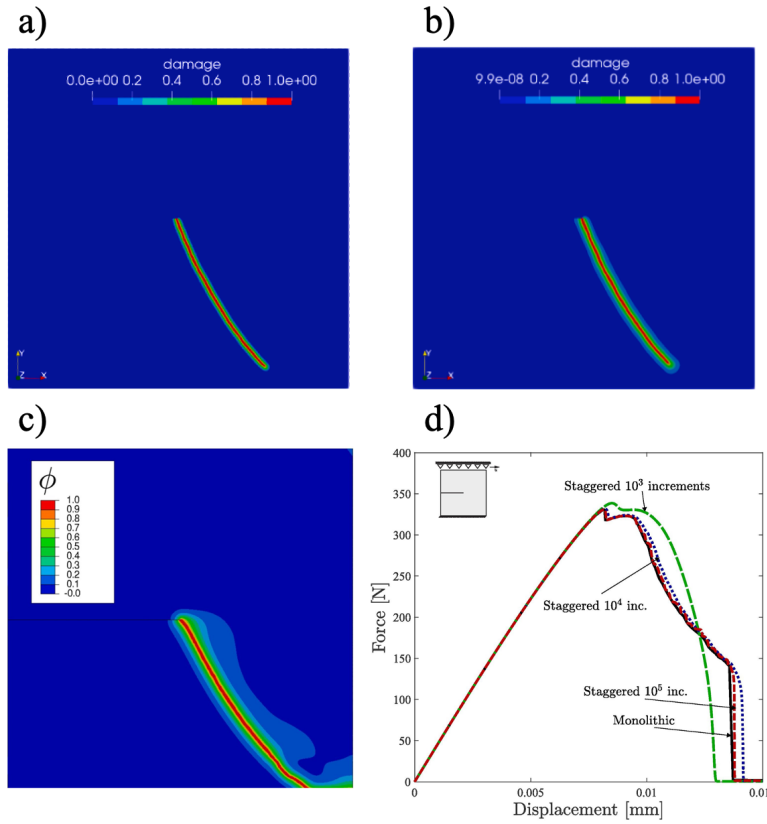

Figure 26: Results for the SENT Shear Model from the literature. The resulting phase field from the study by Mandal et al. [24] using the crack density function a) AT1 and b) AT2. c) The resulting phase field d, here denoted as ϕ, from the study by Kristensen and Martínez-Pañeda [20] using AT2 and the corresponding force-displacement curve in d). The same material parameters as presented in Table 2 are used, except $\ell_c = 0.01$ mm in a)-b). Figures a)-d) are reprinted with permission from Elsevier.

7.1.3 Perforated Asymmetric Bending Test

When running this benchmark, the monolithic solution method had difficulties with convergence. Thus, the staggered solution method was used instead. The staggered solution method was used both in the study by Mandal et al. [24] and the study by Molnár and Gravouil [28]. Δu in the size of 10^{-4} was used by Molnár and Gravouil [28]. For this thesis, the step size is $\Delta u = 2 \cdot 10^{-4}$ mm.

The simulations of the two models have not been completed, they were

aborted when the crack started to grow on the upper side of the middle hole. At this time point, the applied displacement was $u \approx 1.2$ mm. The reason for aborting the simulations is that the experimental results from the study by Ingraffea and Grigoriu [17] only propagates so far (Fig. 27c).

The crack paths up to the second hole are similar (Fig. 27a-b). The pattern that can be seen is that the crack is wider and slightly more smeared for the model with a larger length scale parameter (Fig. 27a). This is expected since the length scale parameter ℓ_c decides the width of the crack. The resulting crack paths are not consistent with the experimental crack path (Fig. 27c). The crack, in the experimental result, is first attracted by the first hole but then deflects from it. Then it propagates and penetrates the second hole instead. The crack paths in Fig. 27a-b are affected by holes. They are attracted by the first hole, however instead of deflecting from it, the cracks penetrate it. Then the cracks continue to propagate on the other side of the first hole, and are then attracted by the second hole and eventually penetrate it as well.

For comparison, the benchmark simulated by Mandal et al. [24] is presented in Fig. 28. The crack path from the experimental findings (Fig. 27c) was captured, however the geometry used was altered.

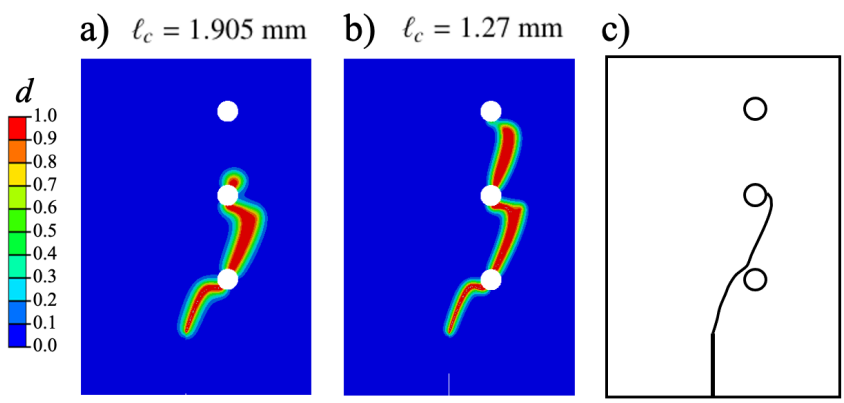

Figure 27: The resulting phase field d for the perforated asymmetric bending test using AT1 as the crack density function. The length scale parameter is a) $\ell_c = 1.905$ mm and b) $\ell_c = 1.27$ mm. The displacement applied to the model is $u = 2$ mm. and the step size is $\Delta u = 2 \cdot 10^{-4}$ mm with the staggered solution scheme. c) Experimental result from the study by Ingraffea and Grigoriu [17]. Drawn based on figure in [17].

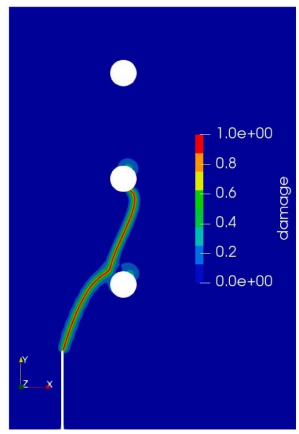

Figure 28: The results presented in the study by Mandal et al. [24] for an altered geometry. The distance from the center of the geometry to the geometrically introduced crack is increased with 0.15 inches (=3.81 mm). The crack density function used is AT2, with the mesh size $h = 0.127$ mm and the length scale parameter $\ell_c = 1.27$ mm. The damage is scaled from 0 (blue) to 1 (red), where the blue represents intact material and the red presents broken material. Figure is from [24] and reprinted with permission from Elsevier.

7.2 Models of Cortical Bone

7.2.1 Sensitivity Analysis of Mesh and Step Size

The Sensitivity Analysis of Step Size

The results of the sensitivity analysis of the step size show that the step size have a significant effect on force-displacement curves, but a smaller effect on the crack paths (Fig. 29). The force-displacement curves for the staggered solution scheme differ to a large extent for the different step sizes (Fig. 29a). The step size also influences the results for the monolithic solution scheme, but not to the same extent. The curves of the monolithic solution schemes display a more brittle behaviour with distinct fracture points. The maximum force for the two step sizes of the monolithic scheme is the same, and the models ruptures at the same displacement. The model with the biggest step size $\Delta u = 2 \cdot 10^{-5}$ mm for the staggered scheme does not fracture all the way, and the fracture points are not clear in the force-displacement curve. The crack path with $\Delta u = 2 \cdot 10^{-7}$ mm does not propagate all the way either, probably because the increment of displacement is very small. However, the

force-displacement curve of the latter does coincide better with the monolithic curves. The staggered solution using $\Delta u = 2 \cdot 10^{-6}$ mm does capture the same pattern as the monolithic curves, but the fracture points are not as distinct.

When focusing on the crack propagation to the first osteon, the crack paths of the staggered solutions in Fig. 29b-d are almost identical. The crack penetrates the osteons and does not propagate in the cement lines. The cement lines do however influence the crack path to a small extent as the crack bends slightly when advancing through the cement line. The crack path in Fig. 29e with the monolithic scheme, also penetrates the osteon but not to the same extent. The crack propagates a little bit further in the cement lines before penetrating the osteon. For the monolithic solution with a smaller step size, in Fig. 29f, the crack does not penetrate the osteon, it only propagates within the cement line. For the models where the crack advanced all the way, the paths through the rest of the geometry are very similar. The only difference is the width of the crack, where the smeared effect of the staggered solution can be seen in Fig. 29c.

The computational time must also be mentioned. The computational cost of the staggered method is greater than that of the monolithic method. The staggered solutions ran for 5 hours, 1.5 days and 9 days, for the decreasing step sizes ($\Delta u = 2 \cdot 10^{-5}$, $\Delta u = 2 \cdot 10^{-6}$ and $\Delta u = 2 \cdot 10^{-7}$ mm), respectively. The monolithic solutions ran for 1 day and 3 days, for $\Delta u = 2 \cdot 10^{-4}$ and $\Delta u = 1 \cdot 10^{-5}$ mm, respectively.

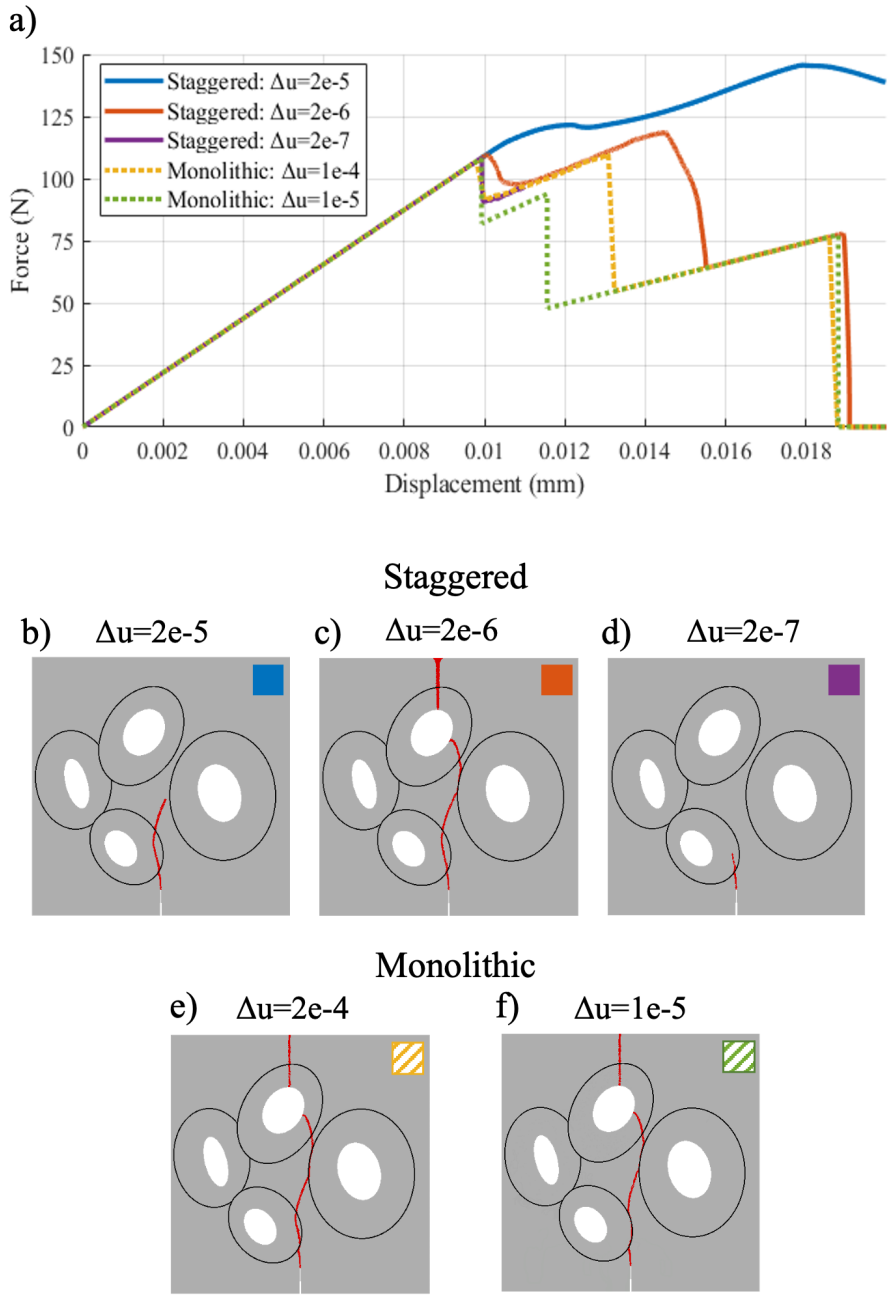

Figure 29: The sensitivity analysis of the step size Δu. a) The force-displacement curves corresponding to the crack paths in b)-f). b)-d) uses the staggered solution scheme with $\Delta u = 2 \cdot 10^{-5}$ mm, $\Delta u = 2 \cdot 10^{-6}$ mm and $\Delta u = 2 \cdot 10^{-7}$ mm, respectively. e)-f) uses the monolithic solution scheme with $\Delta u = 2 \cdot 10^{-4}$ and $\Delta u = 1 \cdot 10^{-5}$ mm, respectively. The mesh size is $h = 2.5$ µm. The crack is represented by $d > 0.9$.

The Sensitivity Analysis of Mesh

The results of the sensitivity analysis of the mesh can be seen in Fig. 30. The step sizes used are based on the discussion and conclusions drawn from the sensitivity analysis of the step size, which is $\Delta u = 2 \cdot 10^{-4}$ mm for the monolithic solution scheme and $\Delta u = 2 \cdot 10^{-6}$ mm for the staggered solution scheme.

The cracks paths of both the monolithic and staggered solution are almost identical when focusing on the crack propagation to the first osteon (Fig. 30). The force-displacement curves of the three mesh sizes for the monolithic solution are identical (Fig. 30a). The fracture points are distinct and are the same for the three values of h. The fracture points for the staggered solutions are not as distinct (Fig. 30b). The mesh size of $h = 1.67$ µm produces a curve which is the most similar to the monolithic force-displacement curves. However, all three mesh sizes produces force-displacement curves with the similar pattern as the monolithic curves.

There is also an effect of the mesh sizes on the width of the crack. The coarser mesh (greater value of h) gives wider cracks. The staggered solution in Fig. 30f-h also has wider cracks, which is the smeared effect mentioned earlier.

The mesh size does also affect the computation time as the number of elements increased with decreasing value of h. The number of elements used to discretize the model for each mesh size h is presented in Table 7. The number of elements are doubled for each increase in h, and the same applies for the computational time.

Table 7: The number of elements used when discretizing the models using the three mesh sizes h for the sensitivity analysis of the mesh.

Mesh Size h (µm)	**Number of elements**
2.5	≈ 172 000
1.67	≈ 354 000
1.25	≈ 609 000

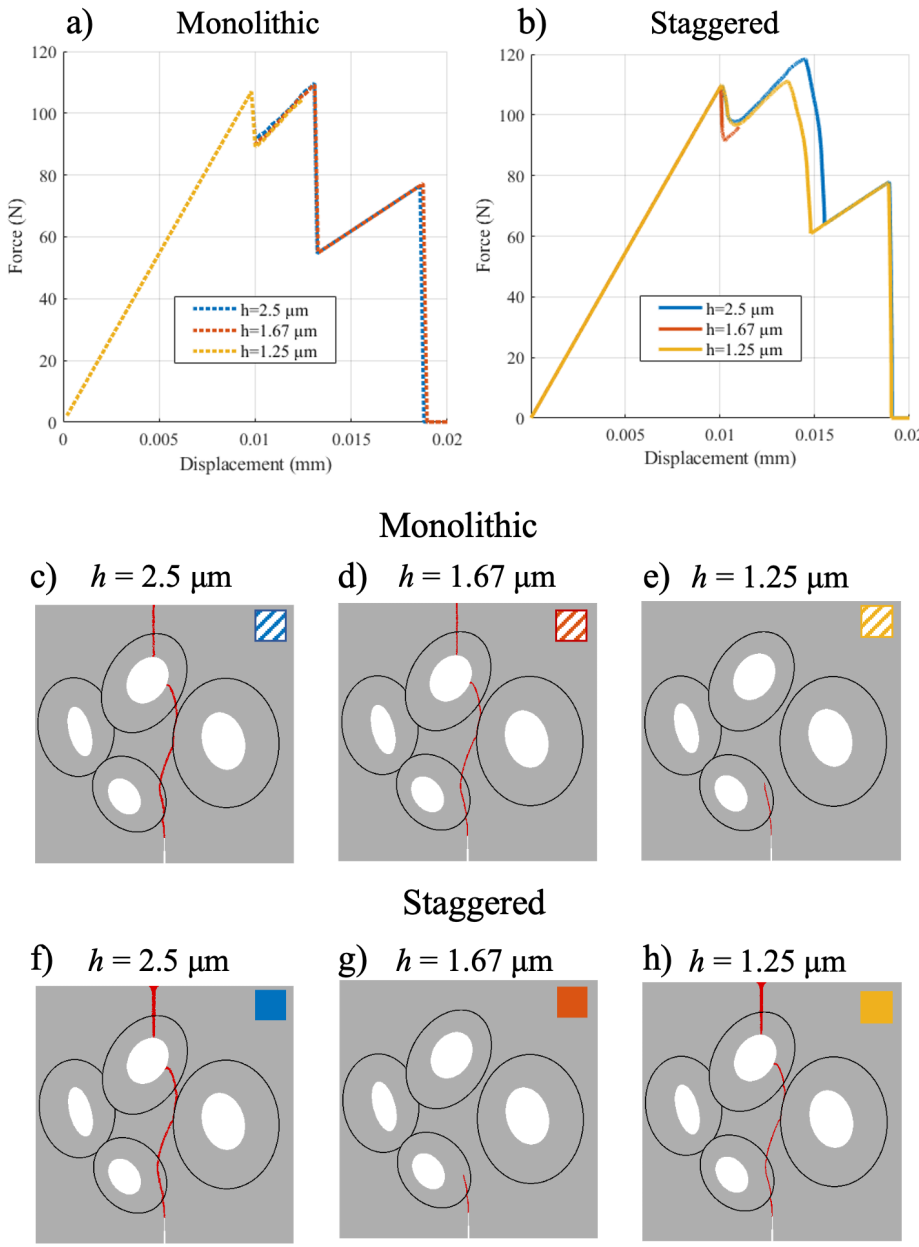

Figure 30: The sensitivity analysis of the mesh size h. a) The force-displacement curves corresponding to the crack paths c)-e). b) The force-displacement curves corresponding to the crack paths f)-h). c)-e) The monolithic solution with $\Delta u = 2 \cdot 10^{-4}$ for the mesh size $h = 2.5$ μm, $h = 1.67$ μm and $h = 1.25$ μm, respectively. f)-h) The staggered solution with $\Delta u = 2 \cdot 10^{-6}$ mm for $h = 2.5$ μm, $h = 1.67$ μm and $h = 1.25$ μm, respectively. The crack is represented by $d > 0.9$.

7.2.2 Analysis of the Material Parameters

The analysis shows that the crack paths are affected by the material parameters used to some extent, as can be seen in Fig. 31. The models are simulated using three sets of material parameters. Set 1 is the standard material parameters presented in Table 4. For Set 2, $\mathcal{G}_c$ for the osteons are set to the value used for the matrix. Set 3 is a homogeneous set of material parameters. Since, both Model A and B are used in this analysis, Fig. 31 also displays that the geometry also affects the crack paths. The difference between Model A and Model B, is that Model B is rotated 180°. The monolithic solution scheme with $\Delta u = 2 \cdot 10^{-4}$ mm was used in Fig. 31b-d and 31f, and the staggered solution scheme with $\Delta u = 2 \cdot 10^{-6}$ mm was used in Fig. 31a and 31e.

For Model A, the crack paths for Set 1 (Fig. 31a), Set 2 (Fig. 31c) and Set 3 (Fig. 31e) are very similar. However, when focusing on the osteon in the top of the model, the crack propagates slightly different. For Set 1, i.e. the standard material parameters, the crack propagates longer in the cement lines than for Set 2. It is deflected more for Set 1. The crack for Set 3 (Fig. 31e), the homogeneous material, is not affected by the cement lines. It is only affected by the Haversian canals.

For Model B, the different sets of material parameters affects the crack path to a greater extent than for Model A. In Fig. 31b, using the standard material parameters (Set 1), the crack is deflected and follows the cement line of the first osteon. The cement lines also slightly bends the crack path when penetrating the upper osteon. For Set 2 and 3, in Fig. 31d and 31f, the first osteon is instead penetrated. The crack paths for Set 2 and 3 are similar.

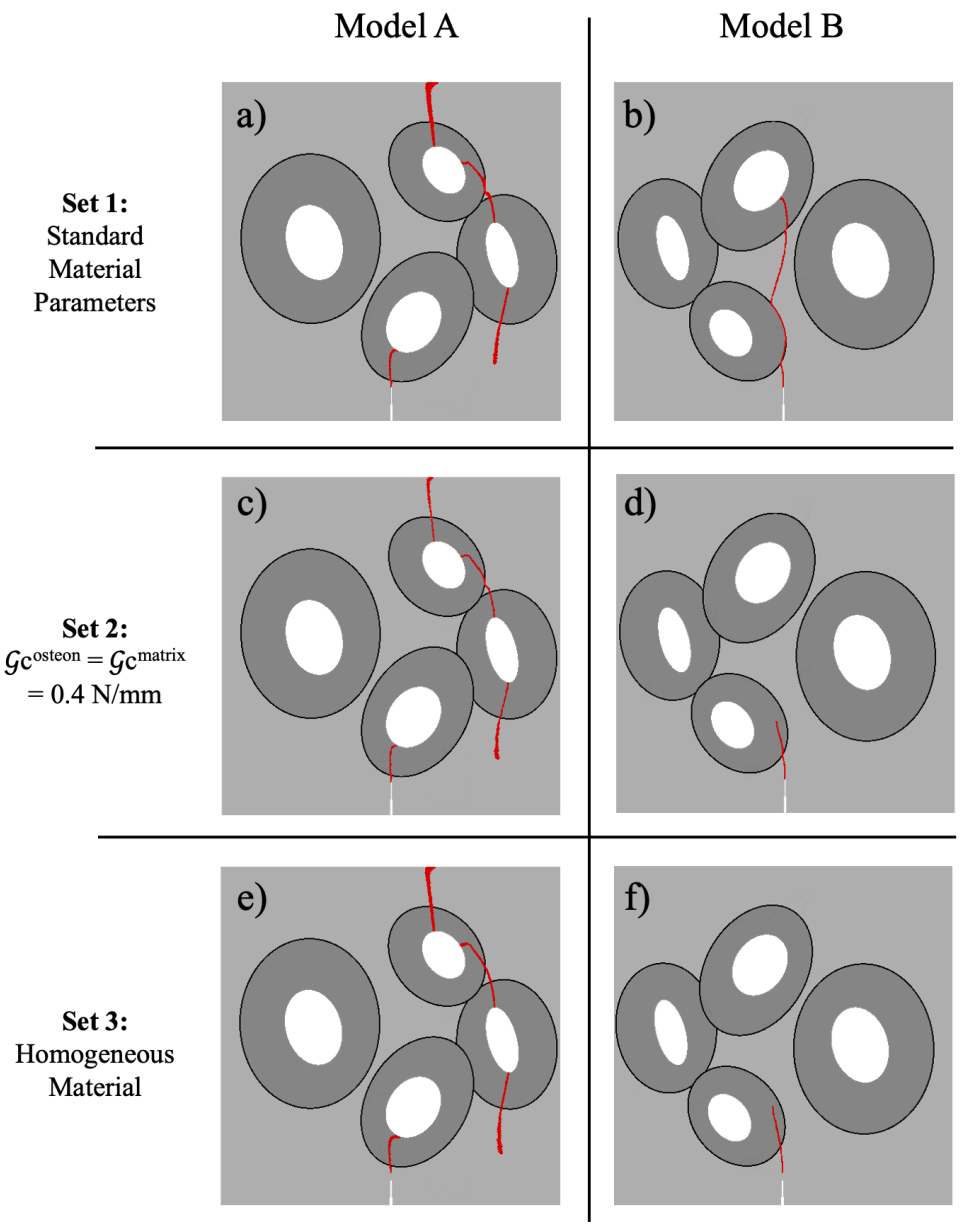

Figure 31: a)-b) Set 1: The standard material parameters as presented in Table 4. c)-d) Set 2: G_c for the osteons and the matrix are set to be equal, i.e. $G_c = 0.4$ N/mm. e-f) Set 3: All material parameters are set to be equal the material parameters for the matrix, i.e homogeneous material. Model A is represented in a), c) and e) and Model B is represented in b), d) and f). The monolithic solution scheme with $\Delta u = 2 \cdot 10^{-4}$ mm was used in b)-d) and f), and the staggered solution scheme with $\Delta u = 2 \cdot 10^{-6}$ mm was used in a) and e). The crack is represented by $d > 0.9$.

7.2.3 The Effect of Geometry

The results shows that the porosity has an effect on the crack propagation, both when a geometrical crack is introduced and not. The results are presented in Fig. 32 for the models with a geometrically introduced crack, and in Fig. 33 it is excluded. In Fig. 32a-b and 33a-b, the staggered solution scheme with $\Delta u = 2 \cdot 10^{-6}$ mm was used. The monolithic solution scheme with $\Delta u = 2 \cdot 10^{-4}$ mm was used for Fig. 32c and 33c.

The crack path in the model without Haversian canals (Fig. 32a) is a straight crack, and it penetrates from the geometrically introduced crack and through the first osteon. It also propagates in the cement line of the upper osteon. It is different from the crack path in Fig. 32b, where the Haversian canals, i.e. the holes, affect the crack propagation, as seen also in the perforated asymmetric bending test. The crack in Fig. 32b propagates through the first osteon, then the crack is initiated in the Haversian canal of the osteon to the right in the model and propagates towards the Haversian canal of the upper osteon. When the crack has reached the canal, the crack continues to grow from both the upper and the right canal simultaneously. The effect of the cement lines can be seen as the crack is deflected when propagating from the right osteon to the upper osteon.

As the porosity is increased, as for the model with 15% porosity in Fig. 32c, the distance between the Haversian canals decreases. The distance between the right and upper canal is short. The distance from the geometrically introduced crack and the first canal is also short. It is here the cracks are propagating, which is an expected mechanical response. Though, an effect of the cement lines can be seen, when advancing from the right to upper osteon. The effect is however smaller than for the crack in the model with 7% porosity in Fig. 32b.

The difference due to the porosities can also be seen in the force-displacement curves (Fig. 32d). The curve of the model with 0% porosity is straight and only has one fracture point. The curves of 7% and 15% have two fracture points that are captured in Fig. 32d. The displacement applied when the fracture points occur are included in Table 9. The first fracture points are similar for the all the porosities, but differs more for 15% porosity. The second fracture points differs with 1.5 µm. The maximum force decreases as the porosity increases, as can be seen in Table 8.

The results for the models without a geometrically introduced crack are also affected by the difference in porosity and are presented in Fig. 33. The model with 15% porosity, in Fig. 33c, fractures at the same place as the model with a geometrically introduced crack (Fig. 32c). Although, in Fig. 33c the crack is initiated in the right Haversian canal. There is a small effect of the cement lines in this model as well. The effect is greater in the model with 7% porosity in Fig. 33b. The crack is initiated in the right osteon in the model, but as it propagates to the upper osteon it is deflected into the cement line.

For the model with 0% porosity and without a geometrical crack introduced (Fig. 33a), no crack is initiated. Therefore, the force-displacement curve (Fig. 33d) has no fracture point. This implies that the displacement applied is not enough for a crack to be formed. In Table 8, the maximum force for the model is bigger than 308.2 N, as the specific number is not known.

Table 8 and the force-displacement curve (Fig. 33d) show that the maximum force applied decreases with increasing porosity. The fracture point of the model with 15% porosity in terms of displacement applied is lower than of the model with 7% porosity (Table 9). The first fracture points of the models without an introduced crack coincide with the second fracture points for the models with an introduced crack. The maximum force is also higher for the models without introduced cracks (Table 8).

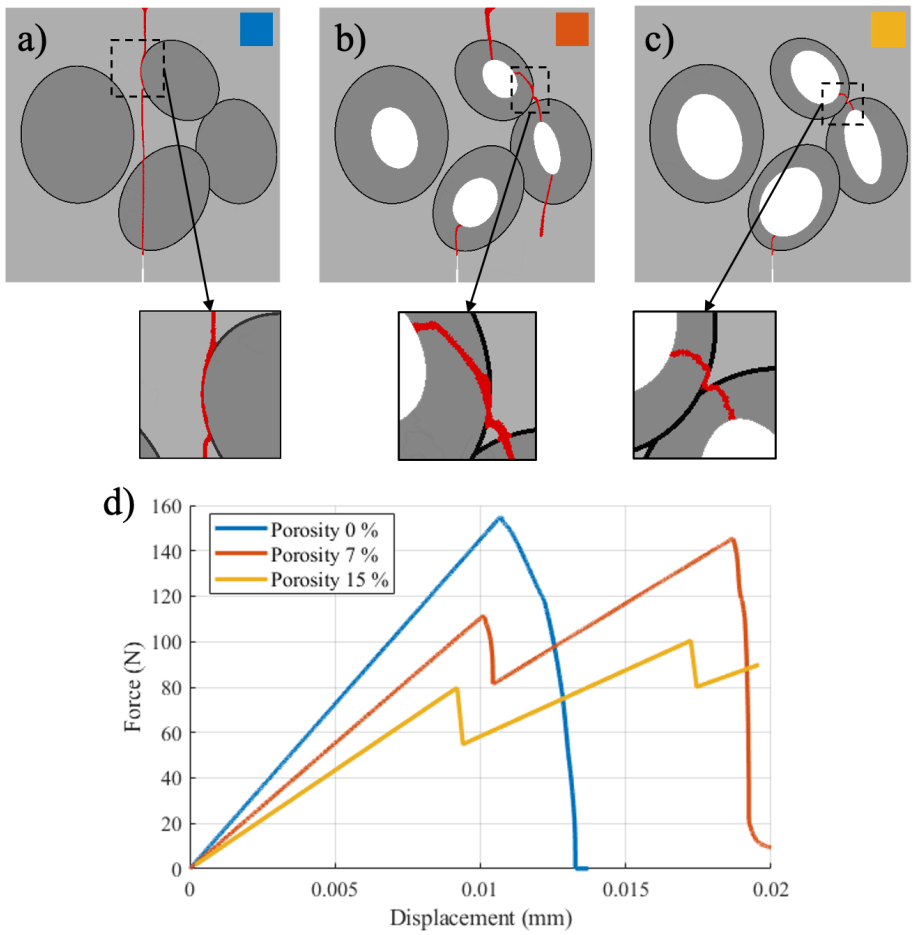

Figure 32: The influence of porosity. Models with a), 0% b) 7%, c) 15% porosity was evaluated. d) The corresponding force-displacement curves. a)-b) The staggered solution scheme with $\Delta u = 2 \cdot 10^{-6}$ mm was used. c) The monolithic solution scheme with $\Delta u = 2 \cdot 10^{-4}$ mm was used. The crack is represented by $d > 0.9$. The stress and strain plots for these models can be found in Appendix B.

Table 8: The maximum force applied to the models with 0%, 7% and 15% porosity. Both the models with geometrically introduced crack and without are represented.

	Maximum Force (N)	
Porosity (%)	With Geometrically Introduced Crack	Without Geometrically Introduced Crack
0	154.8	>302.8
7	145.3	227.6
15	100.4	167.9

Table 9: The first and second fracture points, i.e. the displacement applied to the models when the first and second fracture points occur. Models with and without a geometrically introduced crack and 0%, 7% and 15% porosity are represented.

Fracture Points			
	Porosity (%)	First Fracture Point (µm)	Second Fracture Point (µm)
With Geometrically Introduced Crack	0	10.7	-
	7	10.1	18.7
	15	9.2	17.2
Without Geometrically Introduced Crack	0	-	-
	7	19.6	-
	15	18.1	-

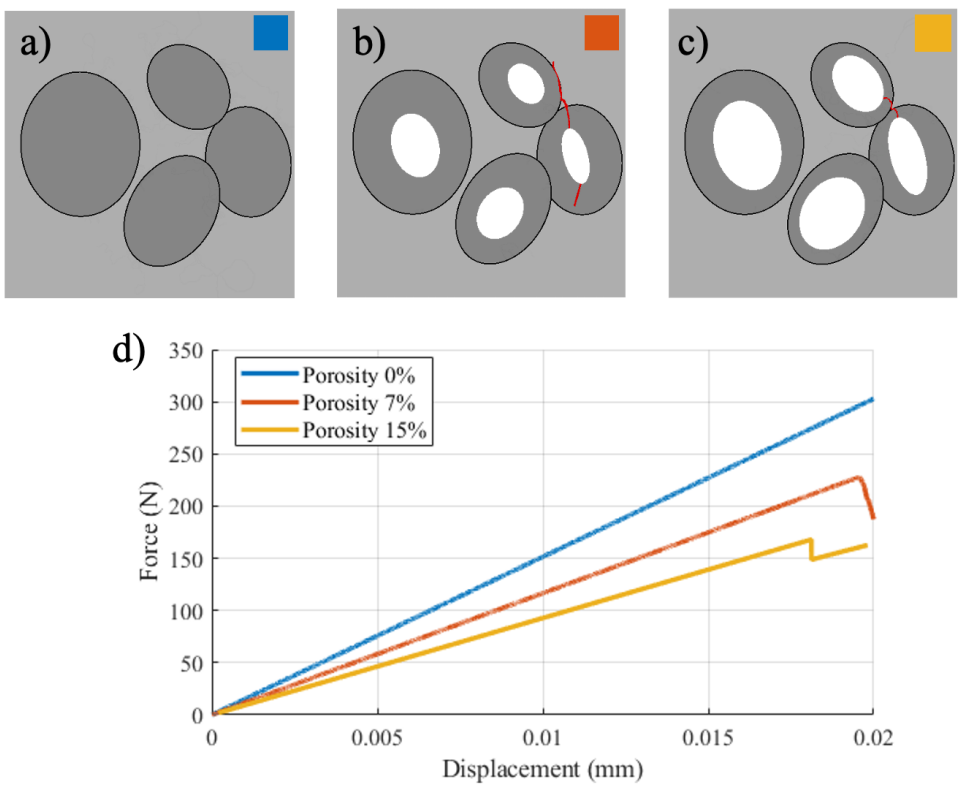

Figure 33: The effect of porosity, while also excluding a geometrically introduced crack. Models with a), 0% b) 7%, c) 15% porosity was evaluated. d) The corresponding force-displacement curves. a)-b) The staggered solution scheme with $\Delta u = 2 \cdot 10^{-6}$ mm was used. c) The monolithic solution scheme with $\Delta u = 2 \cdot 10^{-4}$ mm was used. The crack is represented by $d > 0.9$. The stress and strain plots for these models can be found in Appendix B.

8 Discussion

The aim of this thesis is to investigate the feasibility to model crack propagation in cortical bone using the PF method. The implemented PF framework is first tested on typical benchmarks from commonly used in literature and it is then used on cortical bone models. For the cortical bone models, a sensitivity analysis of the mesh and step size is first performed which will conclude which mesh and step size to use for the rest of the analysis. The crack propagation in the cortical bone models is simulated with different material parameters, geometries and levels of porosity.

8.1 Benchmarks

The benchmark tests show that the implemented PF framework successfully captures the crack paths presented in the literature. They give insight in how the resulting crack paths are affected by the choice of crack density function. The solution methods used also affect the modelled crack. The asymmetric perforated bending test provides insights in how holes in the geometry affects the crack propagation.

8.1.1 SENT Tensile

The implemented PF framework successfully models the crack paths under a tensile load. The crack paths for the crack density function AT2 (Fig. 23c-d) are corresponding well to the results presented by Kristensen and Martínez-Pañeda [20] and by Molnár and Gravouil [28] (Fig. 24). Kristensen and Martínez-Pañeda [20] uses AT2 and a monolithic solution scheme with a quasi-Newton method. They also use an adaptive step scheme. It should not be a surprise since the framework for the monolithic solution method used in thesis is based on the same open source code [20]. The smeared effect in the beginning of the crack path, as seen in Fig. 23c, is captured in the result by Kristensen and Martínez-Pañeda [20] as well (Fig. 24a). The crack path for the staggered solution (Fig. 23d) is similar but wider than the crack path presented by Molnár and Gravouil [28] which also uses a staggered solution scheme (Fig. 24b). This is however expected since the length scale parameter

ℓ_c is 0.0075 mm [28], and therefore 3 times smaller than the ℓ_c used in this thesis.

The force-displacement curves when using AT2 as the crack density functions (Fig. 23e), are also consistent with the study by Kristensen and Martínez-Pañeda [20]. The non-linear behaviour in the curve is also included in the force-displacement curve in Fig. 24c [20]. The point of fracture (at $u \approx 0.006$ mm) and the maximum force (650 – 700 N) is also consistent.

The difference between AT1 and AT2 can clearly be seen in Fig. 23e. The curves for AT2 deviates and behave more non-linear, compared to the linear curves for AT1. This is the effect of the initial elastic domain of the crack density function AT1. Without an initial elastic domain, the damage start as soon as the load is applied, i.e. the response when using AT2. The force-displacement curve when using AT1 results in a higher maximum force ($>$ 700 N) and the fracture point is sharper. This brittle response is expected in bone tissue. This concludes that AT1 will most likely be a good choice for the cortical bone models [33].

8.1.2 SENT Shear

The cracks when using the crack density function AT1 (Fig. 25a-b) have propagated along the expected crack path. The crack paths have the same direction and approximately the same angle. The results corresponds well to the results presented in the literature [20, 25] (Fig. 26). Mandal et al. [24] uses the staggered solution scheme with both AT1 and AT2. Kristensen and Martínez-Pañeda [20] uses the monolithic solution scheme with a quasi-Newton method for the crack density function AT2.

The force-displacement curves for AT1 in Fig. 25e do have a similar pattern to the curves presented in Fig. 26d. The small difference can be due to that Kristensen and Martínez-Pañeda [20] uses AT2 instead of AT1. The force-displacement curves for AT2 also presented in Fig. 25e corresponds better, as could be expected. The curves for AT2 have the same non-linear behaviour in the initial phase. The maximum force ($\approx$ 325 N) for AT1 is closer to the results presented by Kristensen and Martínez-Pañeda [20] than the maximum force for AT2 ($>$ 350 N). The fracture points also coincides better for AT2.

However, the crack paths using AT1 (Fig. 25a-b) are more similar to the expected crack path than using AT2 (Fig. 25c-d). The expected crack path is based on the results presented in Fig. 26. Kristensen and Martínez-Pañeda [20] uses AT2, and the crack paths presented have the same straighter path as seen in the results for AT1 in this thesis (compare Fig. 26c to Fig. 25a-b). The curved crack paths when using AT2 (Fig. 25c-d), have not been captured by the results from the literature in Fig. 26.

The smeared effect of the crack path is seen when using AT2 compared to AT1. It can be seen both for the SENT Shear model and the SENT Tensile model. This behaviour is also captured in the results presented by Mandal et al. [24] in Fig. 26a-b, which uses both AT1 and AT2. For the two SENT models, there is also a smeared effect when using the staggered scheme compared to the monolithic scheme. However, for the SENT Shear model, it is mostly seen at the end of the crack path in the lower corner in Fig. 25b and 25d, whereas for the SENT Tensile model, the smeared effect can be seen along the full length of the crack.

The results from this benchmark show that the framework implemented successfully can model the crack path for a shear load. The results also show that even if the force-displacement curves for AT2 are more consistent with results in literature, the crack paths for AT1 is a better match. The elastic domain of AT1 creates the more brittle behaviour in the force-displacement curves, which is sought for the cortical bone models.

8.1.3 Perforated Asymmetric Bending Test

The resulting crack paths in Fig. 27a-b for the perforated asymmetric bending test are not consistent with the crack path found experimentally [17], as can be seen in Fig. 27e. However, the crack paths are influenced by the perforations, which is the effect that this thesis wants to investigate when choosing this benchmark test. The results clearly show that the holes in the geometry affect the crack path.

Mandal et al. [24] were not able to capture the experimental crack path in [17] (Fig. 27e), with the same geometry as used in this thesis. However, with an altered geometry, they captured the experimental crack path (Fig. 28). They found that it is difficult to capture the correct crack path with the

dimensions used in the geometry in Fig. 18 [24]. By adjusting the position of geometrically introduced crack with 0.15 inches (= 3.81 mm), they were able to capture the experimental crack path from [17] using the crack density function AT2 [24]. Molnár and Gravouil [28] also tried to simulate the experimental crack path from [17] but were not able to do so. They presented a crack path similar to the ones presented in this thesis, but the geometry was different.

Since Mandal et al. [24] claims that it is difficult to model the exact crack path using the correct geometry, the benchmark test in this thesis can be considered relatively successful. The importance of this test is to evaluate if the holes affect the crack propagation when using the implemented PF framework, and they do.

8.2 Models of Cortical Bone

8.2.1 Sensitivity Analysis of Mesh and Step Size

The Sensitivity Analysis of Step Size

The crack paths when using the monolithic solution scheme differ for the two step sizes (Fig. 29e-f). The crack path when using the smaller step size deflects into the cement line when approaching the first osteon (Fig. 29f). When using a bigger step size (Fig. 29e), the crack instead penetrates the first osteon. After the first the osteon, the crack paths for both step sizes continues to propagate in the same manner (Fig. 29e-f). The corresponding force-displacement curves in Fig. 29a also behaves similarly. The models exhibit brittle behaviour, as expected for cortical bone. The maximum force for the two step sizes are the same. There is also a difference in computational time for the two step sizes. The advantage of the monolithic solution scheme is that the correct crack paths can be modelled with a greater step size, which saves computational time. Therefore, $\Delta u = 2 \cdot 10^{-4}$ is the step size used for the monolithic solutions.

In the case that the monolithic solution scheme has problems with convergence, the staggered solution scheme is used instead. The staggered solution is more robust though known to be sensitive to step size [28]. It requires a

small step size which makes it computationally demanding. The step size affects the force-displacement curves in Fig. 29a, whereas the crack paths (Fig. 29b-d) are almost identical when observing the propagation to the first osteon. As the step size is decreased, the force-displacement curve becomes more similar to the monolithic curves. This step size dependency is in concordance with the conclusion drawn in the study by Kristensen and Martínez-Pañeda [20], and can be seen in Fig. 24c for the SENT Tensile model. The force-displacement curve for smallest step size coincides with one of the monolithic curves (Fig. 29a), however the model does not fracture all the way. There is also a difference in computational time between the step sizes $\Delta u = 2 \cdot 10^{-7}$ mm and $\Delta u = 2 \cdot 10^{-6}$ mm and the difference is measured in days. The force displacement curve of the step size $\Delta u = 2 \cdot 10^{-6}$ mm follow the same pattern as the monolithic curves and the first and last fracture points coincide with the monolithic solutions. The step size $\Delta u = 2 \cdot 10^{-6}$ mm is therefore a good choice as it also saves computational time. Since the crack paths of the staggered solution in Fig. 29b-d are nearly identical, the model using step size $\Delta u = 2 \cdot 10^{-6}$ mm is considered converged. Therefore, $\Delta u = 2 \cdot 10^{-6}$ is the step size used for the staggered solutions.

The Sensitivity Analysis of Mesh

The mesh size that is used for the cortical bone models is $h = 1.67$ µm, which discretizes the cement lines with three elements and it fulfills the criteria related to the length scale parameter ℓ_c. This conclusion is firstly based on that all crack paths in Fig. 30 are nearly identical, when focusing on the propagation to the first osteon. Secondly, the force-displacement curves for the monolithic solutions in Fig. 30a coincide. The force-displacement curve for $h = 1.67$µm for the staggered scheme (Fig. 30b) is the curve that is most similar to the monolithic curves. Lastly, to fulfill the criteria $h < \ell_c/2$ and also save computational time, $h = 1.67$ µm is a reasonable choice.

8.2.2 Analysis of the Material Parameters

The material parameters used when modelling human cortical bone can affect the resulting crack paths. Changing the material parameters affect both Model A and B, but the effect is more clear for Model B (Fig. 31b, 31d, 31e). When the critical energy release rate $\mathcal{G}_c$ for the osteons is higher than for the matrix, which was experimentally determined by Mullins et al. [30],

the crack is deflected and propagates in the cement line (Fig. 31b). When $\mathcal{G}_c^{\text{osteon}} = \mathcal{G}_c^{\text{matrix}}$, as in Fig. 31d, the crack instead penetrates the osteon. This corresponds to the results found in the study by Mischinski and Ural [27], which used the cohesive elements method. The osteons are protected from damage by a higher value of the critical energy release rate $\mathcal{G}_c$.

The difference in the resulting crack paths between Model A and B can be explained by the difference in geometry. In Model A, the crack approaches the cement line of the first osteon at approximately 90° and the crack penetrates the cement line (Fig. 31a). The crack in Model B approaches the cement line with a smaller angle and it is deflected (Fig. 31b). The results suggests that when approaching the cement lines with a smaller angle, the crack deflects into the cement lines. In the PF method, the critical release energy $\mathcal{G}_c$ is the driving force for crack propagation. For the crack to be able to advance, the energy released must be equal to or greater than the energy required for fracture, i.e. $\mathcal{G} = \mathcal{G}_c$. The crack will propagate where it requires the least amount of energy to advance. When the angle is small, the cement lines provides a weaker path with a lower value for $\mathcal{G}_c$. Hence, the cement lines is the preferred crack path as the critical limit for the released energy to reach is lower. As seen in the SENT Tensile model, the crack wants to propagate perpendicular to the tensile load applied. When the angle is approximately 90° to the cement lines, the crack must turn and propagate parallel to the load applied in order to propagate in the cement lines. This requires more energy than penetrating the cement line and propagating to the canal, which is a crack path perpendicular to the load applied. Therefore, when the angle is bigger, the preferred crack path is to propagate through the cement lines towards the canal.

For an insight of the effect of $\mathcal{G}_c$ for the cement lines, Model B can be used. The crack path in Fig. 30b can be compared to Fig. 31b. The same material parameters are used except $\mathcal{G}_c$ for the cement lines. In Fig. 30b $\mathcal{G}_c = 0.17$ N/mm and the crack penetrates the first osteon. With $\mathcal{G}_c = 0.13$ N/mm in Fig. 31b, the crack is deflected into the cement line when approaching the first osteon. Since the same geometry is used, the angle in which the crack approaches the cement line is the same. The higher value of $\mathcal{G}_c$ for the osteons compared to the matrix is also the same for the two models. This suggests that the osteons are protected from damage when a higher value of $\mathcal{G}_c$ for the osteons is combined with a lower value of $\mathcal{G}_c$ for the cement lines compared to the matrix. Experiments by Koester et al. [19] and Chan

et al. [7] show that the cement lines play an important role in deflecting cracks. By modelling the cement lines with different material parameters, it can give an insight in how the bone tissue is designed to stop, slow and redirect propagating cracks, which is one of the toughening mechanisms in the tissue. It is not only the values that are important to investigate, but the ratios (the ratio between matrix, osteons and cement lines) used are also key.

Model A is based on one of the XFEM-models used in the study by Gustafsson et al. [15]. The crack for Model A propagates differently compared to the XFEM-model, seen in Fig. 9A. The crack path in the XFEM-model was more straight, penetrated the first osteon and deflected into the cement lines in the upper osteon. In Model A (Fig. 31a and 31c), the crack penetrates the first osteon and then a second crack is initiated in the Haversian canal of the right osteon. The XFEM-method implemented in *Abaqus* and used by Gustafsson et al. [15], only allows one active crack. The PF method can simulate multiple crack paths, which could explain the difference in the resulting crack paths as another crack is allowed to be initiated in Model A. In the XFEM-model only one crack was propagating and another crack could not be initiated. Another important difference between the two methods are the criteria for crack advancement. In the PF method, it is the fracture criterion based on the critical energy release rate $\mathcal{G}_c$. In XFEM, the criteria is based on the maximum principle strain. In the study by Gustafsson et al. [15], the same value for $\mathcal{G}_c$ was used for the matrix, osteon and cement lines, i.e. $\mathcal{G}_c = 0.4$ N/mm. In the PF method, $\mathcal{G}_c$ is important to model crack growth, this thesis uses different values of $\mathcal{G}_c$ for the matrix, osteon and cement lines. The different values of $\mathcal{G}_c$ clearly has an effect on the crack paths as seen when comparing Set 1 and Set 2 for both Model A and B in Fig. 31.

When adopting the homogeneous set of material parameters (Set 3), the weak interface of the cement lines is not present. The only part of the microstructure that is included is the Haversian canals. In Model A (Fig. 31e), the crack path is only affected by the canals. The crack first propagates from the tip of the geometrically introduced crack to the first osteon. A new crack is then initiated in the right canal. The canals attract the crack and this influence of the holes is expected, as it is seen in the perforated asymmetric bending test as well as in two studies by Gustafsson et al. [14, 15], where the Haversian canals attracted and affected the crack propagation. This gives additional insights into the importance of the microstructure, as it provides the tissue

with an interface in which crack paths are affected in order to dissipate energy. By dissipating energy, the tissue protects itself from fracture.

8.2.3 The Effect of Geometry

The crack propagation is affected by the geometry of the cortical models, both due to porosity and if a geometrical crack is introduced (Fig. 32 and 33). The crack path of the model with 0% porosity and an introduced crack (Fig. 32a) shows that the Haversian canals do affect the crack path, especially compared to the models with 7% and 15% porosity (Fig. 32b-c) as 0% porosity results in a straight crack. The model also show some effect of the cement lines, as it propagates along the cement line of the upper osteon (Fig. 32a).

The increase in porosity also affects the crack paths. The model with 15% porosity in Fig. 32c breaks at weak regions and the cement lines only influence the crack path to a small extent. The cracks in the model with 7% porosity in Fig. 32b are more influenced by the cement lines, even if the difference is still small. As the porosity increases with age, it can be said that the effect of cement lines is decreased with age, which agrees with both experimental and numerical findings in literature [7, 23]. The Haversian canals attract the propagating cracks and the cement lines stop or redirect the cracks. In healthy young bone, this protects the osteons from being penetrated. In older bone, the porosity is increased and the holes are bigger, which increases the ability to attract the cracks. The relationship between the canals and the cement lines have changed, which affects the cement lines' ability to stop or deflect the cracks. This behaviour is captured in the sketch in Fig. 4, which shows that the cracks are more deflected and affected by the cement lines in the younger bone compared to the older bone. The sketch is based on experimental findings in the study by Chan et al. [7].

The porosity of the models also affects the initiation and crack propagation when a geometrically crack is not introduced in the model, as seen in Fig. 33. The cracks are initiated in the Haversian canals, instead from the tip of the introduced crack as in Fig. 32. The maximum force experienced in the models are also affected by porosity. A higher degree of porosity makes the models weaker and break under a lower force than a model with a lower degree of porosity (Table 8). The same behaviour is seen for both models with and without a geometrically introduced crack. Although, the maximum

force for the models without a geometrically introduced crack is greater. It requires more load to initiate a new crack than to continue to propagate from an already existing crack tip. For the model with 0% porosity (Fig. 33a), the load applied is not enough as no crack is initiated.

The effect of the cement lines can also be seen when comparing Fig. 33b and 33c. The cement lines in the model with 7% porosity are more effective in deflecting the crack and protecting the osteon than the model with 15% porosity, which further suggests that the effect of the cement lines decreases with increasing porosity and age as seen experimentally by Chan et al. [7]. However, it is not beneficial for the structure of the bone tissue if cracks are initiated in the canals. The models used in this thesis are simplified, and there is no microdamage and microcracks included which is more likely the source of crack initiation in real cortical bone. As the bone remodelling process is impaired with age, the microdamage accumulates and becomes a possible source for crack initiation.

In the XFEM-study by Gustafsson et al. [15], the effect of ageing was investigated by analysing the effect of increasing porosity (Fig. 8). The models used in the analysis include eight osteons instead of four. When comparing 7% and 15% porosity (Fig. 8C and 8E), the cracks were deflected into the cement lines to a greater extent for 7% porosity. The crack path was straighter and penetrated the osteons for the model with 15% porosity. This behaviour due to increased porosity agrees with the results presented in this thesis. The maximum force applied also decreased when the porosity was increased [15]. However, the actual crack paths and the force-displacement curves differ. The force-displacement curves in Fig. 32d and 33d display brittle behaviour and the XFEM-models failed to capture a brittle behaviour for the models with different porosities. The purely theoretical model of 0% porosity was also modelled by Gustafsson et al. [15]. The crack path for the 8-osteon model with 0% porosity (Fig. 8A) was not as straight as the crack path presented in Fig. 32a. The crack path in the XFEM-model (Fig. 8A) was also propagating in the cement lines to a greater extent. As discussed above, the difference can be explained by the method used, XFEM or PF.

8.3 Limitations and Sources of Error

First of all, the cortical bone models used in this thesis are simplified. The osteons and the interstitial matrix are assumed to be homogeneous, excluding both microdamage and the structure of the lamellae [33]. The cement lines are also assumed to be 5 µm wide all the way around the osteons, which is not the case in real cortical bone [8]. The width actually varies in size. However, a constant width make it easier to ensure that the the cement lines are resolved properly when meshing the models. A finer mesh would probably be needed if the width varies, which results in an increase in computational time.

The geometries of the osteons and the Haversian canals are also simplified by fitted ellipses. In real cortical bone, as seen in Fig. 7, they are not perfect ellipses. The models used in thesis are based on the XFEM-models used in the work by Gustafsson et al. [15]. In the XFEM-method, normal vectors for each element in the cement lines were used in the damage criterion implemented by Gustafsson et al. [15], and was the reason for using ellipses. A further improvement could be to model more realistic shapes of the osteons and canals, since the PF method does not require the normal vectors.

As seen in the benchmarks, the solution scheme used can have an effect on the resulting crack paths and force-displacement curves. The monolithic solution scheme is used in first hand in this thesis, and if problems with convergence occur, the staggered solution scheme is used instead. The solution scheme which is used can therefore differ in the results presented, and can be a source of error.

A disadvantage of the PF method is the problems with convergence of the monolithic scheme. A solution is not always found. The alternative, the staggered scheme, is computational demanding where the simulations in this thesis run for several days and in some cases a week. Problems with numerical instability only occurred sporadically when using XFEM in the work by Gustafsson [13]. Another limitation of the PF method is that the crack initiation is driven by the history field variable $\mathscr{H}^+$ which is dependent on the strain energy density. Physically, cracks are initiated due the stresses and are related to the strength of the material. Among others, Kumar et al. [21] are exploring the option of amending the PF method with an additional crack driving force based on the strength of the material to address this limitation.

Lastly, the crack propagation is modelled in 2D under plane strain conditions. It could be modelled in 3D instead to model even more realistic crack paths. The implementation for 3D in the PF framework is not difficult, however the computational time would increase a great deal and convergence can also be an issue. The models used in this thesis, with the size 1.2x1.2 mm^2, take days to run, even a week in some cases. In the literature, modelling of crack propagation in 3D in the microstructure of cortical bone have not yet been done [14].

8.4 Future Work

To capture realistic crack paths, the geometry used in the models should be even more realistic. In the future, the PF method could be used to model geometries which includes more osteons than the four included in the models in this thesis. By including more osteons, the effect of the microstructure on crack propagation can be further analyzed. Also, the osteons and canals could be segmented and modelled with a more realistic shape than ellipses, as in the study by Maghami et al. [23] (Fig. 10).

The individual mechanical properties of the osteons, cement lines and interstitial matrix and the ratio between them should be further investigated. It could answer questions regarding how the bone tissue is designed to resist fracture. The effect of age on these properties is also important to continue to analyze. By using different material parameters, it can give an insight into the individual properties of the osteons, cement lines and interstitial matrix which are difficult to determine experimentally.

Regarding the PF method, other definitions for the split of the strain energy density can be tested. This thesis uses the volumetric-deviatoric split by Amor et al. [3]. Another common choice is the spectral split by Miehe et al. [26]. It would be interesting to compare the influence of the split used on the crack propagation.

There is a debate going on regarding the length scale parameter ℓ_c [29]. Is it a numerical parameter or is it a material parameter? In this thesis, only one value for ℓ_c is used. It would be interesting to test different values, and also individually different values for the osteons, cement lines and interstitial matrix to see if it could give some answers to if ℓ_c is a numerical or material

parameter.

For the further understanding of crack propagation, a 3D-model would give a better understanding of the crack growth in the microstructure of cortical bone. However, as mentioned in Section 8.3, it is a demanding and difficult task.

9 Conclusions

In this thesis, A PF framework is implemented to be able to model crack propagation in the microstructure of human cortical bone. The cortical bone models, which are based on microscopy images, are modelled with different material parameters, geometries and levels of porosity.

This thesis show that the material parameters used to describe the osteons, cement lines and the interstitial matrix play a role in the crack growth, and are of importance to be able to capture realistic crack paths with deflection into the cement lines. A higher value for the critical energy release rate of the osteons compared to the interstitial matrix protects the osteons from penetration of the crack. It can also be concluded that age affects the crack propagation. The ability to deflect the cracks into the cement lines is degraded with age, as porosity increases. The findings also suggest that the cracks are more likely to deflect and propagate in the cement lines if the crack approaches the cement lines with a smaller angle.

To conclude, the PF method is a promising tool to use to model human cortical bone at the microscale. It can give insights in how the microstructure of the cortical bone tissue affects crack propagation, which can be difficult to test experimentally.

References

[1] Nationalencyklopedin: Benvävnad. https://www.ne.se/uppslagsverk/encyklopedi/lång/benvävnad. (Accessed: 2021-12-08).

[2] M. Ambati, T. Gerasimov, and L. De Lorenzis. A review on phase-field models of brittle fracture and a new fast hybrid formulation. *Computational Mechanics*, 55(2):383–405, 2015.

[3] H. Amor, J.-J. Marigo, and C. Maurini. Regularized formulation of the variational brittle fracture with unilateral contact: Numerical experiments. *Journal of the Mechanics and Physics of Solids*, 57(8):1209–1229, 2009.

[4] B. Bourdin, G. A. Francfort, and J.-J. Marigo. Numerical experiments in revisited brittle fracture. *Journal of the Mechanics and Physics of Solids*, 48(4):797–826, 2000.

[5] J. Carlsson. *On Crack Dynamics in Brittle Heterogeneous Materials*. PhD thesis, Acta Universitatis Upsaliensis, 2020.

[6] J. Carlsson and P. Isaksson. Simulating fracture in a wood microstructure using a high-resolution dynamic phase field model. *Engineering Fracture Mechanics*, 232:107030, 2020.

[7] K. S. Chan, C. K. Chan, and D. P. Nicolella. Relating crack-tip deformation to mineralization and fracture resistance in human femur cortical bone. *Bone*, 45(3):427–434, 2009.

[8] C. R. Ethier and C. A. Simmons. *Introductory biomechanics: from cells to organisms*. Cambridge University Press, 2013.

[9] G. A. Francfort and J.-J. Marigo. Revisiting brittle fracture as an energy minimization problem. *Journal of the Mechanics and Physics of Solids*, 46(8):1319–1342, 1998.

[10] E. Giner, R. Belda, C. Arango, A. Vercher-Martínez, J. E. Tarancón, and F. J. Fuenmayor. Calculation of the critical energy release rate gc of the cement line in cortical bone combining experimental tests and finite element models. *Engineering Fracture Mechanics*, 184:168–182, 2017.

[11] A. A. Griffith. Vi. the phenomena of rupture and flow in solids. *Philosophical transactions of the royal society of london. Series A, containing papers of a mathematical or physical character*, 221(582-593):163–198, 1921.

[12] D. Gross and T. Seelig. *Fracture mechanics: with an introduction to micromechanics*. Springer, 2017.

[13] A. Gustafsson. *The role of microstructure for crack propagation in cortical bone*. PhD thesis, Lund University, 2019.

[14] A. Gustafsson, H. Khayyeri, M. Wallin, and H. Isaksson. An interface damage model that captures crack propagation at the microscale in cortical bone using xfem. *Journal of the mechanical behavior of biomedical materials*, 90:556–565, 2019.

[15] A. Gustafsson, M. Wallin, and H. Isaksson. Age-related properties at the microscale affect crack propagation in cortical bone. *Journal of biomechanics*, 95:109326, 2019.

[16] A. Gustafsson, M. Wallin, H. Khayyeri, and H. Isaksson. Crack propagation in cortical bone is affected by the characteristics of the cement line: a parameter study using an xfem interface damage model. *Biomechanics and modeling in mechanobiology*, 18(4):1247–1261, 2019.

[17] A. R. Ingraffea and M. Grigoriu. Probabilistic fracture mechanics: A validation of predictive capability. Technical report, Cornell Univ Ithaca Ny Dept OF Structural Engineering, 1990.

[18] G. R. Irwin. Analysis of stresses and strains near the end of a crack traversing a plate. 1957.

[19] K. J. Koester, J. Ager, and R. Ritchie. The true toughness of human cortical bone measured with realistically short cracks. *Nature materials*, 7(8):672–677, 2008.

[20] P. K. Kristensen and E. Martínez-Pañeda. Phase field fracture modelling using quasi-newton methods and a new adaptive step scheme. *Theoretical and Applied Fracture Mechanics*, 107:102446, 2020.

[21] A. Kumar, B. Bourdin, G. A. Francfort, and O. Lopez-Pamies. Revisiting nucleation in the phase-field approach to brittle fracture. *Journal of the Mechanics and Physics of Solids*, 142:104027, 2020.

[22] M. E. Launey, M. J. Buehler, and R. O. Ritchie. On the mechanistic origins of toughness in bone. *Annual review of materials research*, 40:25–53, 2010.

[23] E. Maghami, T. O. Josephson, J. P. Moore, T. Rezaee, T. A. Freeman, L. Karim, and A. R. Najafi. Fracture behavior of human cortical bone: Role of advanced glycation end-products and microstructural features. *Journal of Biomechanics*, 125:110600, 2021.

[24] T. K. Mandal, V. P. Nguyen, and J.-Y. Wu. Length scale and mesh bias sensitivity of phase-field models for brittle and cohesive fracture. *Engineering Fracture Mechanics*, 217:106532, 2019.

[25] E. Martínez-Pañeda, A. Golahmar, and C. F. Niordson. A phase field formulation for hydrogen assisted cracking. *Computer Methods in Applied Mechanics and Engineering*, 342:742–761, 2018.

[26] C. Miehe, M. Hofacker, and F. Welschinger. A phase field model for rate-independent crack propagation: Robust algorithmic implementation based on operator splits. *Computer Methods in Applied Mechanics and Engineering*, 199(45-48):2765–2778, 2010.

[27] S. Mischinski and A. Ural. Finite element modeling of microcrack growth in cortical bone. 2011.

[28] G. Molnár and A. Gravouil. 2d and 3d abaqus implementation of a robust staggered phase-field solution for modeling brittle fracture. *Finite Elements in Analysis and Design*, 130:27–38, 2017.

[29] G. Molnar, A. Gravouil, R. Seghir, and J. Réthoré. An open-source abaqus implementation of the phase-field method to study the effect of plasticity on the instantaneous fracture toughness in dynamic crack propagation. *Computer Methods in Applied Mechanics and Engineering*, 365:113004, 2020.

[30] L. Mullins, V. Sassi, P. McHugh, and M. Bruzzi. Differences in the crack resistance of interstitial, osteonal and trabecular bone tissue. *Annals of biomedical engineering*, 37(12):2574, 2009.

[31] Y. Navidtehrani, C. Betegón, and E. Martínez-Pañeda. A unified abaqus implementation of the phase field fracture method using only a user material subroutine. *Materials*, 14(8):1913, 2021.

[32] J. A. Nirody, K. P. Cheng, R. M. Parrish, A. J. Burghardt, S. Majumdar, T. M. Link, and G. J. Kazakia. Spatial distribution of intracortical porosity varies across age and sex. *Bone*, 75:88–95, 2015.

[33] M. Nordin and V. H. Frankel. *Basic biomechanics of the musculoskeletal system*. Wolters Kluwer Health/Lippincott Williams Wilkins, 4 edition, 2012.

[34] J. Y. Rho, P. Zioupos, J. D. Currey, and G. M. Pharr. Microstructural elasticity and regional heterogeneity in human femoral bone of various ages examined by nano-indentation. *Journal of biomechanics*, 35(2):189–198, 2002.

[35] J. G. Skedros, J. L. Holmes, E. G. Vajda, and R. D. Bloebaum. Cement lines of secondary osteons in human bone are not mineral-deficient: New data in a historical perspective. *The Anatomical Record Part A: Discoveries in Molecular, Cellular, and Evolutionary Biology: An Official Publication of the American Association of Anatomists*, 286(1):781–803, 2005.

[36] U. G. Wegst, H. Bai, E. Saiz, A. P. Tomsia, and R. O. Ritchie. Bioinspired structural materials. *Nature materials*, 14(1):23–36, 2015.

A Appendix

A.1 Derivation of the strong form

Start with the total energy of the body:

$$\begin{aligned}\Pi(\boldsymbol{u}, d) &= \Pi^{int}(\boldsymbol{u}, d) + \Pi^{crack}(d, \nabla d) + \Pi^{ext}(\boldsymbol{u}) \\ &= \int_{\mathcal{B}} [1-d]^2 \hat{\psi}^+(\boldsymbol{\varepsilon}) + \hat{\psi}^-(\boldsymbol{\varepsilon}) \mathrm{d}V + \mathcal{G}_c \int_{\mathcal{B}} \gamma(d, \nabla d) \mathrm{d}V \\ &+ \int_{\partial\mathcal{B}} -\boldsymbol{t} \cdot \boldsymbol{u} \mathrm{d}A + \int_{\mathcal{B}} -\boldsymbol{u} \cdot \hat{\boldsymbol{b}} \mathrm{d}V\end{aligned}$$

The first variation of $\Pi(\boldsymbol{u}, d)$:

$$\begin{aligned}\delta\Pi(\boldsymbol{u}, d \mid \delta\boldsymbol{u}, \delta d) = \lim_{\epsilon \to 0} \frac{\mathrm{d}}{\mathrm{d}\epsilon} \Pi\left(\boldsymbol{u}^*, d^*\right) = 0, \quad \epsilon \in \mathbb{R} \quad \text{with} \\ \boldsymbol{u}^* = \boldsymbol{u} + \epsilon\delta\boldsymbol{u} \\ d^* = d + \epsilon\delta d\end{aligned}$$

This will give a set of partial differential equations (PDE) called Euler-Lagrange equations.

A.1.1 Variation of the displacement field

Variation of the displacement field:

$$\delta\Pi(\boldsymbol{u}, d \mid \delta\boldsymbol{u}) = \lim_{\epsilon \to 0} \frac{\mathrm{d}}{\mathrm{d}\epsilon} \Pi\left(\boldsymbol{u}^*, d\right) = 0 \quad \text{with} \quad \boldsymbol{u}^* = \boldsymbol{u} + \epsilon\delta\boldsymbol{u}$$

$$\begin{aligned}\delta\Pi(\boldsymbol{u}, d \mid \delta\boldsymbol{u}) &= \lim_{\epsilon \to 0} \frac{\mathrm{d}}{\mathrm{d}\epsilon} \int_{\mathcal{B}} [1-d]^2 \hat{\psi}^+\left(\boldsymbol{\varepsilon}\left(\boldsymbol{u}^*\right)\right) + \hat{\psi}^-\left(\boldsymbol{\varepsilon}\left(\boldsymbol{u}^*\right)\right) \mathrm{d}V \\ &+ \lim_{\epsilon \to 0} \frac{\mathrm{d}}{\mathrm{d}\epsilon} \left\{ \int_{\partial\mathcal{B}} -\boldsymbol{u}^* \cdot \boldsymbol{t} \mathrm{d}A + \int_{\mathcal{B}} -\boldsymbol{u}^* \cdot \hat{\boldsymbol{b}} \mathrm{d}V \right\} \\ &= \lim_{\epsilon \to 0} \int_{\mathcal{B}} \left\{ [1-d]^2 \frac{\partial \hat{\psi}^+}{\partial \boldsymbol{\varepsilon}} : \frac{\partial \boldsymbol{\varepsilon}}{\partial \boldsymbol{h}} : \frac{\mathrm{d}}{\mathrm{d}\epsilon} (\nabla(\boldsymbol{u} + \epsilon\delta\boldsymbol{u})) \right. \\ &+ \left. \frac{\partial \hat{\psi}^-}{\partial \boldsymbol{\varepsilon}} : \frac{\partial \boldsymbol{\varepsilon}}{\partial \boldsymbol{h}} : \frac{\mathrm{d}}{\mathrm{d}\epsilon} (\nabla(\boldsymbol{u} + \epsilon\delta\boldsymbol{u})) \right\} \mathrm{d}V \\ &+ \lim_{\epsilon \to 0} \left\{ \int_{\partial\mathcal{B}} -\frac{\mathrm{d}}{\mathrm{d}\epsilon} (\boldsymbol{u} + \epsilon\delta\boldsymbol{u}) \cdot \boldsymbol{t} \mathrm{d}A + \int_{\mathcal{B}} -\frac{\mathrm{d}}{\mathrm{d}\epsilon} (\boldsymbol{u} + \epsilon\delta\boldsymbol{u}) \cdot \hat{\boldsymbol{b}} \mathrm{d}V \right\} = 0\end{aligned}$$

where $\boldsymbol{\varepsilon}(\boldsymbol{u}) = \frac{1}{2}\left[\boldsymbol{h}(\boldsymbol{u}) + \boldsymbol{h}^t(\boldsymbol{u})\right]$ and $\boldsymbol{h} = \nabla\boldsymbol{u}$.

$$
\begin{aligned}
\delta\Pi(\boldsymbol{u}, d \mid \delta\boldsymbol{u}) &= \lim_{\epsilon\to 0}\frac{\mathrm{d}}{\mathrm{d}\epsilon}\int_{\mathcal{B}}\Big\{[1-d]^2\frac{\partial\hat{\psi}^+}{\partial\boldsymbol{\varepsilon}} : \frac{\partial\boldsymbol{\varepsilon}}{\partial\boldsymbol{h}} : \frac{\mathrm{d}}{\mathrm{d}\epsilon}(\nabla(\boldsymbol{u}+\epsilon\delta\boldsymbol{u})) \\
&\quad + \frac{\partial\hat{\psi}^-}{\partial\boldsymbol{\varepsilon}} : \frac{\partial\boldsymbol{\varepsilon}}{\partial\boldsymbol{h}} : \frac{\mathrm{d}}{\mathrm{d}\epsilon}(\nabla(\boldsymbol{u}+\epsilon\delta\boldsymbol{u}))\Big\}\mathrm{d}V \\
&\quad + \lim_{\epsilon\to 0}\left\{\int_{\partial\mathcal{B}} -\frac{\mathrm{d}}{\mathrm{d}\epsilon}(\boldsymbol{u}+\epsilon\delta\boldsymbol{u})\cdot\boldsymbol{t}\mathrm{d}A + \int_{\mathcal{B}} -\frac{\mathrm{d}}{\mathrm{d}\epsilon}(\boldsymbol{u}+\epsilon\delta\boldsymbol{u})\cdot\hat{\boldsymbol{b}}\mathrm{d}V\right\} \\
&= \lim_{\epsilon\to 0}\frac{\mathrm{d}}{\mathrm{d}\epsilon}\int_{\mathcal{B}}\Big\{\boldsymbol{\sigma}^+ : \boldsymbol{I}_{sym} : \nabla\delta\boldsymbol{u} + \boldsymbol{\sigma}^- : \boldsymbol{I}_{sym} : \nabla\delta\boldsymbol{u}\Big\}\mathrm{d}V \\
&\quad + \lim_{\epsilon\to 0}\left\{\int_{\partial\mathcal{B}} -\delta\boldsymbol{u}\cdot\boldsymbol{t}\mathrm{d}A + \int_{\mathcal{B}} -\delta\boldsymbol{u}\cdot\hat{\boldsymbol{b}}\mathrm{d}V\right\} \\
&= \int_{\mathcal{B}}(\boldsymbol{\sigma}^+ : \nabla\delta\boldsymbol{u} + \boldsymbol{\sigma}^- : \nabla\delta\boldsymbol{u})\mathrm{d}V + \int_{\partial\mathcal{B}} -\delta\boldsymbol{u}\cdot\boldsymbol{t}\mathrm{d}A + \int_{\mathcal{B}} -\delta\boldsymbol{u}\cdot\hat{\boldsymbol{b}}\mathrm{d}V \\
&= \int_{\mathcal{B}}\boldsymbol{\sigma} : \nabla\delta\boldsymbol{u}\mathrm{d}V + \int_{\partial\mathcal{B}} -\delta\boldsymbol{u}\cdot\boldsymbol{t}\mathrm{d}A + \int_{\mathcal{B}} -\delta\boldsymbol{u}\cdot\hat{\boldsymbol{b}}\mathrm{d}V = 0
\end{aligned}
$$

The first integral can be rewritten using the identity:

$$\mathrm{div}(\delta\boldsymbol{u}\cdot\boldsymbol{\sigma}) = \nabla\delta\boldsymbol{u} : \boldsymbol{\sigma} + \delta\boldsymbol{u}\cdot\mathrm{div}\,\boldsymbol{\sigma} \quad \Leftrightarrow \quad \nabla\delta\boldsymbol{u} : \boldsymbol{\sigma} = \mathrm{div}(\delta\boldsymbol{u}\cdot\boldsymbol{\sigma}) - \delta\boldsymbol{u}\cdot\mathrm{div}\,\boldsymbol{\sigma}$$

together with the divergence theorem and Cauchy theorem:

$$\int_{\mathcal{B}}\mathrm{div}(\delta\boldsymbol{u}\cdot\boldsymbol{\sigma})\mathrm{d}V = \int_{\partial\mathcal{B}}\delta\boldsymbol{u}\cdot\boldsymbol{\sigma}\cdot\boldsymbol{n}\mathrm{d}A = \int_{\partial\mathcal{B}}\delta\boldsymbol{u}\cdot\boldsymbol{t}\mathrm{d}A$$

The final expression of the variation of the displacement field is then:

$$
\begin{aligned}
\delta\Pi(\boldsymbol{u}, d \mid \delta\boldsymbol{u}) &= \int_{\mathcal{B}}\nabla\delta\boldsymbol{u} : \boldsymbol{\sigma}\mathrm{d}V + \int_{\partial\mathcal{B}} -\delta\boldsymbol{u}\cdot\boldsymbol{t}\mathrm{d}A + \int_{\mathcal{B}} -\delta\boldsymbol{u}\cdot\hat{\boldsymbol{b}}\mathrm{d}V \\
&= \int_{\mathcal{B}}\mathrm{div}(\delta\boldsymbol{u}\cdot\boldsymbol{\sigma})\mathrm{d}V - \int_{\mathcal{B}}\delta\boldsymbol{u}\cdot\mathrm{div}\,\boldsymbol{\sigma}\mathrm{d}V + \int_{\partial\mathcal{B}} -\delta\boldsymbol{u}\cdot\boldsymbol{t}\mathrm{d}A + \int_{\mathcal{B}}\delta\boldsymbol{u}\cdot\hat{\boldsymbol{b}}\mathrm{d}V \\
&= \int_{\partial\mathcal{B}}\delta\boldsymbol{u}\cdot\boldsymbol{t}\mathrm{d}A - \int_{\mathcal{B}}\delta\boldsymbol{u}\cdot\mathrm{div}\,\boldsymbol{\sigma}\mathrm{d}V + \int_{\partial\mathcal{B}} -\delta\boldsymbol{u}\cdot\boldsymbol{t}\mathrm{d}A + \int_{\mathcal{B}} -\delta\boldsymbol{u}\cdot\hat{\boldsymbol{b}}\mathrm{d}V \\
&= \int_{\mathcal{B}} -\delta\boldsymbol{u}\cdot\mathrm{div}\,\boldsymbol{\sigma}\mathrm{d}V + \int_{\mathcal{B}} -\delta\boldsymbol{u}\cdot\hat{\boldsymbol{b}}\mathrm{d}V = \int_{\mathcal{B}} -\delta\boldsymbol{u}\cdot(\mathrm{div}\,\boldsymbol{\sigma} + \hat{\boldsymbol{b}})\mathrm{d}V = 0
\end{aligned}
$$

and the strong form for the displacement field is:

$$\int_{\mathcal{B}} \delta \boldsymbol{u} \cdot [\operatorname{div} \boldsymbol{\sigma} + \hat{\boldsymbol{b}}] \mathrm{d}V = 0 \quad \forall \delta \boldsymbol{u} \qquad \Rightarrow \qquad \operatorname{div} \boldsymbol{\sigma} + \hat{\boldsymbol{b}} = 0$$

A.1.2 Variation of the phase field

Variation of the phase field:

$$\delta \Pi(\boldsymbol{u}, d \mid \delta d) = \lim_{\epsilon \to 0} \frac{\mathrm{d}}{\mathrm{d}\epsilon} \Pi(\boldsymbol{u}, d^*) = 0 \quad \text{with} \quad d^* = d + \epsilon \delta d$$

$$\delta \Pi(\boldsymbol{u}, d \mid \delta d) = \lim_{\epsilon \to 0} \frac{\mathrm{d}}{\mathrm{d}\epsilon} \int_{\mathcal{B}} [1 - d^*]^2 \hat{\psi}^+(\varepsilon) + \hat{\psi}^-(\varepsilon) \mathrm{d}V + \mathcal{G}_c \int_{\mathcal{B}} \gamma(d, \nabla d) \mathrm{d}V$$

Since the crack functional $\gamma(d, \nabla d)$ can be described using two different equations, the derivation to the strong form of the phase field will differ.

Variational approach using the crack functional AT2

$$\begin{aligned}
\delta \Pi(\boldsymbol{u}, d \mid \delta d) &= \lim_{\epsilon \to 0} \frac{\mathrm{d}}{\mathrm{d}\epsilon} \int_{\mathcal{B}} [1 - d^*]^2 \hat{\psi}^+(\varepsilon) + \hat{\psi}^-(\varepsilon) \mathrm{d}V + \mathcal{G}_c \int_{\mathcal{B}} \gamma_{AT2}(d, \nabla d) \mathrm{d}V \\
&= \lim_{\epsilon \to 0} \frac{\mathrm{d}}{\mathrm{d}\epsilon} \int_{\mathcal{B}} [1 - d^*]^2 \hat{\psi}^+(\varepsilon) + \hat{\psi}^-(\varepsilon) \mathrm{d}V \\
&+ \mathcal{G}_c \lim_{\epsilon \to 0} \frac{\mathrm{d}}{\mathrm{d}\epsilon} \int_{\mathcal{B}} \frac{1}{2 l_0} \left[d^{*2} + l_0^2 \nabla d^* \cdot \nabla d^* \right] \mathrm{d}V
\end{aligned}$$

The derivations and limits are as followed:

$$\frac{\mathrm{d}}{\mathrm{d}\epsilon} d^{*2} = \frac{\mathrm{d}}{\mathrm{d}\epsilon} \left([d + \epsilon \delta d]^2 \right) = \frac{\mathrm{d}}{\mathrm{d}\epsilon} \left(d^2 + 2 d \epsilon \delta d + \epsilon^2 \delta d^2 \right) = 2 d \delta d + 2 \epsilon \delta d^2 \overset{\epsilon \to 0}{=} 2 d \delta d$$

$$\frac{\mathrm{d}}{\mathrm{d}\epsilon} d^* = \delta d$$

$$\begin{aligned}
\frac{\mathrm{d}}{\mathrm{d}\epsilon} (\nabla d^* \cdot \nabla d^*) &= \frac{\mathrm{d}}{\mathrm{d}\epsilon} (\nabla (d + \epsilon \delta d) \cdot \nabla (d + \epsilon \delta d)) = [\text{apply product rule}] \\
&= \frac{\mathrm{d}}{\mathrm{d}\epsilon} \nabla (d + \epsilon \delta d) \cdot \nabla (d + \epsilon \delta d) + \nabla (d + \epsilon \delta d) \cdot \frac{\mathrm{d}}{\mathrm{d}\epsilon} \nabla (d + \epsilon \delta d) \\
&= \nabla \delta d \cdot \nabla (d + \epsilon \delta d) + \nabla (d + \epsilon \delta d) \cdot \nabla \delta d \\
&\overset{\epsilon \to 0}{=} \nabla \delta d \cdot \nabla d + \nabla d \cdot \nabla \delta d = 2 \nabla \delta d \cdot \nabla d
\end{aligned}$$

Inserted into the variation of the phase field d:

$$\delta\Pi(\boldsymbol{u}, d \mid \delta d) = \int_{\mathcal{B}} \Big\{ -\delta d 2[1-d]\hat{\psi}^{+} + \frac{\mathcal{G}_c}{2l_0}\left[\delta d 2d + l_0^2 2\nabla\delta d \cdot \nabla d\right] \Big\} \mathrm{d}V = 0$$

Using the identity $\nabla\delta d \cdot \nabla d = \operatorname{div}(\delta d \nabla d) - \delta d \operatorname{div}\nabla d$, the expression can be rewritten:

$$\begin{aligned}\delta\Pi(\boldsymbol{u}, d \mid \delta d) = &\int_{\mathcal{B}} -\delta d 2[1-d]\hat{\psi}^{+} \\ &+ \frac{\mathcal{G}_c}{l_0}\left[\delta d d - l_0^2 \delta d \operatorname{div}\nabla d\right] \mathrm{d}V + \int_{\mathcal{B}} \mathcal{G}_c l_0 \operatorname{div}(\delta d \nabla d)\mathrm{d}V = 0\end{aligned}$$

Using Gauss divergence theorem $\int_{\mathcal{B}} \operatorname{div}(\delta d \nabla d)\mathrm{d}V = \int_{\partial\mathcal{B}} \delta d \nabla d \cdot \boldsymbol{n}\mathrm{d}A$ and assuming homogeneous Neumann boundary conditions for the d-field: $\mathcal{G}_c l_0 \nabla d \cdot \boldsymbol{n} = 0$ on $\partial\mathcal{B}$ gives:

$$\begin{aligned}\delta\Pi(\boldsymbol{u}, d \mid \delta d) = \int_{\mathcal{B}} \delta d \left[-2[1-d]\hat{\psi}^{+} + \frac{\mathcal{G}_c}{l_0}\left[d - l_0^2 \operatorname{div}\nabla d\right]\right] \mathrm{d}V = 0 \quad \forall \delta d \\ \Rightarrow \qquad 2[1-d]\hat{\psi}^{+} - \frac{\mathcal{G}_c}{l_0}\left[d - l_0^2 \operatorname{div}\nabla d\right] = 0\end{aligned}$$

Variational approach using the crack functional AT1

$$\begin{aligned}\delta\Pi(\boldsymbol{u}, d \mid \delta d) &= \lim_{\epsilon\to 0} \frac{\mathrm{d}}{\mathrm{d}\epsilon} \int_{\mathcal{B}} \left[1-d^*\right]^2 \hat{\psi}^{+}(\varepsilon) + \hat{\psi}^{-}(\varepsilon)\mathrm{d}V + \mathcal{G}_c \int_{\mathcal{B}} \gamma_{AT1}(d, \nabla d)\mathrm{d}V \\ &= \lim_{\epsilon\to 0} \frac{\mathrm{d}}{\mathrm{d}\epsilon} \int_{\mathcal{B}} \left[1-d^*\right]^2 \hat{\psi}^{+}(\varepsilon) + \hat{\psi}^{-}(\varepsilon)\mathrm{d}V \\ &+ \mathcal{G}_c \lim_{\epsilon\to 0} \frac{\mathrm{d}}{\mathrm{d}\epsilon} \int_{\mathcal{B}} \frac{3}{8l_0}\left[d^* + l_0^2 \nabla d^* \cdot \nabla d^*\right] \mathrm{d}V\end{aligned}$$

The derivations and limits expressed in previously can be inserted into the variation of the phase field d:

$$\delta\Pi(\boldsymbol{u}, d \mid \delta d) = \int_{\mathcal{B}} \Big\{ -\delta d 2[1-d]\hat{\psi}^{+} + \mathcal{G}_c \frac{3}{8l_0}\left[\delta d + l_0^2 2\nabla\delta d \cdot \nabla d\right] \Big\} \mathrm{d}V = 0$$

Using the identity $\nabla\delta d \cdot \nabla d = \operatorname{div}(\delta d \nabla d) - \delta d \operatorname{div}\nabla d$, the expression can be rewritten:

$$\begin{aligned}\delta\Pi(\boldsymbol{u}, d \mid \delta d) = &\int_{\mathcal{B}} -\delta d 2[1-d]\hat{\psi}^{+} + \mathcal{G}_c \frac{3}{8l_0}\left[\delta d - l_0^2 2\delta d \operatorname{div}\nabla d\right] \mathrm{d}V \\ &+ \int_{\mathcal{B}} \frac{3}{4}\mathcal{G}_c l_0 \operatorname{div}(\delta d \nabla d)\mathrm{d}V = 0\end{aligned}$$

Using Gauss divergence theorem $\int_{\mathcal{B}} \operatorname{div}(\delta d \nabla d) \mathrm{d}V = \int_{\partial\mathcal{B}} \delta d \nabla d \cdot \boldsymbol{n} \mathrm{d}A$ and assuming homogeneous Neumann boundary conditions for the d-field: $\frac{3}{4}\mathcal{G}_c l_0 \nabla d \cdot \boldsymbol{n} = 0$ on $\partial\mathcal{B}$ gives:

$$\delta\Pi(\boldsymbol{u}, d \mid \delta d) = \int_{\mathcal{B}} \delta d \left[-2[1-d]\hat{\psi}^+ + \frac{3\mathcal{G}_c}{8l_0}\left[1 - 2l_0^2 \operatorname{div}\nabla d\right]\right] \mathrm{d}V = 0 \quad \forall \delta d$$

$$\Rightarrow \qquad 2[1-d]\hat{\psi}^+ - \frac{3\mathcal{G}_c}{8l_0}\left[1 - 2l_0^2 \operatorname{div}\nabla d\right] = 0$$

A.1.3 The strong form

The strong forms using the two different crack functionals are and with the positive part of the strain energy density replaced with the history field $\psi^+ = \mathscr{H}$:

The strong form using AT2

The strong form for the crack functional AT2 is:

$$\begin{aligned} &\operatorname{div}\boldsymbol{\sigma} + \hat{\boldsymbol{b}} = 0 \\ &2[1-d]\mathscr{H} - \frac{\mathcal{G}_c}{l_0}\left[d - l_0^2 \operatorname{div}\nabla d\right] = 0 \end{aligned}$$

subjected to the boundary conditions:

$$\begin{aligned} \boldsymbol{u} &= \overline{\boldsymbol{u}} \quad \text{on} \quad \partial\mathcal{B}^u \\ \boldsymbol{t} &= \overline{\boldsymbol{t}} \quad \text{on} \quad \partial\mathcal{B}^t \\ \mathcal{G}_c l_0 \nabla d \cdot \boldsymbol{n} &= 0 \quad \text{on} \quad \partial\mathcal{B} \end{aligned}$$

The strong form using AT1

The strong form for the crack functional AT1 is:

$$\begin{aligned} &\operatorname{div}\boldsymbol{\sigma} + \hat{\boldsymbol{b}} = 0 \\ &2[1-d]\mathscr{H} - \frac{3\mathcal{G}_c}{8l_0}\left[1 - 2l_0^2 \operatorname{div}\nabla d\right] = 0 \end{aligned}$$

subjected to the boundary conditions:

$$\begin{aligned} \boldsymbol{u} &= \overline{\boldsymbol{u}} \quad \text{on} \quad \partial\mathcal{B}^u \\ \boldsymbol{t} &= \bar{\boldsymbol{t}} \quad \text{on} \quad \partial\mathcal{B}^t \\ \frac{3}{4}\mathcal{G}_c l_0 \nabla d \cdot \boldsymbol{n} &= 0 \quad \text{on} \quad \partial\mathcal{B} \end{aligned}$$

B Appendix

B.1 Plots of strain of Model A for different porosities

Equivalent strain prior to crack initiation

Model A with a geometrically introduced crack

Porosity 0%

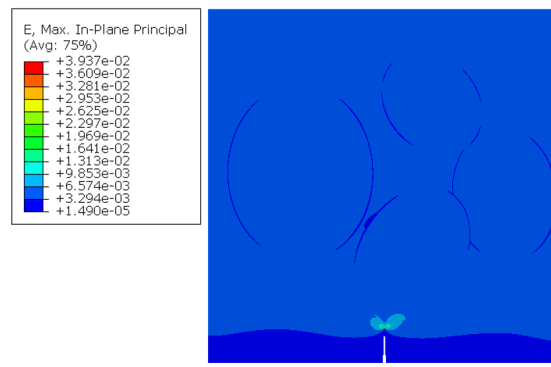

Porosity 7%

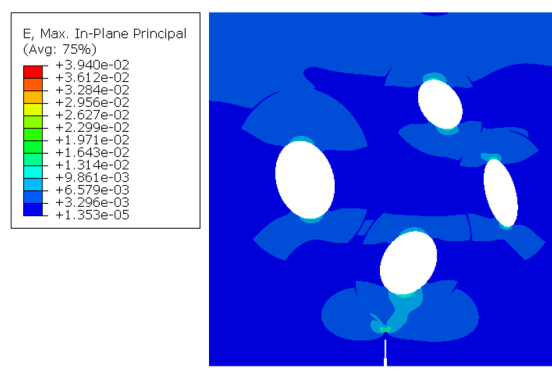

Porosity 15%

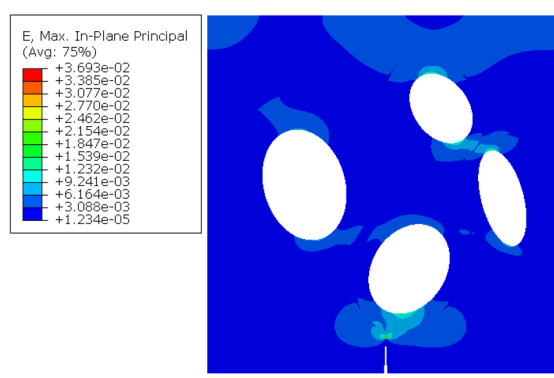

Equivalent strain prior to crack initiation

Model A without a geometrically introduced crack

Porosity 0%

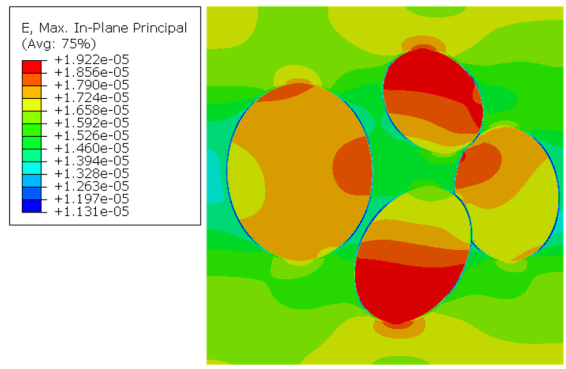

Porosity 7%

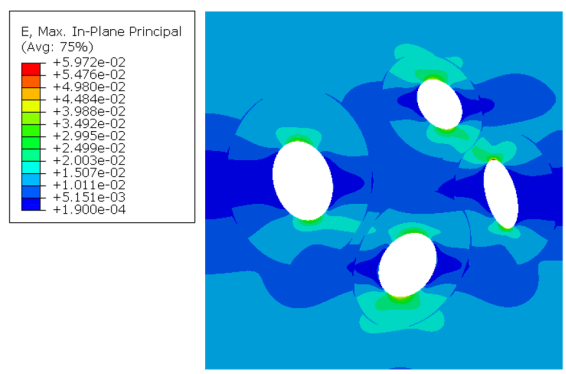

Porosity 15%

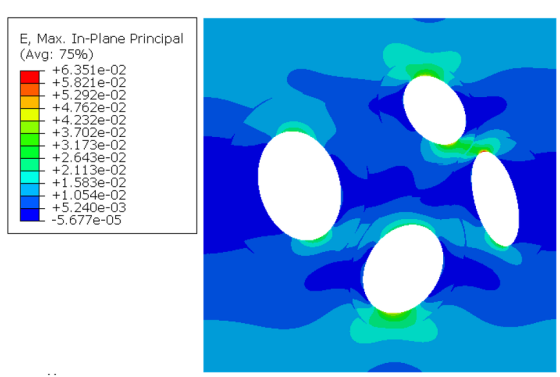

B.2 Plots of stress of Model A for different porosities

Stress levels in the x-direction prior to crack initiation

Model A with a geometrically introduced crack

Porosity 0%

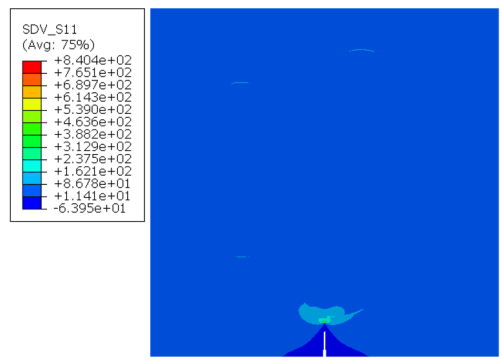

Porosity 7%

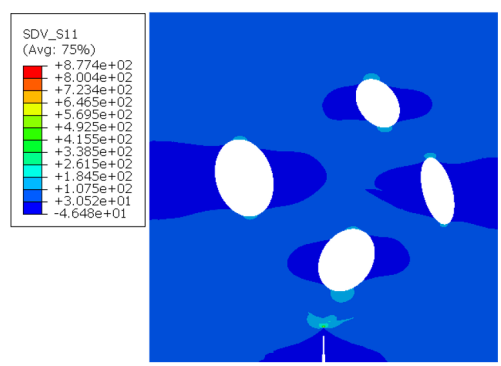

Porosity 15%

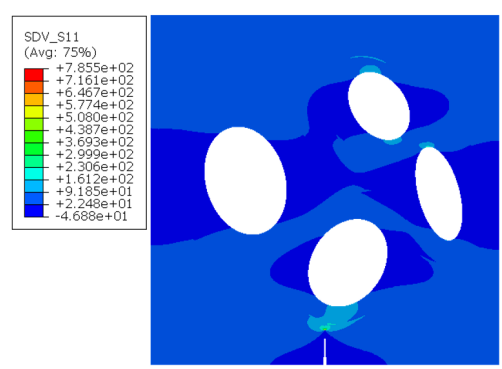

Stress levels in the y-direction prior to crack initiation

Model A with a geometrically introduced crack

Porosity 0%

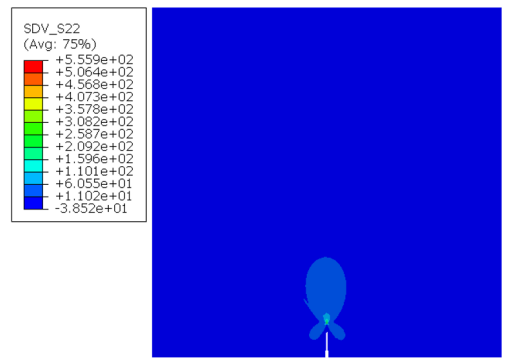

Porosity 7%

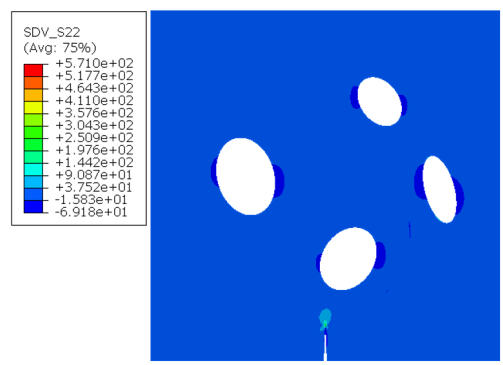

Porosity 15%

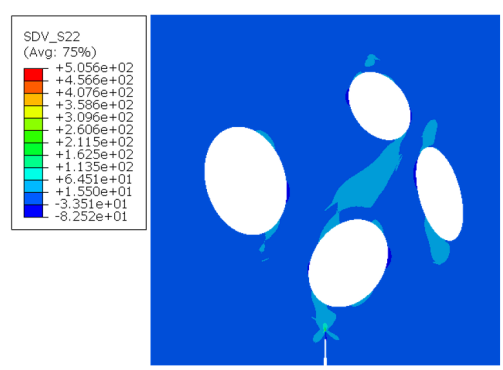

Stress levels in the x-direction prior to crack initiation

Model A without a geometrically introduced crack

Porosity 0%

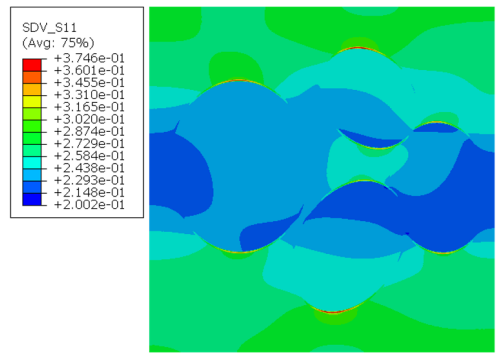

Porosity 7%

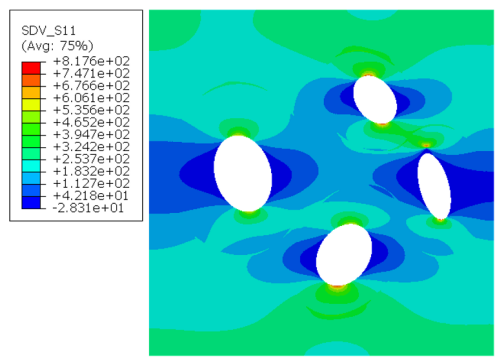

Porosity 15%

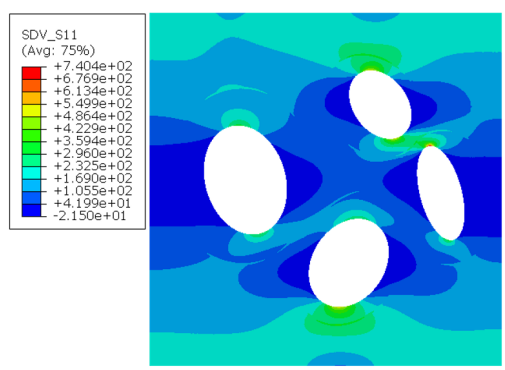

Stress levels in the y-direction prior to crack initiation

Model A without a geometrically introduced crack

Porosity 0%

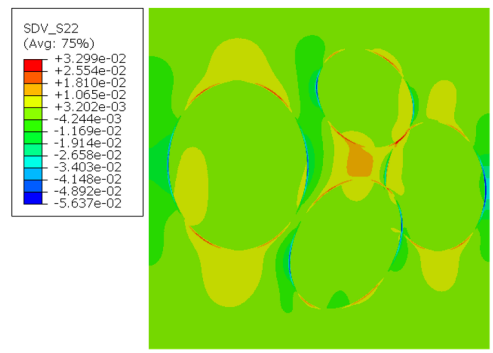

Porosity 7%

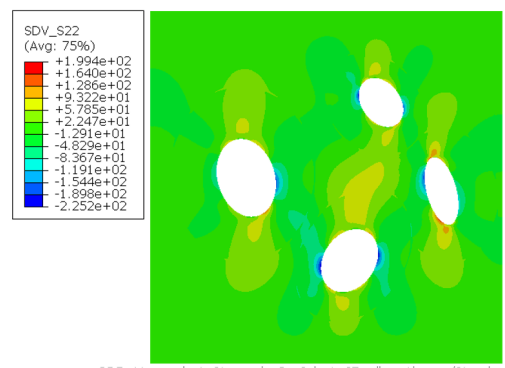

Porosity 15%